DOCTORAL THESIS

Development of Innovative Electrodes for the Electrocatalytic Conversion of Small Molecules

Università degli Studi di Messina

(HOME Institution)

Host Institution: École supérieure de chimie physique électronique de Lyon,
Université Claude Bernard Lyon 1

SINCHEM - Sustainable Industrial Chemistry Erasmus Mundus - Joint Doctoral Research Program

Doctoral Dissertation of: **Hua WEI**

Doctoral Program in

ENGINEERING AND CHEMISTRY OF MATERIALS AND CONSTRUCTIONS
(XXXIII Cycle, Department of Engineering)

The Chair of the Doctoral Program: Prof. Giovanni NERI

SSD: ING-IND/25 (Chemical Plants); CHIM/04 (Industrial Chemistry)

Supervisor (HOME): **Prof. Claudio AMPELLI**

Supervisor (HOST): **Prof. Jérome CANIVET**

November 2020

N° d’ordre NNT : xxx

THESE de DOCTORAT DE L’UNIVERSITE DE LYON
opérée au sein de
L’Université Claude Bernard Lyon 1

Ecole Doctorale N° ED206

Spécialité de doctorat : Chimie
Discipline : Chimie Industrielle Durable

Soutenue publiquement le 04/03/2021 par
Wei Hua

Développement d'électrodes innovantes pour la conversion électrocatalytique de petites molécules

---

Devant le jury composé de:

Prof.ssa Stefania ALBONETTI	Università di Bologne	Rapporteure
Dr. Jérôme CANIVET	CNRS-Université Lyon 1	Directeur de thèse
Prof. Gabriele CENTI	Università di Messina	Examinateur
Dr. Francesco DI-RENZO	CNRS-ICG Montpellier	Rapporteur
Dr. Shashank MISHRA	Université Lyon 1	Examinateur
Prof.ssa Anna Maria RASPOLLI GALLETTI	Università di Pisa	Examinatrice
Prof. Singlinda PERATHONER	Università di Messina	Directrice de thèse
Prof.ssa Michela SIGNORETTO	Università Ca' Foscari Venezia	Examinatrice
Prof. Claudio AMPELLI	Università di Messina	Co-directeur de these, Invité
Dr. Elsje Alessandra QUADRELLI	CNRS-Université Lyon 1	Co-directrice de these, Invitée

Sustainable
Industrial
Chemistry

Erasmus+

The research presented in this Ph.D. thesis was carried out at the University of Messina, Department of Engineering, Laboratory of Catalysis for Sustainable Productions and Energy (CASPE/INSTM) and Université Lyon 1 - Claude Bernard, IRCELYON - Institut de Recherche sur la Catalyse et l'Environnement de Lyon (UMR5256)

This work was co-funded through a SINCHEM Grant. SINCHEM is a Joint Doctorate programme selected under the Erasmus Mundus Action 1 Programme (FPA 2013-0037),

Acknowledgement

Firstly, I would like to express my sincere gratitude to my Ph.D. supervisor ***Prof. Claudio Ampelli*** for the continuous support of my Ph.D. study and related research, for his patience, motivation, and immense knowledge. I learned a lot from his deep thinking and intuitive explanation. He has guided me and encouraged me to carry on through my Ph.D. study and has contributed to this thesis with a major impact. I have been very lucky to have his constant support during my Ph.D. and to share his passion for the research we have done.

I would also like to thank ***Prof. Gabriele Centi***, who offers critical comments on scientific problems and invaluable advice on academic career. Prof. Centi's wise insight and his continually passion on scientific research after he achieved the worldwide reputation let me know what is a real scientist should be.

I am thankful to ***Prof. Elsje Alessandra Quadrelli***. She was not only a source of academic wisdom, but also a kind caring mentor who provided personal support during my stay in Universite Claude Bernard Lyon, France.

I would like to thank my co-supervisor ***Dr. Jerome Canivet*** and the ING group of IRCELYON. Dr. Jerome taught me from the beginning on MOFs materials, such as how to prepare, characterize and test in a reaction. Many thanks for providing detailed support and feedback for my experimental design and thesis writing. In addition to all the members of the ING group, I would especially like to thank members of Dr. Florian Wisser, Mehdi Bessaa, Remy Rajapaksha, Baptiste Chauchon, Dr.Katia Barbera Dr. David Farrusseng and Dr. Marcelo Alves Favaro, for the kind help, sharing ideas and guidance during my stay in IRCELYON, Universite Claude Bernard Lyon, France.

I would like to thank all the past and present members of the Prof. Gabriele Centi research group for making the Ph.D. a very enjoyable experience. I would especially like to thank ***Prof. Siglinda Perathoner*** for her friendly and open hearted support to me in working and living in Messina. She always makes me feel all warm and fuzzy inside. I have really enjoyed both working and hanging out with everyone in the laboratory of Catalysis for Sustainable Productions and Energy (University of Messina) and would like to thank Shiming Chen, Daniele, Chalachew, Chiara, Francesco, Paola, Georgia, Gianfranco, Salvatore, Bhanu and Matteo.

I would also like to thank ***Dr. Yuefeng Liu*** and his group in Dalian National Laboratory for Clean Energy (DNL), Dalian Institute of Chemical Physics (DICP, China) for the close and long-term collaboration. We worked together since I was a master's student in China. I want to thank the partners and friends in DICP: Qian Jiang, Ying Ma, Shiyan Li, Qingqing Gu and Tianfu Liu.

I thank the SINCHEM program, the committee, all the Professors and Ph.D. students for their constant support and encouragement. A special thanks go to Prof. Stefania Albonetti (SINCHEM coordinator) for her help and guidance on all the academic and administrative matters. I would also thank to the SINCHEM local coordinators Dr. Francesca Pollicino and Anna Maria Casella for their help provided to carry out my Ph.D. thesis based on the cotutelle between University of Messina and Universite Claude Bernard Lyon. A special thanks to our SINCHEM family – Medet Zhukush, Ana Patricia, Paola Blair, Samantha, Ferenc Martinovic, Valeriia Maslova, Quang Nguyen, Akash Kaithal, Daniel Antonio, Marcelo, Sonia Milena, and Ravi Srivastava.

To my friends scattered around the world, thank you for listening, offering me advice, and supporting me through this entire process. I would like to thank Ying Wang-for your thoughts, phone calls, texts, visits and being there whenever I needed a friend. I also thank my friends in Messina, Lyon and other places around the world: Bassma, Zainab, Ginane, Sanaz, Chalachew, Roberto Di Chio, Huiying Ma, Xueyao Zhang, and Qingyun Dai.

A special thanks for ***Prof. Dangsheng Su***, who is my master supervisor. It is he that introduces me to the wonderful world of science, help me install the sense of research, inspired me to study aboard. We lost him forever on 24th, June 2019. Prof. Su was a wonderful scientist and a kindly tutor who is much beloved and deeply missed by all that knew him. It is extremely hard to convey my gratitude to him in words. I feel most appropriate to dedicate this thesis to him.

Last but not the least, I would like to thank my family: ***my mother, Hong Jia***; ***my father, Xianping Wei***; ***my grandmother, Zhenqin Yin*** and ***my brother, Tongtong Wei***. Their constant love, encouragement, and support have made me believe in myself and there are no words to describe the love and appreciation I feel for them. I would also like to acknowledge my grandfather, ***Shizong Wei,*** who passed away before the completion of my education. I know he would be proud and I will forever be grateful for the love and values he instilled in me.

WEI Hua

2020, Messina, Italy

Abstract (English)

Nitrogen plays an indispensable role for all life on earth and for the development of human beings. Industrially, nitrogen gas is converted to ammonia (NH_3) and nitrogen-rich fertilisers to supplement the amount of nitrogen fixed spontaneously by nature. At present, the only industrial-scale ammonia synthesis technology is the process developed by Haber and Bosch in the early 20th century using gas phase N_2 and H_2 as the feeding gases. However, the Haber-Bosch process requires harsh conditions, complex equipment and high energy consumption, and operates with low conversion rates, which are inconsistent with economic and social growing development requirements. Compared to the Haber-Bosch method, electrocatalysis is one of the promising routes that can integrate electricity produced from renewable energy technologies for the production of ammonia at room temperature and ambient pressure. A specific challenge is related to the development of novel electrocatalysts/electrodes with the aim to achieve a low-cost, large-scale and delocalized production of ammonia.

In view of the above key scientific issues, this PhD work focuses on three main aspects of the electrocatalytic nitrogen reduction reaction (NRR): i) engineering and design of the electrocatalyst, ii) electrode and cell design of the electrochemical device and iii) improvement and optimization of the reaction conditions, to enhance the performances of ammonia synthesis.

Most of the research activities of this PhD work about synthesis and characterization of the electrocatalytic materials and assembling/testing of the

electrodes in unconventional electrochemical devices were carried out at the laboratory CASPE (Laboratory of Catalysis for Sustainable Production and Energy) of the University of Messina. Moreover, during the three years, a period of 12 months was spent in cotutelle with the École supérieure de chimie, physique, électronique de Lyon (CPE Lyon), where advanced synthesis routes were explored for the preparation of organometallic-based electrocatalysts to be used as more active electrodes in NRR.

The PhD thesis is organized in five main chapters. Chapter 1 focuses on N_2 fixation issues and on describing the industrial Haber-Bosch process, with an overview of the general implications related to its high energy requirements. The alternative methods based on the electrochemical nitrogen fixation are then presented, with a wide description of pros and cons related to the milder conditions (i.e., room temperature and atmospheric pressure) and by discussing the elements to be developed for a future implementation of this technology, including a description of the possible reaction mechanism, which is still unclear in literature.

Chapter 2, instead, refers to the electrocatalytic materials developed in this PhD work for the preparation of the electrodes: 1) the Metal-organic Frameworks (MOFs), a class of porous materials very promising for their peculiar characteristics of high surface area, tunable properties, organic functionality and porosity, as well as for the possibility of creating specific catalytic active sites thanks to both the functional groups and the metal ion centres; 2) the MXenes, a class of metal carbide or nitride materials with a two-dimensional (2D) structure, which have recently attracted a large interest for a broad range of applications, including catalysis and N_2

fixation, for their unique properties of metallic conductivity and hydrophilic nature of the hydroxyl or oxygen terminated surfaces.

In Chapters 3-5, the experimental results are presented and discussed. Chapter 3 concerns the preparation of a series of Fe-MOF-based (Fe@Zn/SIM-1) electrodes and their testing in NRR by using an advanced engineered three-phase reactor, working in gas-phase. This novel device operates at room temperature and atmospheric pressure, with counter and reference electrodes immersed into an anode half-cell (where the oxidation of H_2O to O_2 occurs) containing a liquid electrolyte (the anolyte), while the cathode half-cell for NRR operates in gas phase without a liquid electrolyte (electrolyte-less conditions). This type of electrocatalytic reactor is thus quite different from the conventional electrocatalytic reactors operating in liquid phase, with the main advantages of avoiding issues related to the low N_2 solubility and transport in the electrolyte, and allowing an easier recovery of ammonia. The results obtained from these electrocatalytic tests in gas-phase were very useful to improve the design of the MOFs-based electrodes, evidencing the limits of these kinds of materials in terms of N content, stability and possibility to prepare more advanced electrocatalysts by carbonization. A wide part of this chapter was dedicated to the development of new experimental strategies for avoiding false positive in the detection of ammonia, which is one of the topics most studied from scientists working in NRR in the last two years. As accurate protocols were recently suggested in literature, also using advanced analytical techniques (i.e. using ^{15}N labelled nitrogen), an easier methodology based on UV-visible spectrophotometric analysis (coupled with blank tests with inert gases) was suggested in this work to avoid ammonia contaminations and false positives, although more sophisticated analytical techniques may definitely confirm the real source of ammonia.

In Chapter 4, a series of improved Fe-MOF-based materials (Fe-based and Fe-alkali metal-based MOF UiO-66-$(COOH)_2$), synthesized by cation exchange reaction technique to replace the proton of carboxylic acid with an iron cation, are presented. With respect to Fe@Zn/SIM-1, this new class of MOFs are more stable in water and do not contain nitrogen atoms in their structure. Results evidenced that 80% cation exchange Fe@UiO-66-$(COOH)_2$ (with an effective Fe content of around 8 wt.%) was the best electrocatalyst among the tested Fe-based MOF synthesized materials. The performances in NRR highly depended on cell and electrode design. More in detail, an ammonia yield of 1.19 $\mu g \cdot h^{-1} \cdot mg_{cat}^{-2}$ was obtained with an assembling configuration of layers ordered as i) Nafion (the membrane), ii) Fe-based MOF (the electrocatalyst), iii) GDL (the carbon gas diffusion layer) and iv) a further layer of Fe-MOF. The effect of applied voltage was also explored, indicating an optimal voltage of -0.5 V vs. RHE to maximize activity in NRR and limiting the side hydrogen evolution reaction. Moreover, as currently used in the industrial catalysts for Haber-Bosh process, the introduction of potassium in the electrocatalysts was also investigated, in order to facilitate charge transfer from K^- ions to the iron-based catalyst surface, balancing the dissociative chemisorption between H_2 and N_2, and suppressing side reactions, thus improving both activity and stability. These results were very promising, although a further experimentation is needed to improve their performances in NRR, to overcome limitations related to MOF materials themselves, majorly due to their low conductivity and stability.

Finally, Chapter 5 refers to the exploration of advanced MXene materials (Ti_3C_2 MXene) and to the attempt of synthesizing a 3D nanoarchitecture starting from 2D-dimensional MXene-based catalysts. To understand the role of the nanostructure of MXene materials in NRR, Ti_3C_2 nanosheets were treated with KOH to obtain a final shape of three-dimensional (3D) porous frameworks nanoribbons. Specifically, the objective of this research was to investigate how the conversion of Ti_3C_2 nanosheets to 3D-like nanoribbons influence the NRR reactivity in the gas-phase electrochemical device. A full characterization of MXenes nanoribbons (SEM, TEM, HRTEM, XRD, XPS and EDX) was also presented. Results showed that the 3D-type nanostructure (nanoribbons) leads to a significant enhancement of the N_2 fixation activity due to the formation of exposed Ti-OH sites. A linear relationship was observed between ammonia formation rate and amount of oxygen on the surface of Ti_3C_2 MXene.

Keywords: ammonia synthesis, nitrogen reduction reaction (NRR), electro-catalysis, electrochemical cells, Metal-Organic Frameworks (MOFs), coordination polymers, two-dimensional materials, 2D carbides and nitrides (MXenes)

Abstract (Italian)

L'azoto gioca un ruolo indispensabile per la vita sulla terra e per lo sviluppo degli esseri umani. Industrialmente, è necessario convertire l'azoto gassoso in ammoniaca (NH_3) per la produzione di fertilizzanti, in modo da integrare la quantità di azoto fissata spontaneamente in natura. Attualmente, l'unica tecnologia di sintesi dell'ammoniaca su scala industriale è il processo sviluppato da Haber e Bosch all'inizio del XX secolo che utilizza N_2 e H_2 come gas di alimentazione. Tuttavia, il processo Haber-Bosch richiede condizioni molto drastiche, apparecchiature complesse e porta ad un elevato consumo energetico, operando inoltre a bassi tassi di conversione che non sono coerenti con le esigenze sempre crescenti di sviluppo economico e sociale. In alternativa al metodo Haber-Bosch, l'elettrocatalisi rappresenta una delle vie più promettenti che possono integrare l'elettricità prodotta da tecnologie di energia rinnovabile con la produzione di ammoniaca a temperatura ambiente e a pressione atmosferica. Una sfida specifica è legata allo sviluppo di nuovi elettrocatalizzatori/elettrodi con l'obiettivo di ottenere una produzione di ammoniaca a basso costo, su larga scala e delocalizzata sul territorio.

Alla luce delle suddette questioni scientifiche fondamentali, questo lavoro di dottorato si concentra su tre aspetti principali legati alla reazione elettrocatalitica di riduzione dell'azoto (NRR): i) l’ingegneria e la progettazione dell'elettrocatalizzatore, ii) la progettazione dell'elettrodo e del dispositivo elettrochimico e iii) il miglioramento e l’ottimizzazione delle condizioni di reazione, per migliorarne le prestazioni nella sintesi dell'ammoniaca.

La maggior parte delle attività di ricerca di questo dottorato, dalla sintesi e caratterizzazione dei materiali elettrocatalitici all'assemblaggio/collaudo degli elettrodi in dispositivi elettrochimici non convenzionali, sono state svolte presso il laboratorio CASPE (Laboratorio di Catalisi per la Produzione e l'Energia Sostenibile) dell'Università di Messina. Durante i tre anni, un periodo di 12 mesi è stato inoltre trascorso in cotutela con l'École supérieure de chimie, physique, électronique de Lyon (CPE Lyon), dove sono state studiate tecniche di sintesi avanzate per la preparazione di elettrocatalizzatori a base organometallica da utilizzare come elettrodi cataliticamente attivi nella NRR.

La tesi di dottorato è organizzata in cinque capitoli principali. Il capitolo 1 si concentra sulle questioni di fissazione dell’azoto e sulla descrizione del processo industriale Haber-Bosch, con una panoramica sulle implicazioni generali relative al suo elevato fabbisogno energetico. Vengono poi presentati i metodi alternativi per la fissazione elettrochimica dell'azoto, con un'ampia descrizione dei vantaggi, legati alle condizioni più favorevoli (cioè temperatura ambiente e pressione atmosferica) e degli svantaggi, e discutendo gli elementi da sviluppare per una futura implementazione di questa tecnologia, includendo anche una descrizione del possibile meccanismo di reazione, ancora non del tutto chiaro in letteratura.

Il capitolo 2, invece, si riferisce alla descrizione dei materiali elettrocatalitici sviluppati in questo lavoro di dottorato per la preparazione degli elettrodi: 1) i “Metal-Organic Frameworks” (MOF), una classe di materiali porosi molto promettenti per le loro caratteristiche peculiari di elevata superficie, proprietà adattabili, funzionalità organica e porosità, oltre che per la possibilità di creare specifici siti attivi catalitici grazie sia ai gruppi funzionali che ai centri ionici metallici; 2) i MXeni, una classe di materiali a base di carburi o nitruri metallici con struttura bidimensionale (2D), che hanno recentemente attirato un grande interesse per una vasta gamma di applicazioni, tra cui la catalisi e la fissazione di N_2, per le loro proprietà uniche di conducibilità metallica e la natura idrofila delle superfici con terminali idrossilici o di ossigeno.

Nei capitoli 3-5 vengono presentati e discussi i risultati sperimentali. Il capitolo 3 riguarda la preparazione di una serie di elettrodi di MOF a base di Fe (Fe@Zn/SIM-1) e il loro test nella NRR utilizzando un reattore trifasico avanzato, che lavora in fase gassosa. Questo nuovo dispositivo funziona a temperatura ambiente e a pressione atmosferica, e possiede il controelettrodo e l’elettrodo di riferimento immersi in una semicella anodica (dove avviene l'ossidazione di H_2O a O_2) contenente un elettrolita liquido (l'anolita), mentre la semicella catodica per la NRR opera in fase gassosa senza elettrolita liquido. Questo tipo di reattore elettrocatalitico è quindi molto diverso dai reattori elettrocatalitici convenzionali che operano in fase liquida, con il grande vantaggio di evitare problematiche legate alla bassa solubilità e al trasporto di N_2 nell'elettrolita, e di permettere inoltre un più facile recupero dell'ammoniaca prodotta. I risultati ottenuti da questi test elettrocatalitici in fase gassosa sono stati molto utili per migliorare la progettazione degli elettrodi a base di MOF, evidenziando i limiti di questo tipo di materiali in termini di contenuto di N, stabilità e possibilità di preparare elettrocatalizzatori più avanzati mediante carbonizzazione. Un'ampia parte di questo capitolo è stata dedicata allo sviluppo di nuove strategie sperimentali per evitare i falsi positivi nella rilevazione dell'ammoniaca, che è uno degli argomenti più investigati negli ultimi due anni dai ricercatori che lavorano sulla NRR. Mentre in letteratura sono stati recentemente proposti protocolli molto accurati che utilizzano tecniche analitiche avanzate (basati sull’azoto marcato ${}^{15}N$), in questo lavoro viene invece suggerita una metodologia più semplice basata sull'analisi spettrofotometrica UV-visibile (accoppiata a test in bianco con gas inerti in luogo dell’azoto) che hanno permesso con successo di evitare contaminazioni da ammoniaca e identificare i falsi positivi, anche se tecniche analitiche più sofisticate sono sicuramente necessarie per confermare definitivamente la vera fonte di ammoniaca.

Nel capitolo 4 viene presentata una serie di materiali MOF migliorati (MOF UiO-66-$(COOH)_2$ a base di Fe o Fe e metalli alcalini), sintetizzati con la tecnica di reazione a scambio cationico per sostituire il protone dell'acido carbossilico con un catione di ferro. Rispetto ai materiali Fe@Zn/SIM-1, questa nuova classe di MOF è più stabile in acqua e non contiene atomi di azoto nella sua struttura. I risultati hanno dimostrato che il Fe@UiO-66-$(COOH)_2$ ottenuto mediante l'80% di scambio cationico (con un contenuto effettivo di Fe di circa 8% in peso) è stato il miglior elettrocatalizzatore testato tra i vari materiali MOF a base di Fe sintetizzati. Le prestazioni nella NRR dipendono fortemente dal design della cella e dell'elettrodo. Più in dettaglio, è stato ottenuto un rendimento di ammoniaca di $1.19\ \mu g \cdot h^{-1} \cdot mg_{cat}^{-2}$ con una configurazione di strati assemblati ed ordinati nel modo seguente: i) Nafion (la membrana), ii) MOF a base di Fe (l'elettrocatalizzatore), iii) il GDL (lo strato di diffusione gassosa a base di carbonio) e iv) un ulteriore strato di Fe-MOF. È stato anche esplorato l'effetto del voltaggio applicato, con un potenziale ottimale di -0.5 V vs RHE per massimizzare l'attività nella NRR e limitare la reazione collaterale di evoluzione dell'idrogeno. Inoltre, come attualmente utilizzato nei catalizzatori industriali per il processo Haber-Bosh, è stata studiata anche l'introduzione del potassio negli elettrocatalizzatori, al fine di facilitare il trasferimento di carica dagli ioni K^- verso la superficie del catalizzatore a base di ferro, bilanciando il chemisorbimento dissociativo tra H_2 e N_2, e sopprimendo le reazioni collaterali, migliorandone così sia l'attività che la stabilità. I risultati ottenuti sono molto promettenti, anche se sono necessari ulteriori studi per migliorare le loro prestazioni nella NRR, per superare le limitazioni legate ai materiali MOF stessi, soprattutto a causa della loro bassa conducibilità e stabilità.

Infine, il capitolo 5 si riferisce all'esplorazione di materiali avanzati, i MXeni (Ti_3C_2 MXeni), e al tentativo di sintetizzare una nanoarchitettura 3D partendo dalla loro forma bidimensionale. Per comprendere il ruolo della nanostruttura dei materiali MXeni nella NRR, "nanoribbons" (nano-nastri) di Ti_3C_2 sono stati trattati con KOH per ottenere una forma finale di strutture porose tridimensionali (3D). In particolare, l'obiettivo di questa parte di lavoro è stato quello di indagare come la conversione dei "nanoribbons" di Ti_3C_2 in strutture tridimensionali influenzi la reattività nella NRR condotta nel dispositivo elettrochimico in fase gassosa. È stata anche effettuata una caratterizzazione completa dei "nanoribbons" di MXeni (SEM, TEM, HRTEM, XRD, XPS e EDX). I risultati hanno mostrato che la nanostruttura tridimensionale porta ad un significativo miglioramento dell'attività di fissazione di N_2 a causa della formazione di siti esposti di Ti-OH. È stata anche osservata una relazione lineare tra il tasso di formazione di ammoniaca e la quantità di ossigeno sulla superficie dei Ti_3C_2 MXeni.

Parole chiave: sintesi di ammoniaca, reazione di riduzione dell'azoto (NRR), elettrocatalisi, celle elettrochimiche, strutture metallo-organiche (MOF), polimeri di coordinamento, materiali bidimensionali, carburi e nitruri 2D (MXeni)

Abstract (French)

L'azote joue un rôle indispensable pour toute vie sur terre et pour le développement des êtres humains. Industriellement, l'azote gazeux est converti en ammoniac (NH_3) et en engrais riches en azote pour compléter la quantité d'azote fixée spontanément par la nature. À l'heure actuelle, la seule technologie de synthèse de l'ammoniac à l'échelle industrielle est le procédé mis au point par Haber et Bosch au début du XXe siècle, qui utilise les phases gazeuses N_2 et H_2. Cependant, le procédé Haber-Bosch nécessite des conditions difficiles, des équipements complexes et une consommation d'énergie élevée, et fonctionne avec de faibles taux de conversion, ce qui est incompatible avec les exigences d'un développement durable. Par rapport à la méthode Haber-Bosch, l'électrocatalyse est l'une des voies prometteuses qui permet d'intégrer l'électricité produite à partir de technologies d'énergies renouvelables pour la production d'ammoniac à température ambiante et à pression ambiante. Un défi spécifique est lié au développement de nouveaux électrocatalyseurs/électrodes dans le but de parvenir à une production d'ammoniac à faible coût, à grande échelle et délocalisée.

Compte tenu ces défis scientifiques, ce travail de doctorat se concentre sur trois aspects principaux de la réaction électrocatalytique de réduction de l'azote (NRR) : i) ingénierie et conception de l'électrocatalyseur, ii) conception de l'électrode et de la cellule du dispositif électrochimique et iii) amélioration et optimisation des conditions de réaction, afin d'améliorer les performances de la synthèse de l'ammoniac.

La plupart des activités de recherche de ce travail de doctorat sur la synthèse et la caractérisation des matériaux électrocatalytiques et l'assemblage/le test des électrodes dans des dispositifs électrochimiques non conventionnels ont été menées au laboratoire CASPE (Laboratory of Catalysis for Sustainable Production and Energy) de l'université de Messine. En outre, une période de 12 mois a été passée en cotutelle avec l'École supérieure de chimie, physique, électronique de Lyon (CPE Lyon), où des voies de synthèse avancées ont été explorées pour la préparation d'électrocatalyseurs à base de composés organométalliques qui ont été utilisés comme électrodes plus actives dans la RRN.

Cette thèse de doctorat est organisée en cinq grands chapitres. Le chapitre 1 se concentre sur les questions de fixation de l'azote et sur la description du processus industriel de Haber-Bosch, avec un aperçu des implications générales liées à ses besoins élevés en énergie. Les méthodes alternatives basées sur la fixation électrochimique de l'azote sont ensuite présentées, avec une large description des avantages et des inconvénients liés aux conditions plus douces (c'est-à-dire la température ambiante et la pression atmosphérique) et en discutant des éléments à développer pour une future mise en œuvre de cette technologie, y compris une description du mécanisme de réaction possible, encore débattu dans la littérature.

Le chapitre 2 fait référence aux matériaux électrocatalytiques développés pour la préparation des électrodes : 1) les matériaux hybrides organiques-inorganiques de type MOF, une classe de matériaux poreux très prometteurs pour leurs caractéristiques particulières de surface spécifique élevée et leurs propriétés ajustables ainsi que pour la possibilité de créer des sites catalytiques actifs spécifiques grâce aux groupes fonctionnels et aux centres d'ions métalliques ; 2) les MXènes, une classe de matériaux en carbure ou nitrure de métal à structure bidimensionnelle (2D), qui ont récemment suscité un grand intérêt pour un large éventail d'applications, notamment la catalyse et la fixation de N_2, pour leurs propriétés uniques de conductivité métallique et de nature hydrophile des surfaces terminées par un hydroxyle ou un oxygène.

Les chapitres 3 à 5 présentent et analysent les résultats expérimentaux. Le chapitre 3 concerne la préparation d'une série d'électrodes à base de Fe-MOF (Fe@Zn/SIM-1) et leur test dans la réaction NRR en utilisant un réacteur triphasé de pointe, fonctionnant en phase gazeuse. Ce nouveau dispositif fonctionne à température ambiante et à la pression atmosphérique, avec des électrodes de comptage et de référence immergées dans une demi-cellule anodique (où se produit l'oxydation de H_2O en O_2) contenant un électrolyte liquide (l'anolyte), tandis que la demi-cellule cathodique pour le NRR fonctionne en phase gazeuse sans électrolyte liquide. Ce type de réacteur électrocatalytique est donc très différent des réacteurs électrocatalytiques classiques fonctionnant en phase liquide, avec les principaux avantages d'éviter les problèmes liés à la faible solubilité et au transport de N_2 dans l'électrolyte, et de permettre une récupération plus facile de l'ammoniac. Les résultats obtenus lors de ces essais électrocatalytiques en phase gazeuse ont été très utiles pour améliorer la conception des électrodes à base de MOFs, mettant en évidence les limites de ce type de matériaux en termes de teneur en N, de stabilité et de possibilité de préparer des électrocatalyseurs plus avancés par carbonisation. Une grande partie du chapitre 3 a été consacrée au développement de nouvelles stratégies expérimentales pour éviter les faux positifs dans la détection de l'ammoniac, qui est l'un des sujets les plus étudiés par les scientifiques travaillant dans la NRR ces deux dernières années. Comme des protocoles précis ont été récemment suggérés dans la littérature, utilisant également des techniques analytiques avancées (c'est-à-dire utilisant de l'azote marqué à ^{15}N), une méthodologie plus facile basée sur l'analyse spectrophotométrique UV-visible (couplée à des essais à blanc avec des gaz inertes) a été suggérée dans ce travail pour éviter les contaminations par l'ammoniac et les faux positifs, bien que des techniques analytiques plus sophistiquées puissent définitivement confirmer la source réelle d'ammoniac.

Dans le chapitre 4, une série de matériaux améliorés à base de Fe-MOF (incluant un dopage additionel par un métal alcalin du MOF UiO-66-$(COOH)_2$), synthétisés par une technique de réaction d'échange de cations pour remplacer le proton de l'acide carboxylique par un cation de fer, sont présentés. En ce qui concerne le Fe@Zn/SIM-1, cette nouvelle classe de MOF est plus stable dans l'eau et ne contient pas d'atomes d'azote dans sa structure. Les résultats ont montré que l'échange cationique à 80 % Fe@UiO-66-$(COOH)_2$ (avec une teneur effective en Fe d'environ 8 % en poids) était le meilleur électrocatalyseur parmi les matériaux synthétisés de MOF à base de Fe testés. Les performances du NRR dépendaient fortement de la conception de la cellule et de l'électrode. Plus en détail, un rendement en ammoniac de 1.19 $\mu g \cdot h^{-1} \cdot mg_{cat}^{-2}$ a été obtenu avec une configuration d'assemblage de couches ordonnées comme i) Nafion (la membrane), ii) MOF à base de Fe (l'électrocatalyseur), iii) GDL (la couche de diffusion de gaz carbonique) et iv) une autre couche de Fe-MOF. L'effet de la tension appliquée a également été exploré, indiquant une tension optimale de -0,5 V par rapport à la RHE pour maximiser l'activité dans le NRR et limiter la réaction latérale d'évolution de l'hydrogène. En outre, comme c'est le cas actuellement dans les catalyseurs industriels pour le procédé Haber-Bosh, l'introduction de potassium dans les électrocatalyseurs a également été étudiée, afin de faciliter le transfert de charge des ions K^- à la surface du catalyseur à base de fer, en équilibrant la chimisorption dissociative entre H_2 et N_2, et en supprimant les réactions secondaires, ce qui améliore à la fois l'activité et la stabilité. Ces résultats étaient très prometteurs, bien qu'une nouvelle expérimentation soit nécessaire pour améliorer leurs performances dans les NRR, afin de surmonter les limitations liées aux matériaux MOF eux-mêmes, principalement en raison de leur faible conductivité et de leur stabilité.

Enfin, le chapitre 5 fait référence à l'exploration des matériaux avancés à base de MXène (Ti_3C_2 MXène) et à la tentative de synthèse d'une nanoarchitecture 3D à partir de catalyseurs à base de MXène en 2D. Pour comprendre le rôle de la nanostructure des matériaux à base de MXène dans la NRR, des nanofeuilles de Ti_3C_2 ont été traitées au KOH pour obtenir une forme finale de nanorubans à armature poreuse tridimensionnelle (3D). Plus précisément, l'objectif de cette recherche était d'étudier comment la conversion des nanofeuilles de Ti_3C_2 en nanorubans tridimensionnels influençait la réactivité du NRR dans le dispositif électrochimique en phase gazeuse. Une caractérisation complète des nanorubans MXenes (SEM, TEM, HRTEM, XRD, XPS et EDX) a également été présentée. Les résultats ont montré que la nanostructure de type 3D (nanorubans) conduit à une amélioration significative de l'activité de fixation du N_2 en raison de la formation de sites Ti-OH exposés. Une relation linéaire a été observée entre le taux de formation d'ammoniac et la quantité d'oxygène à la surface du Ti_3C_2 MXene.

Mots clés : synthèse de l'ammoniac, réaction de réduction de l'azote (NRR), électro-catalyse, cellules électrochimiques, metal-organic frameworks (MOF), polymères de coordination, matériaux bidimensionnels, carbures et nitrures 2D (MXenes)

Table of Contents

List of Figures

List of Tables

1 Introduction

1.1 An overview of electrocatalytic conversion of small molecules

Nature is inclined to light elements developing complexity. Small molecules play an important role as building blocks for fuels, chemicals, and fertilizers [1]. Key small molecules such as such as H_2, H_2O, O_2, N_2, CO_2, and CH_4 are the important ingredients for energy storage and high value-added products. H_2 and O_2 provide clean energy through fuel cells, which are formed by electrocatalytic water splitting [2]. N_2 and H_2 are used to produce ammonia, which is an essential constituent of fertilizers produced primarily from the Haber–Bosch process [3]. Catalytic conversion of one-carbon (C1) molecules, such as CO, CO_2, CH_4, and CH_3OH, into fuels and value-added chemicals have been receiving large attention because of its close correlation to energy and environmental implications [4] [5]. Small molecule activation and conversion reactions are significant in many chemical processes and have been extensively investigated by scientists. The centralized production of fuels, chemicals, and fertilizers by thermocatalytic processes sustained by fossil resources is a pillar of modern societies. Developing sustainable, fossil-free pathways to produce fuels and chemicals of global importance is essential. Electrocatalysis is a key element for the development of sustainable chemical processes utilizing renewable energy.

Figure 1.1 shows a scheme of a sustainable energy landscape based on electrocatalysis, including hydrogen, hydrocarbons, oxygenates, and ammonia, by either replacing or working in concert with conventional energy production. Earth’s atmosphere provides a universal feedstock of water, carbon dioxide, and nitrogen.

The water-splitting reaction produces a sustainable source of hydrogen, which can be used to produce clean electricity in fuel cells [6]. Meanwhile, the hydrogen oxidation and oxygen reduction reactions (ORR) convert chemical energy into electrical energy [7]. CO_2 captured from the atmosphere or directly from point sources could become a feedstock for fuels, commodity chemicals, fine chemicals, and precursors to polymers and plastics through electrocatalytic CO_2 reduction reaction (CO_2RR)[8]. The direct electrocatalytic synthesis of ammonia from N_2 and H_2O would allow for the production of fertilizers sustainably and locally at the point of application and at the required concentration, eliminating distribution costs stemming from the inflexibly large-scale, centralized Haber-Bosch process [9]. From this above, this general area is indicated as "Solar-driven chemistry", where the term "solar" indicates all the challenging new area of syntheses where the energy to drive the reaction is not provided by fossil fuels (i.e. thermal energy). Electrocatalysis is at the core of this challenge, where the term electrocatalysis indicates the possibility to drive the electrochemical reactions through the use of catalysis concepts that will allow to i) lower the required energy (i.e. by reducing the overpotential and loss of energy), ii) improve the Faradaic efficiency and iii) especially control the selectivity.

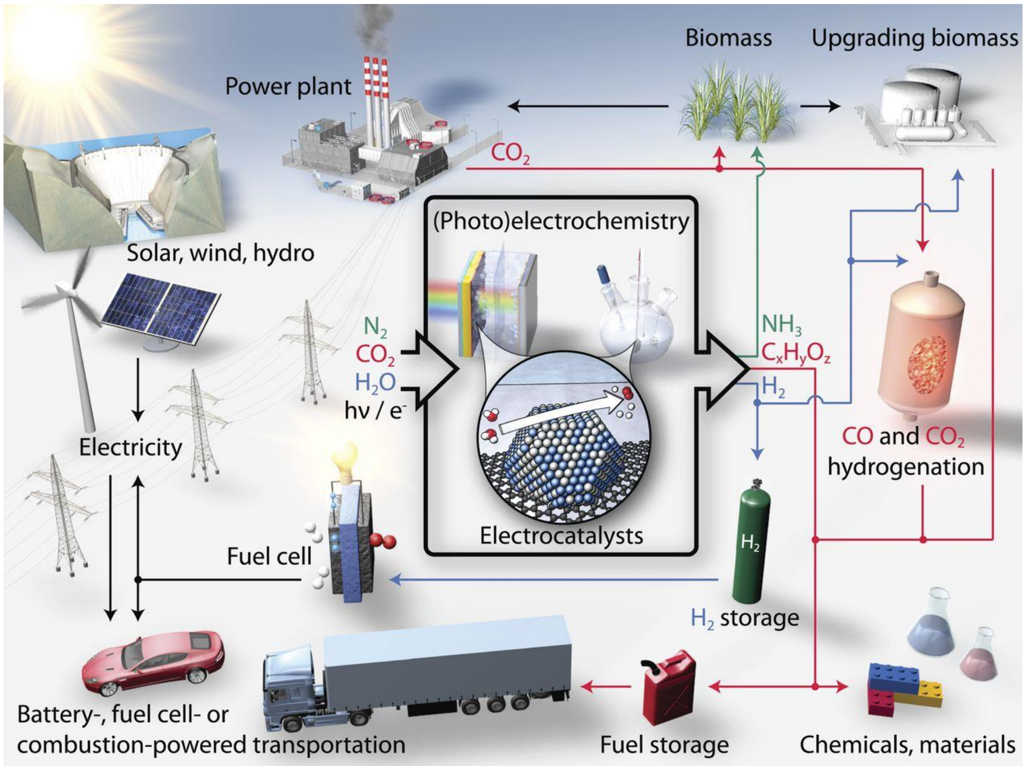

Figure 1.1 Schematic of a sustainable energy landscape based on electrocatalysis.[1] Copyright 2017, Science.

1.2 Nitrogen fixation

Nitrogen is necessary for all known forms of life on Earth. Figure 1.2 shows the nitrogen cycle in a Terrestrial Ecosystem [10]. Important processes in the nitrogen cycle include fixation, ammonification, nitrification, and denitrification. Nitrogen comes from biofixation, atmospheric deposition, and the recycling of crop residues and animal manures. Conversion of nitrogen into nitrates and nitrites through atmospheric, industrial and biological processes is called as nitrogen fixation. When a plant or animal dies or an animal expels waste, the initial form of nitrogen is organic. Bacteria or fungi convert the organic nitrogen within the remains back into ammonium (NH_4^+), a process called ammonification or mineralization. The nitrification process is dependent on the activities of a diverse assemblage of microorganisms, such as bacteria, archaea, and fungi. The denitrification process is performed by bacterial species such as Pseudomonas and Clostridium in anaerobic conditions. They use the nitrate as an electron acceptor in the place of oxygen during respiration. The anaerobic ammonium oxidation (anammox) process makes up a major proportion of nitrogen conversion in the oceans [11], while the nitrogen fixation and ammonification provide all the nitrogen into the nitrogen cycle. The atmospheric nitrogen has limited availability for biological use, leading to a scarcity of usable nitrogen in many types of ecosystems. Thus, the limitation for the nitrogen cycle is the nitrogen fixation process.

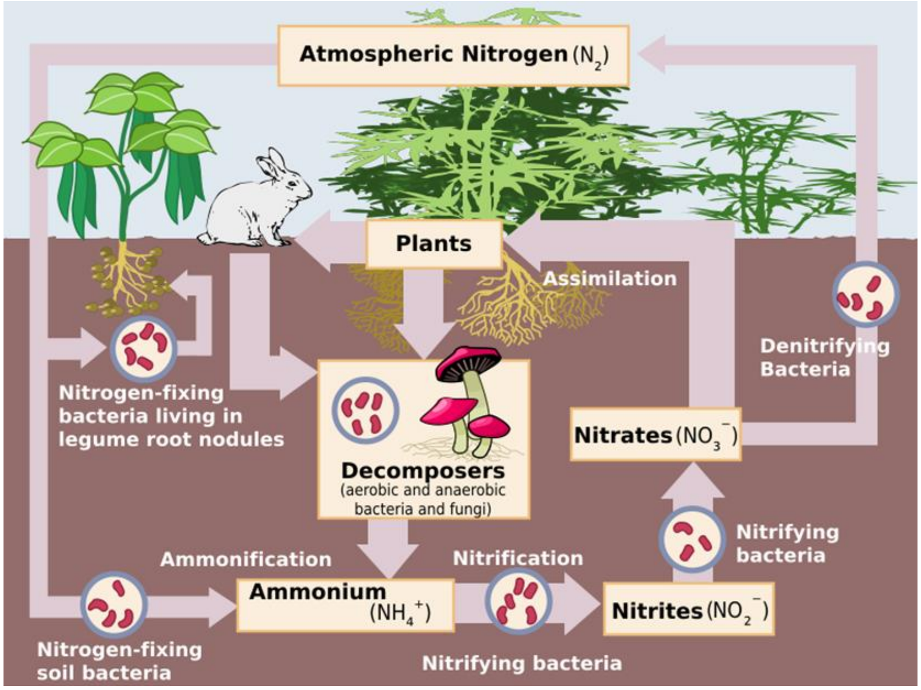

Figure 1.2 Nitrogen cycle in a Terrestrial Ecosystem [10].

Ammonia is essential for fertilisers in order to feed the World's growing population. Indeed, it is estimated that between a third and half of us would starve to death if ammonia-based fertilisers were not available, and ammonia's industrial-scale synthesis from its elements is arguably the single biggest scientific discovery of the 20th century [12].

1.3 Industrial ammonia production: Haber-Bosch process

The conventional route of producing ammonia is by the Haber-Bosch process named after two Scientists Fritz Haber and Carl Bosch [13]. The process requires the reaction of hydrogen and nitrogen over an iron based catalyst at temperatures in the vicinity of 400° to 650° C and pressures ranging from 200 to 400 atmospheres, the scheme of the Haber-Bosch process is shown in Figure 1.3. Over 200 million metric tons of ammonia per annum are produced by this process worldwide [14]. About 80% of the ammonia produced globally is used for nitrogen based fertiliser production [15]. The remaining 20% of the ammonia production is used in explosives, pharmaceuticals, refrigeration, cleaning products and many other industrial processes [16]. Ammonia synthesis reaction in the Haber-Bosch process is given as:

$$3H_2 + N_2 \rightarrow 2NH_3 \quad \Delta H_{298.15K} = -91.88\ \mathrm{kJ\ mol^{-1}},\ \Delta S_{298.15K} = -198.09\ \mathrm{J\ mol^{-1}\ K^{-1}}$$

High temperatures are needed in order to offset the sluggish kinetics of this reaction; however, the thermodynamics of this process favours ammonia decomposition to nitrogen and hydrogen at elevated temperatures and hence the need for high pressure. Including the energy required to obtain the pure feed gases, pressurization and so on, ammonia synthesis by the Haber Bosch process typically requires an energy input of around 485 kJ mol^{-1} [17]. This is a large amount of energy, especially in comparison to natural systems, and therefore methods reducing this requirement are highly desirable but at the same time very challenging. This has led to the development of alternative routes to synthesise ammonia, having the potential to overcome the many limitations of the conventional catalytic reactor, such as low ammonia conversion, severe environmental pollution and high energy consumption [18].

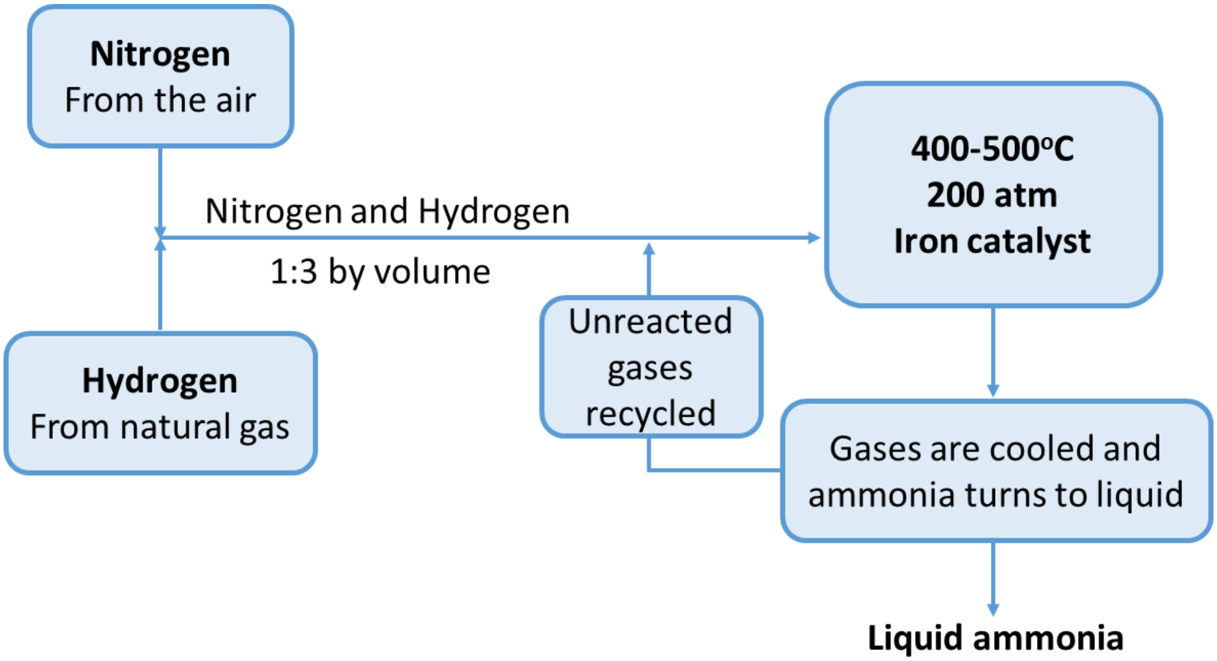

Figure 1.3 Scheme of the Haber Bosch process.

1.4 Electrocatalytic synthesis of NH_3 -Nitrogen reduction reaction (NRR)

1.4.1 Advantages of electrochemical Nitrogen fixation

Various alternative approaches for ammonia synthesis have been investigated, including plasma-induced methods, biological methods, methods based on metallo complexes, photocatalytic methods, and electrochemical methods. Comparing with Haber Bosch process, all these methods are in the beginning state, waiting the breakthrough [19] [20].

Among these methods, ammonia can be synthesised by a number of electrochemical routes and many different electrolytic systems are currently under development. It has been forecast that electrochemical routes can save more than 20% of the energy consumption as compared to the conventional Haber-Bosch route [21]. Ammonia could be produced under less demanding conditions in electrochemical methods, so there would be the potential for smaller devices to be used to generate ammonia in a decentralized manner for local consumption. Moreover, there will be no greenhouse gas emission and no natural gas consumption, if H_2O is used as the hydrogen source.

In brief, electrochemical ammonia production is a promising route for ammonia production, due to the following reasons:

- high pressure and temperature conditions are not essential;
- H_2O instead of H_2 can be used as the hydrogen source;

- comparing with the heating system in Haber-Bosch process, which can activate both reactants and products (reverse reactions), the electricity can selectively be used for the reactant with a suitable catalyst.
- renewable and clean electricity, such as solar and wind energy, can be used for ammonia synthesis minimizing CO_2 emissions;
- process scaling down without decreasing the energy efficiency can be addressed;
- this solution offers attractive possibilities for a distributed production of fertilizers.

1.4.2 Reaction mechanisms of NRR

The proposed mechanisms for electrochemical reduction of N_2 to NH_3 can generally be classified into 1) the dissociative pathway and 2) the associative pathway [23]. In the dissociative pathway, the $N{\equiv}N$ triple bond is broken before the addition of H to the N atoms (Figure 1.4a), whereas in the associative pathway, the N-N bond is cleaved simultaneously with the release of the first molecule of NH_3. The associative pathway can be further divided into the distal pathway and the alternating pathway according to different hydrogenation sequences. In the distal pathway, the remote nitrogen atom is hydrogenated first and released as NH_3, whereas in the alternating pathway, the two N atoms are hydrogenated simultaneously (Figure 1.4b) [24]. Notably, the enzymatic pathway, which belongs to the associative pathway, exhibits a distinctive feature of its side-on adsorption mode of N atoms (Figure 1.4c), instead of an end-on adsorption mode of N atoms proposed on most heterogeneous surfaces.

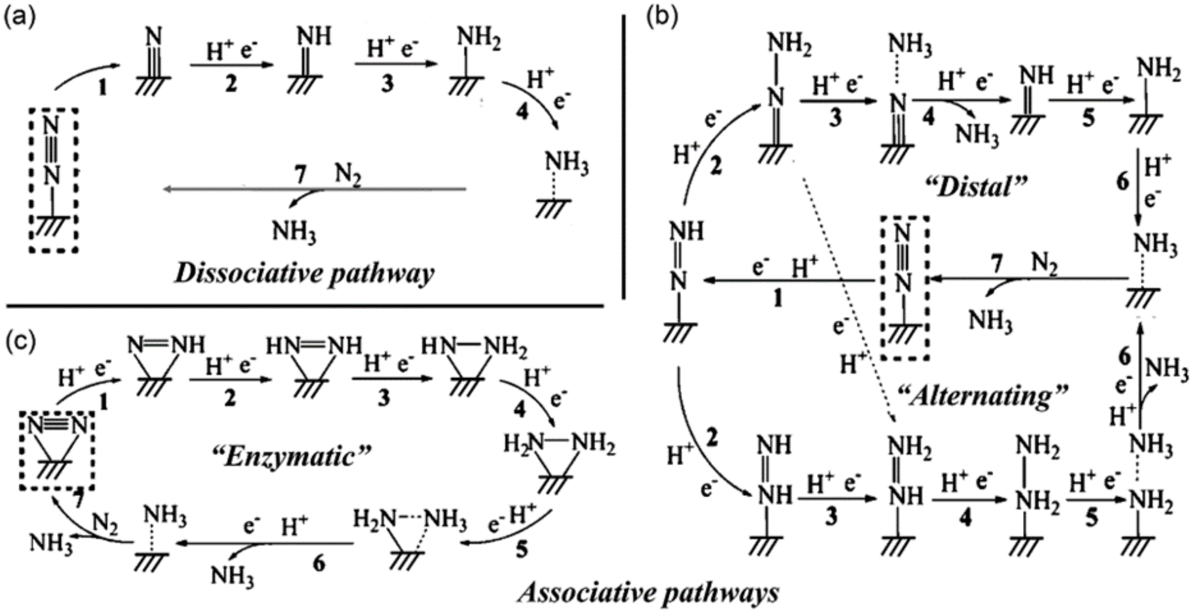

Figure 1.4 Schematic depiction of the dissociative pathway and the associative pathways (including distal, alternating, and enzymatic pathway) for catalytic conversion of N_2 to NH_3 Reproduced with permission [22]. Copyright 2016, American Chemical Society.

1.4.3 Electrochemical systems of NRR

Electrochemical nitrogen reduction is a complicated system with several parts, where optimized conditions are important for catalysts to reach their full potentiality, including a combination of reactor configuration, electrolyte, temperature, pressure, and feeding gas.

The electrolyte. Electrolyte is a key factor in the electrochemical NRR process. An electrolyte with a limited proton transfer rate and high solubility of N_2 can efficiently improve the reaction efficiency and selectivity. Currently, electrolytes can be divided into four types: liquid electrolytes, polymer electrolytes, solid electrolytes and molten salt electrolytes.

At present, NRR in liquid electrolyte is one of the most practical reactions under ambient conditions owing to its energy-saving, simple and cost-effective properties. Generally, the reaction chambers are filled with liquid electrolytes such as $KHCO_3$ aqueous solution [9], KOH aqueous solution [25], HCl aqueous solution [26], Li-mediated electrolytes [27], organic mixture electrolytes such as, tetrahydrofuran/$LiClO_4$/ethanol solution[28], 2-propanol/ deionized water solution and ethylenediamine/LiCl solution[29], and ionic liquid[30]. It is worth mentioning that the water-based ("aqueous") solutions of ions are the most widely used electrolytes in recent years due to their low price, easy operability, and diversity of modification.

Molten salt electrolytes have been intensively researched due to their high ionic conductivity and relatively mild reaction conditions, wide electrochemical window, thermodynamic stability and low vapor pressure [31]. Licht et al. reported the use of molten hydroxide (NaOH/KOH) suspension of nano-Fe_2O_3 as electrolyte/catalyst to achieve high rates of NH_3 generation from air and water [32]. This concept provides a new electrochemical pathway to produce NH_3 by using water as proton sources in one pot without a separator. The use of molten salt electrolytes generally leads to higher ammonia production rates compared with liquid electrolyte systems. However, when molten salts are used as electrolyte, higher reaction temperatures are required, which means more energy necessary for the process compared with other options working at room temperature.

Among the other electrolytes, solid state electrolytes can be used under high temperature with excellent ion conductivity [33], which can largely promote the reaction kinetic and obtain high NH_3 production rate. This electrolyte concept can lead to higher stability and easier separation of formed ammonia. The first work with solid electrolyte on electrochemical ammonia synthesis was published by M. Stoukides et al. in 1998 on Science [34]. Another type of solid electrolytes is polymer-gel conductive electrolytes in PEM-type cells. It was reported that NRR catalysts behave quite differently in aqueous solutions and PEM cells [9] [19]. In PEM cells, the NRR actually takes place at the gas-solid interface instead of the gas-liquid-solid three-phase interface in aqueous solution, with protons provided by the solid electrolytes. Proton conductive polymers, represented by Nafion membranes, are the most widely used polymer electrolytes in electrochemistry due to their high proton conductivity. Catalysts in PEM cells generally exhibit much lower Faraday efficiency but higher NH_3 yield in some cases compared to that in aqueous solution in conventional H-type cells[9] [19]. The utilization of a PEM cell can also avoid the stability issue of some water- or acid/base-sensitive catalysts in aqueous electrolyte.

In general, electrolytic cells based on solid electrolyte membrane are more versatile as they allow easy separation of hydrogen feed from ammonia product.

The electrochemical cell. Different kinds of electrochemical cell have been developed with the use of either liquid or solid electrolytes. The electrochemical reactors reported in recent experimental investigations can be divided into four categories based on the differences in the cell configuration, as illustrated in Figure 1.5 [23].

The back-to-back cell illustrated in Figure 1.5a with solid-state electrolyte has been widely used for solid-state electrochemical synthesis of NH_3 over a wide temperature range (25–800 °C) [35].

The polymer electrolyte membrane (PEM)-type cell is shown in Figure 1.5b. A recent research at the University of Messina [9] demonstrated direct synthesis of NH_3 from N_2 and H_2O under room temperature and atmospheric pressure over iron oxide supported on carbon nanotubes (Fe_2O_3-CNT) as cathode catalyst in an PEM-type cell.

Generally, the H-type cell is chosen for a liquid-electrolyte reaction. As shown in Figure 1.5c, both the working electrode and the reference electrode are located in the cathode chamber, making it more accurate to measure the applied potentials, exerted on the working electrode than using the PEM-type cell, in which the reference electrode has to be placed in the anode chamber filled with electrolyte. However, the H-type cell with Nafion membrane as the separator exhibits issues of ammonia/ ammonium crossover effect [23].

The single chamber cell is shown in Figure 1.5d. The main drawback of this cell refers to the fact that the products generated at the cathode may be oxidized at the anode. In contrast, the double-chamber cell with an ion-exchange membrane as the separator makes it possible to prevent further oxidation of the gaseous products by allowing the transfer of only the desired ions.

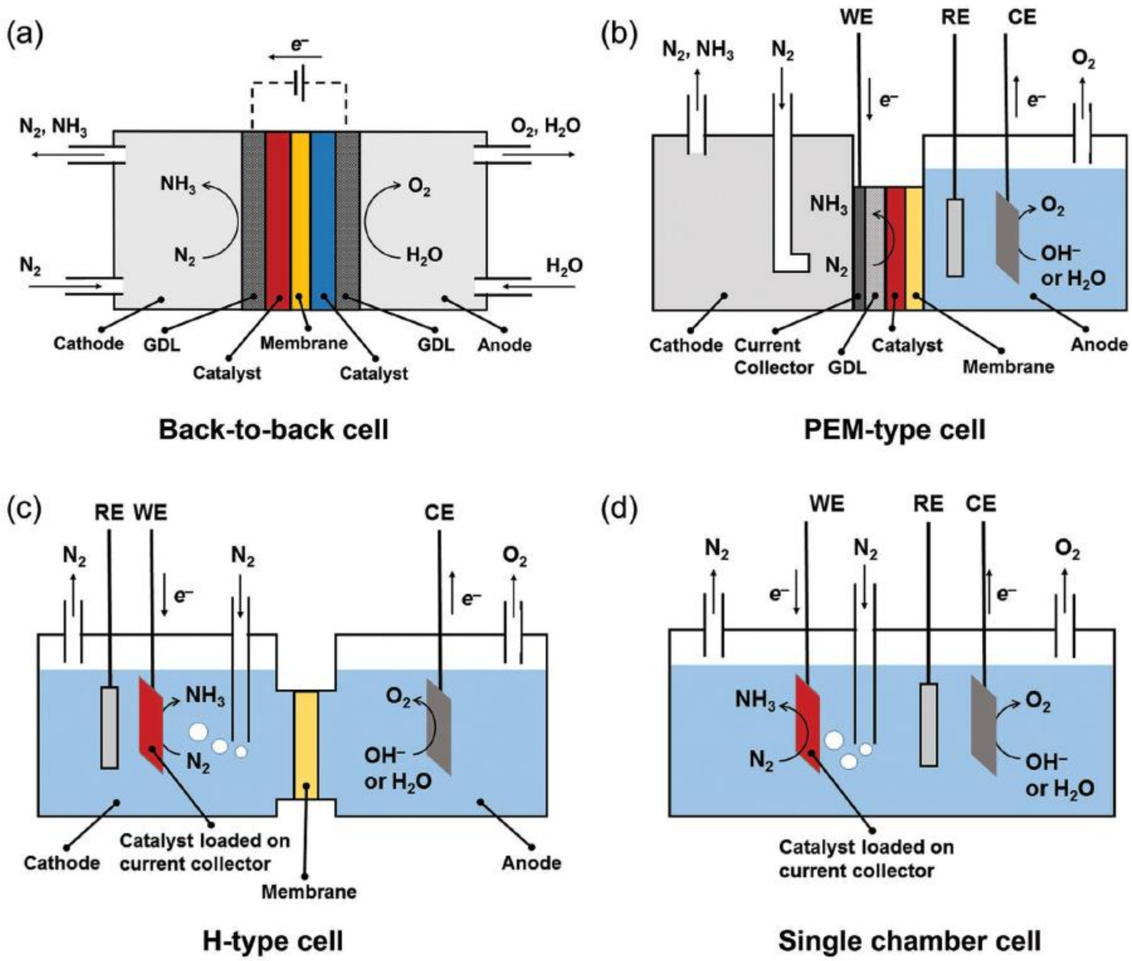

Figure 1.5 (a-d) Schematics of different cell configurations for electrocatalytic NRR at ambient conditions [23].

To choose the right reaction system, a rational design of the whole electrochemical system including electrode materials, electrolytes, and cell configurations, is needed.

1.4.4 Electrocatalysts for NRR

Electrocatalysts are the core components of electrocatalytic NRR systems, which can promote the dissociation of N≡N at relatively low energy barrier. Developing the catalysts with high activity for NRR and suppression of HER is the key factor for the development of electrocatalytic NH_3 synthesis. The catalysts can be divided into four types: i) metal catalysts, ii) metal-based oxide/nitride/carbide catalysts, iii) single-atom–based catalysts and iv) carbonaceous catalysts.

NRR on Metal Surface. A pure metal surface is the simplest model to be analysed for electrochemical ammonia formation. Precious metals and transition metals [36–38] are the most widely used pure-metal electrocatalysts for NRR, owing to their unique d-electrons [36]. Noble metals can easily adsorb molecules for electrochemical reaction and show good adsorption and desorption of new molecules. In addition, noble metal catalysts have excellent chemical durability, can maintain high catalytic activity, and are more resistant to corrosion in some acid/alkaline electrolytes. In a landmark work in 2012[36], Skúlason et al. evaluated the catalytic activity toward NRR on a range of flat and stepped transition metal surfaces by assuming that the activation energy scales with the free energy difference in each elementary step of NRR. Fe and Mo were the most active surfaces for ammonia formation. However, these surfaces were predicted to be more active at promoting HER rather than NRR. The flat metal surfaces of some early transition metals such as Sc, Y, Ti, and Zr are expected to bind N-adatoms more strongly than H-adatoms, allowing for the reduction of N_2 to NH_3 at a theoretical applied bias of ≈ -1.0 to -1.5 V vs NHE. However, these early transition metal surfaces are also known to easily form oxides so that the question remains whether they can be effective NRR catalysts or not. Yan and co-workers fabricated Au nanoparticles with exposed facets, different diameters, and amorphous structures. They achieved about 4% Faradaic efficiency using tetrahexahedral Au nanorods [37], ≈ 8% Faradaic efficiency using TiO_2-supported, size-controlled Au nanoparticles by tannic acid reduction method [26],[19] and ≈10% Faradaic efficiency on amorphous Au/CeO_x-rGO, which possessed a high concentration of unsaturated sites for N_2 fixation [38].

NRR on Metal Oxide/Nitride/Carbide Surface. On the background of electrochemical NH_3 synthesis from N_2 and steam electrolysis in molten hydroxide suspensions of nano-Fe_2O_3 reported by Licht et al [32], iron oxide has drawn strong attention as potential electrocatalyst toward NRR under more benign conditions. The NRR mechanism was identified to follow the associative pathway, and the most demanding step is the addition of the first proton to the adsorbed molecular nitrogen, which requires an applied bias of -1.84 V vs NHE for the Fe-Fe-O_3- (Fe-O_3-Fe-) surface. Recently, many metal oxides in the rutile structure was investigated, such as NbO_2, ReO_2, and TaO_2 with low onset potentials of -0.57, -1.07, and -1.21 V vs SHE, respectively [39].

Metal nitrides can be more active than pure metal catalysts toward NRR with respect to the competing HER. Recently, Zhang and co-workers reported that pure MoN_2 nanosheets demonstrated excellent performance for N_2 adsorption and activation at room temperature, but required large energy input for surface refreshment [40].

NRR on Single-Atom–Based Surface Single-atom catalysts (SACs), composed of isolated metal atoms anchored to support, have emerged as promising candidates for heterogeneous catalysis. In 2014, Tian and co-workers evaluated the catalytic profile of a molybdenum–graphene-based catalyst (Mo/N-doped grapheme with a $C_{33}H_{15}MoN_3$ model) for nitrogen fixation [41]. The Mo/N that acts as active centers, the graphene periphery region that acts as an electron donor or acceptor (i.e., an electron reservoir) and provides electrons for protonation and reduction, and the graphene body that acts as electron bridge for electron transportation.

NRR on Carbonaceous Catalysts. Carbon-based catalysts could be attractive alternatives to transition metal catalysts for electrolytic ammonia synthesis because of low selectivity for hydrogen evolution. The earliest report of carbonaceous catalyst for N_2 fixation was based on H-terminated B-doped diamonds with negative electron affinity [42]. Its conduction band lies on an absolutely negative potential for directly coupling of N_2 and electrons without hydrogenation. Song et al. reported a highly textured physical catalyst, composed of N-doped carbon nanospikes, that electrochemically reduces dissolved N_2 with the maximum production rate is 97.18 ± 7.13 μg h^{-1} cm^{-2} [43]. The catalyst has a surface composed of sharp spikes, which concentrates the electric field at the tips, thereby promoting the electroreduction of dissolved N_2 molecules near the electrode.

Carbonaceous catalysts can also be used as carrier materials for metal nanoparticles (NPs) in NRR. Recently, Quan and co-workers produced N-doped porous carbon from the zeolite imidazolate framework pyrolysis process possessing high N_2 contents and tunable N species, which were expected to promote chemisorption and dissociation of N_2 molecules, and thereby enhance the kinetics of N_2 fixation [44].

1.5 Objectives of the thesis

The electrocatalytic reduction of nitrogen, as an emerging electrocatalytic reaction, has attracted increasing attention from researchers in recent years. The performances of ammonia electrochemical synthesis can be evaluated from two parameters: i) the ammonia production rate (the total amount of ammonia produced per unit cell area and per unit time, usually measured in $mol·cm^{-2}·s^{-1}$) and ii) the conversion rate related to current efficiency of the process. In particular, with the hydrogen evolution reaction being dominant in most electrochemical systems, most electrons and protons are involved in H_2 evolution rather than reducing N_2 to ammonia, resulting in low Faradaic efficiencies [45].

In general, higher Faradaic efficiencies can be obtained at very low current densities, but the ammonia formation rate is too low under these conditions [3]. Giddey et al [3]. suggested that an ammonia formation rate close to 10^{-6} $mol·cm^{-2}·s^{-1}$ and a Faradaic efficiency up to 50% would be quite reasonable for commercial systems. However, the ammonia production rates achieved so far are lower than 10^{-6} $mol·cm^{-2}·h^{-1}$ and most of the electrochemical ammonia production from N_2 and H_2O under ambient conditions reported the performance with Faradaic efficiencies (FEs) less than 30% [45].These ammonia synthesis rates are too low and are due to H^+ flux being too low through the electrolytes, or the slow reaction kinetics at the electrode/electrolyte interface on the ammonia production side. It is to remark that, while there is a substantial scope for the development of electrochemical processes for ammonia synthesis, and the low-pressure operation is an advantage, the technology is at an early stage of research and the development requires significant advances in catalysts on ammonia production side.

The principal goal of this thesis is thus to develop new type of advanced electrodes for ammonia electro-synthesis from nitrogen and water as hydrogen source, at room temperature and atmospheric pressure, which is considered to be a sustainable way to produce ammonia. The PhD thesis will investigate i) the synthesis and advanced characterization (using a combination of techniques) of the electrocatalysts/electrodes, ii) the electrochemical characterization of these materials and the testing of the nitrogen reduction reaction, iii) the engineering design of the cell and related electrodes, optimized to attain the maximum benefit in electrochemical syntheses.

In this thesis, Fe based MOFs and MXene were chosen for the promising catalysts for nitrogen reduction reaction. The detail information and the main properties of the materials were described in chapter 2.

In chapter 3, Fe-MOF-based (Fe@Zn/SIM-1) electrodes were prepared and assembled to be used in ammonia reduction process by using an advanced engineered three-phase reactor, working in gas-phase. The identification and elimination of contamination in electrochemical nitrogen reduction studies were discussed in depth at the same time.

In chapter 4, a series of improved Fe-based and Fe-alkali metal-based MOF UiO-66-$(COOH)_2$ were synthesized by cation exchange reaction technique. The cell design and reaction condition was optimised through a series of experimental protocols.

In chapter 5, the fabrication of a novel 3D porous framework of alkalized Ti_3C_2 MNRs derived from Ti_3C_2 MNSs in KOH solution has been demonstrated. The structural difference will be deeply analyzed and discussed. By analyzing electrochemical test results and material characterization, the reaction mechanism and the active sites were discussed in depth.

1.6 References

[1] Seh, Z. W.; Kibsgaard, J.; Dickens, C. F.; Chorkendorff, I.; Nørskov, J. K.; Jaramillo, T. F., Combining theory and experiment in electrocatalysis: Insights into materials design. *Science* **2017,** *355* (6321).

[2] You, B.; Sun, Y., Innovative strategies for electrocatalytic water splitting. *Accounts of chemical research* **2018,** *51* (7), 1571-1580.

[3] Giddey, S.; Badwal, S.; Kulkarni, A., Review of electrochemical ammonia production technologies and materials. *International Journal of Hydrogen Energy* **2013,** *38* (34), 14576-14594.

[4] Meng, X.; Cui, X.; Rajan, N. P.; Yu, L.; Deng, D.; Bao, X., Direct Methane Conversion under Mild Condition by Thermo-, Electro-, or Photocatalysis. *Chem* **2019,** *5* (9), 2296-2325.

[5] Wang, B.; Albarracín-Suazo, S.; Pagán-Torres, Y.; Nikolla, E., Advances in methane conversion processes. *Catalysis Today* **2017,** *285*, 147-158.

[6] Benck, J. D.; Hellstern, T. R.; Kibsgaard, J.; Chakthranont, P.; Jaramillo, T. F., Catalyzing the hydrogen evolution reaction (HER) with molybdenum sulfide nanomaterials. *Acs Catalysis* **2014,** *4* (11), 3957-3971.

[7] Tian, J.; Liu, Q.; Asiri, A. M.; Sun, X., Self-supported nanoporous cobalt phosphide nanowire arrays: an efficient 3D hydrogen-evolving cathode over the wide range of pH 0-14. *Journal of the American Chemical Society* **2014,** *136* (21), 7587-7590.

[8] Centi, G.; Quadrelli, E. A.; Perathoner, S., Catalysis for CO_2 conversion: a key technology for rapid introduction of renewable energy in the value chain of chemical industries. *Energy Environmental Science* **2013,** *6* (6), 1711-1731.

[9] Chen, S.; Perathoner, S.; Ampelli, C.; Mebrahtu, C.; Su, D.; Centi, G., Electrocatalytic synthesis of ammonia at room temperature and atmospheric pressure from water and nitrogen on a carbon-nanotube-based electrocatalyst. *Angewandte Chemie International Edition* **2017,** *56* (10), 2699-2703.

[10] [File:Nitrogen Cycle.svg|Nitrogen Cycle] https://commons.wikimedia.org/wiki/File:Nitrogen_Cycle.svg, 2020-12-04

[11] Rios-Del Toro, E. E.; Cervantes, F. J., Anaerobic ammonium oxidation in marine environments: contribution to biogeochemical cycles and biotechnological developments for wastewater treatment. *Reviews in Environmental Science Bio/Technology* **2019,** *18* (1), 11-27.

[12] US Geological Survey, Nitrogen (Fixed)—Ammonia: http://minerals.usgs.gov/minerals/pubs/commodity/nitrogen/mcs-2015-nitro.pdf (accessed March, 2016).

[13] Avery, W., A role for ammonia in the hydrogen economy. *International journal of hydrogen energy* **1988,** *13* (12), 761-773.

[14] Anantharaman, B.; Hazarika, S.; Ahmad, T.; Nagvekar, M.; Ariyapadi, S.; Gualy, R. In *Coal gasification technology for ammonia plants*, PROCEEDINGS OF THE ASIA NITROGEN & SYNGAS 2012 CONFERENCE. Kuala Lumpur, Malaysia, 2012.

[15] Market study: ammonia (UC-3705). Cerasena Market Intelligence Consulting; October 2012. p. 530.

[16] Schiller M. Industrial uses of ammonia. Available at: http://www.easychem.com.au/monitoring-and-management/maximising-production/industrial-uses-of-ammonia [cited 4 April 2013].

[17] Appl, M., Ammonia. Ullmann's Encyclopedia of Industrial Chemistry, 153. 2006.

[18] Marnellos, G.; Stoukides, M., Ammonia synthesis at atmospheric pressure. *Science* **1998,** *282* (5386), 98-100.

[19] Schlögl, R., Catalytic Synthesis of Ammonia-A "Never - Ending Story"? *Angewandte Chemie International Edition* **2003,** *42* (18), 2004-2008.

[20] Broda, H.; Tuczek, F., Catalytic Ammonia Synthesis in Homogeneous Solution—Biomimetic at Last? *Angewandte Chemie International Edition* **2014,** *53* (3), 632-634.

[21] Lipman, T.; Shah, N., Ammonia as an alternative energy storage medium for hydrogen fuel cells: scientific and technical review for near-term stationary power demonstration projects, final report. **2007**.

[22] Li, X.-F.; Li, Q.-K.; Cheng, J.; Liu, L.; Yan, Q.; Wu, Y.; Zhang, X.-H.; Wang, Z.-Y.; Qiu, Q.; Luo, Y., Conversion of dinitrogen to ammonia by FeN_3-embedded graphene. *Journal of the American Chemical Society* **2016,** *138* (28), 8706-8709.

[23] Cui, X.; Tang, C.; Zhang, Q., A review of electrocatalytic reduction of dinitrogen to ammonia under ambient conditions. *Advanced Energy Materials* **2018,** *8* (22), 1800369.

[24] Van der Ham, C. J.; Koper, M. T.; Hetterscheid, D. G., Challenges in reduction of dinitrogen by proton and electron transfer. *Chemical Society Reviews* **2014,** *43* (15), 5183-5191.

[25] Bao, D.; Zhang, Q.; Meng, F. L.; Zhong, H. X.; Shi, M. M.; Zhang, Y.; Yan, J. M.; Jiang, Q.; Zhang, X. B., Electrochemical reduction of N2 under ambient conditions for artificial N_2 fixation and renewable energy storage using N_2/NH_3 cycle. *Advanced materials* **2017,** *29* (3), 1604799.

[26] Shi, M. M.; Bao, D.; Wulan, B. R.; Li, Y. H.; Zhang, Y. F.; Yan, J. M.; Jiang, Q., Au sub‐nanoclusters on TiO_2 toward highly efficient and selective electrocatalyst for N_2 conversion to NH_3 at ambient conditions. *Advanced Materials* **2017,** *29* (17), 1606550.

[27] Nazemi, M.; Panikkanvalappil, S. R.; El-Sayed, M. A., Enhancing the rate of electrochemical nitrogen reduction reaction for ammonia synthesis under ambient conditions using hollow gold nanocages. *Nano Energy* **2018,** *49*, 316-323.

[28] Tsuneto, A.; Kudo, A.; Sakata, T., Lithium-mediated electrochemical reduction of high pressure N_2 to NH_3. *Journal of Electroanalytical Chemistry* **1994,** *367* (1-2), 183-188.

[29] Kim, K.; Lee, N.; Yoo, C.-Y.; Kim, J.-N.; Yoon, H. C.; Han, J.-I., Communication—electrochemical reduction of nitrogen to ammonia in 2-propanol under ambient temperature and pressure. *Journal of The Electrochemical Society* **2016,** *163* (7), F610.

[30] Zhou, F.; Azofra, L. M.; Ali, M.; Kar, M.; Simonov, A. N.; McDonnell-Worth, C.; Sun, C.; Zhang, X.; MacFarlane, D. R., Electro-synthesis of ammonia from nitrogen at ambient temperature and pressure in ionic liquids. *Energy Environmental Science* **2017,** *10* (12), 2516-2520.

[31] Ohno, H., Molten salt type polymer electrolytes. *Electrochimica Acta* **2001,** *46* (10-11), 1407-1411.

[32] Licht, S.; Cui, B.; Wang, B.; Li, F.-F.; Lau, J.; Liu, S. J. S., Ammonia synthesis by N_2 and steam electrolysis in molten hydroxide suspensions of nanoscale Fe_2O_3. *Science* **2014,** *345* (6197), 637-640.

[33] Ishihara, T.; Matsuda, H.; Takita, Y., Doped $LaGaO_3$ perovskite type oxide as a new oxide ionic conductor. *Journal of the American chemical society* **1994,** *116* (9), 3801-3803.

[34] Yang, X.; Nash, J.; Anibal, J.; Dunwell, M.; Kattel, S.; Stavitski, E.; Attenkofer, K.; Chen, J. G.; Yan, Y.; Xu, B., Mechanistic insights into electrochemical nitrogen reduction reaction on vanadium nitride nanoparticles. *Journal of the American Chemical Society* **2018,** *140* (41), 13387-13391.

[35] Amar, I. A.; Lan, R.; Petit, C. T.; Tao, S., Solid-state electrochemical synthesis of ammonia: a review. *Journal of Solid State Electrochemistry* **2011,** *15* (9), 1845.

[36] Skulason, E.; Bligaard, T.; Gudmundsdóttir, S.; Studt, F.; Rossmeisl, J.; Abild-Pedersen, F.; Vegge, T.; Jonsson, H.; Nørskov, J. K., A theoretical evaluation of possible transition metal electro-catalysts for N_2 reduction. *Physical Chemistry Chemical Physics* **2012,** *14* (3), 1235-1245.

[37] Shi, Miao - Miao, et al. "Au Sub - Nanoclusters on TiO_2 toward Highly Efficient and Selective Electrocatalyst for N_2 Conversion to NH_3 at Ambient Conditions." Advanced Materials 29.17 (2017): 1606550.

[38] Wang, S.; Ichihara, F.; Pang, H.; Chen, H.; Ye, J., Nitrogen fixation reaction derived from nanostructured catalytic materials. *Advanced Functional Materials* **2018,** *28* (50), 1803309.

[39] Mukherjee, S.; Cullen, D. A.; Karakalos, S.; Liu, K.; Zhang, H.; Zhao, S.; Xu, H.; More, K. L.; Wang, G.; Wu, G., Metal-organic framework-derived nitrogen-doped highly disordered carbon for electrochemical ammonia synthesis using N_2 and H_2O in alkaline electrolytes. *Nano Energy* **2018,** *48*, 217-226.

[40] Li, Q.; He, L.; Sun, C.; Zhang, X., Computational study of MoN_2 monolayer as electrochemical catalysts for nitrogen reduction. *The Journal of Physical Chemistry C* **2017,** *121* (49), 27563-27568.

[41] Le, Y.-Q.; Gu, J.; Tian, W. Q., Nitrogen-fixation catalyst based on graphene: every part counts. *Chemical Communications* **2014,** *50* (87), 13319-13322.

[42] Zhu, D.; Zhang, L.; Ruther, R. E.; Hamers, R. J., Photo-illuminated diamond as a solid-state source of solvated electrons in water for nitrogen reduction. *Nature materials* **2013,** *12* (9), 836-841.

[43] Song, Y.; Johnson, D.; Peng, R.; Hensley, D. K.; Bonnesen, P. V.; Liang, L.; Huang, J.; Yang, F.; Zhang, F.; Qiao, R., A physical catalyst for the electrolysis of nitrogen to ammonia. *Science advances* **2018,** *4* (4), e1700336.

[44] Singh, A. R.; Rohr, B. A.; Schwalbe, J. A.; Cargnello, M.; Chan, K.; Jaramillo, T. F.; Chorkendorff, I.; Nørskov, J. K., Electrochemical Ammonia Synthesis-The Selectivity Challenge. ACS Publications: 2017.

[45] Xu, H.; Ithisuphalap, K.; Li, Y.; Mukherjee, S.; Lattimer, J.; Soloveichik, G.; Wu, G., Electrochemical ammonia synthesis through N_2 and H_2O under ambient conditions: Theory, practices, and challenges for catalysts and electrolytes. *Nano Energy* **2020,** *69*, 104469.

2 Materials in general

2.1 Metal–organic frameworks (MOFs) materials

2.1.1 MOFs: Overview

Metal-organic Frameworks (MOFs), also called porous coordination polymers (PCPs), are a class of materials constructed by connecting metal ions or clusters with organic linkers, which have captured widespread interest and achieved the explosive development over the past two decades [1]. MOFs consist of both inorganic and organic units. The organic units (linkers/bridging ligands) consist of carboxylates, or anions, such as phosphonate, sulfonate, and heterocyclic compounds. The inorganic units are the metal ions or clusters termed as secondary building units (SBUs) [2]. Their geometry is determined by the coordination number, coordination geometry of the metal ions, and the nature of the functional groups. The exhibiting open crystalline structure, structural flexibility, and tunable functionality as well as ultrahigh surface area make MOFs find their potential applications in diverse fields, such as gas sorption and separation[3], chemical sensing[4], proton conductivity[5], biomedicine [6]. In particular, catalysis is one of the earliest demonstrated applications [7] and is becoming one of the most promising applications for MOFs, along with its rapid development in the past 20 years [8].

The term [9] “metal-organic framework” was introduced by Prof. Omar Yaghi in 1995. A coordination compound with a two-dimensional structure was synthesized by utilizing 1, 3, 5-Benzenetricarboxylic acid (BTC) as a linker and cobalt ions as metal nodes. In 1999, Yaghi et al. designed and synthesized an exceptionally stable and highly porous metal-organic framework, MOF-5 (Zn_4O $(bdc)_3$, bdc = terephthalate), one of the most well-known MOF structures, shown in Figure 2.1. The metal nodes at the eight vertices of the cube are connected by stable organic molecules with benzene rings, each containing four zinc atoms, fixed by carbon and oxygen atoms. In MOF-5, 55±61% of the space is accessible to guest species and stable when fully desolvated and heated up to 300 ^{o}C.

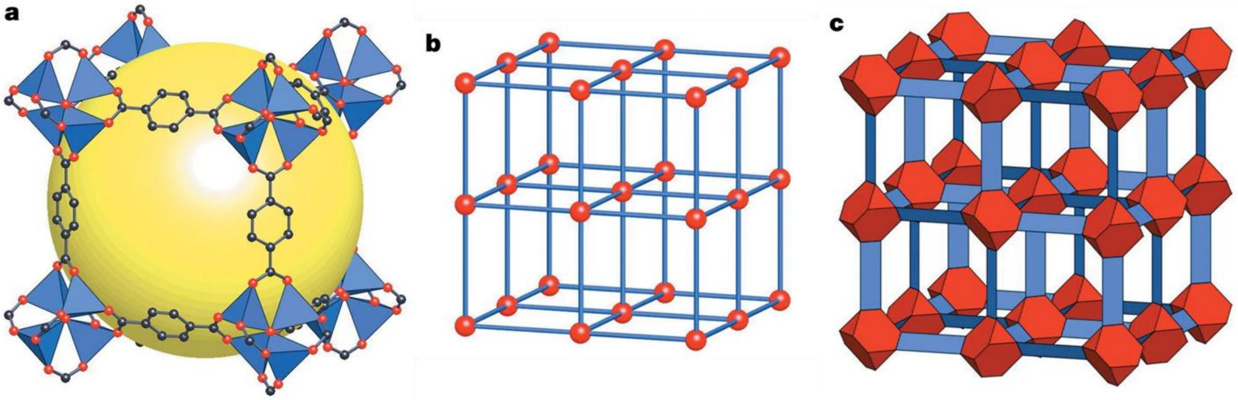

Figure 2.1 The MOF-5 structure and its topology. (a) The MOF-5 structure shown as ZnO_4 tetrahedra (blue polyhedra) joined by benzene dicarboxylate linkers (O, red and C, black) to give an extended 3D cubic framework with interconnected pores of 8A° aperture width and 12A° pore (yellow sphere) diameter. (b) The topology of the structure (primitive cubic net) shown as a balland- stick model. (c) The structure shown as the envelopes of the $(OZn_4)O_{12}$ cluster (red truncated tetrahedron) and benzene dicarboxylate (BDC) ion (blue slat).

In 2004 [10] and 2005 [11], Gérard Férey's group reported a new type of MOFs with very large pore size, MIL-100 and MIL-101, respectively. Especially for the MIL-101, Férey combined targeted chemistry and computational design to create a crystal structure for porous chromium terephthalate, with very large pore sizes and surface area by employing H_2BDC and building trinuclear chromium carboxylate secondary building units (SBUs). The pore cavity is available in 2.9 nm and 3.0 nm and a Langmuir surface area for N_2 of ∼5900 m^2/g.

In 2006, Yaghi's group turned their attention to conventional molecular sieve materials with superior stability properties and reported that 12 zeolitic imidazolate frameworks (ZIFs; termed ZIF-1 to -12) were synthesized as crystals by copolymerization of either Zn(II) or Co(II) with imidazolate-type links [12]. These materials exhibited superior thermal and chemical stability, ZIF-8 and -11, demonstrating their permanent porosity (Langmuir surface area = 1,810 m^2/g), high thermal stability (up to 550°C), and remarkable chemical resistance to boiling alkaline water and organic solvents.

UiO-66 is the prototype of UiO family with the material composition of $Zr_6O_4(OH)_4(BDC)_6$. UiO stands for the Oslo University and was first reported by Lillerud’s group in 2008 [13]. The archetypal UiO-66 has a very high surface area as well as high thermal stability. The high thermal stability could be attributed to the metal oxide node being cuboctahedral allowing for 12 extension points for 1, 4-benzenedicarboxylic acid (BDC) coordination. By increasing the number of benzene rings in the ligands, the length of the ligands increased, and UiO-67 and UiO-68 with larger pores (shown in Figure 2.2) were synthesized and applied in porous coordination polymer field.

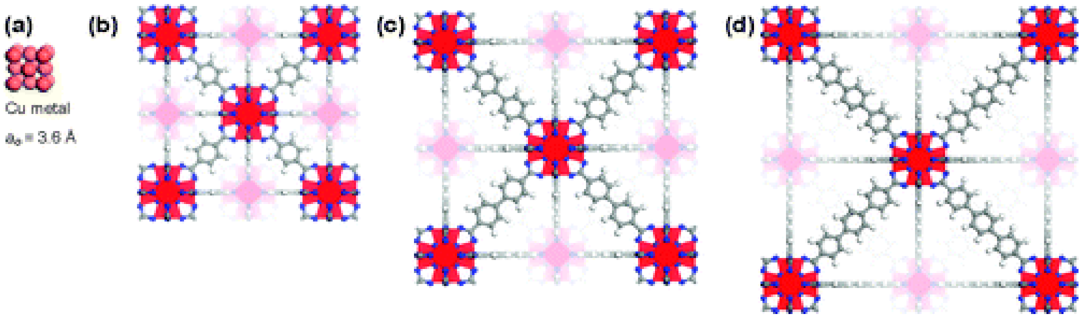

Figure 2.2 (a) One unit cell of copper drawn to scale with: (b) UiO-66, Zr-MOF with 1, 4-benzene-dicarboxylate (BDC) as linker (c) UiO-67, Zr-MOF with 4,4′ biphenyl-dicarboxylate (BPDC) as linker, (d) Zr-MOF with terphenyl dicarboxylate (TPDC) as linker, UiO-68. Zirconium, oxygen, carbon, and hydrogen atoms are red, blue, gray, and white, respectively.

2.1.2 MOFs: Nomenclature and composition

In recent times, numerous materials containing metal ions bound by organic linkers have been described. Abbreviation MOF is used as a general name of the class of these compounds. When followed by an ordinal number, it represents an individual metal-organic framework. Examples of typical MOF names and their composition were summarized in Table 2.1 [14].

Table 2.1 Examples of typical MOF names and their composition.

No.	Designation	Formula	Abbreviation interpretation
1	MOF-74	$\mathrm{Zn_2DOT}$	Metal-Organic Frameworks
2	MOF-101	$\mathrm{Cu_2(BDC\text{-}Br)_2(H2O)_2}$	
3	MOF-177	$\mathrm{Zn_4O(BTB)_2}$	
4	MOF-235	$\mathrm{[Fe_3O(BDC)_3(DMF)_3][FeCl_4] \cdot (DMF)_3}$	
5	MOF-253	$\mathrm{Al(OH)(BPYDC)}$	

6	IRMOF-1 (MOF-5)	$Zn_4O(BDC)_3 \cdot 7DEF \cdot 3H_2O$	IsoReticular Metal-Organic Frameworks
7	IRMOF-16	$Zn_4O(TPDC)_3 \cdot 17\ DEF \cdot 2H_2O$	
8	UiO-66	$Zr_6O_6(BDC)_6$	Universitetet i Oslo
9	UiO-67	$Zr_6O_6(BPDC)_6$	
10	UiO-68	$Zr_6O_6(TPDC)_6$	
11	MIL-53	$Al(OH)(BDC)$	Materials of Institut Lavoisier
12	MIL-53(Al)-NH_2	$Al(OH)(BDC\text{-}NH_2)$	
13	MIL-88A	$Fe_3O(MeOH)_3(O_2CCH{=}CHCO_2)_3 \cdot MeCO_2 \cdot n\ H_2O$	
14	MIL-88-Fe	$Fe_3O(MeOH)_3(O_2C(CH_2)_2CO_2)_3 \cdot AcO \cdot (MeOH)_{4.5}$	
15	MIL-88B-4CH_3	$2Fe_3O(OH)(H_2O)_2(BDC\text{-}Me_2)_3$	
16	MIL-100-Fe	$Fe^{III}{}_3\ O(H_2O)_2F \cdot (BTC)_2 \cdot n\ H_2O$	
17	MIL-101	$Cr_3O(H_2O)_2F \cdot (BDC)_3 \cdot n\ H_2O$	
18	HKUST-1 (MOF-199)	$Cu_3(BTC)_2$	Hong Kong University of Science and Technology
19	LIC-1	$Gd_2(BDC\text{-}NH_2)_3(DMF)_4$	Leiden Institute of Chemistry
20	ZIF-8	$Zn(MIM)_2$	Zeolite Imidazolate Framework
21	ZIF-90	$Zn(FIM)_2$	
22	CPL-2	$Cu_2(PZDC)_2(4,40\ \text{-}BPY)$	Coordination Polymer with pillared Layer structure
23	F-MOF-1	$[Cu(HFBBA)(phen)_2](H_2HFBBA)_2(H_2O)(HCO_2)$	Fluorinated Metal-Organic Framework
24	MOP-1	$Cu_{24}(m\text{-}BDC)_{24}(DMF)_{14}(H_2O)_{10}$	Metal-Organic Polyhedra

Note. DOT is 2,5-dihydroxyterephthalate, BPYDC is 2,20 -bipyridine-5,50 -dicarboxylate, DEF is N,N-diethylformamide, TPDC is p-terphenyl4,40 -dicarboxylate, BPDC is biphenyl-4,40 -dicarboxylate, MIM is 2-methylimidazolate, FIM is 2-formylimidazolate, PZDC is pyrazine-2,3- dicarboxylate, 4,40 -BPY is 4,40 -bipyridine, phen is 1,10-phenanthroline, HFBBA is 4,40 -(hexafluoroisopropylidene)dibenzoate, m-BDC is m-benzenedicarboxylate (for BDC, BDC-Br, BDC-NH2, BDC-Me2, BTB, BTC, see Fig. 2.3).

Two components can be distinguished in MOFs: secondary building units (Figure 2.3a) (clusters or metal ions) and organic molecules (Figure 2.3b) linking the former to give basically periodic porous structures [1]. Different combinations of these structure elements lead to an enormous number of MOFs.

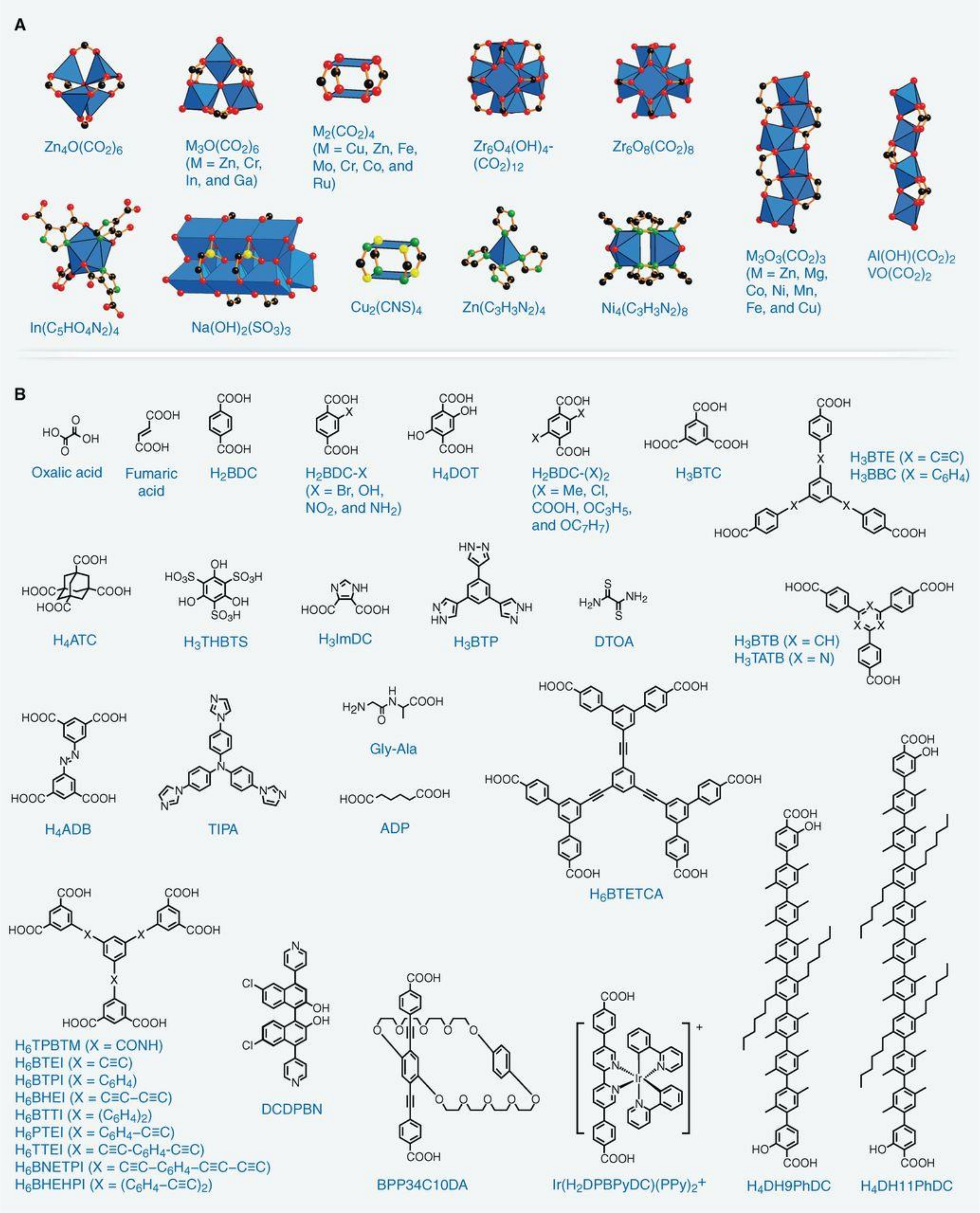
A
Zn4O(CO2)6
M3O(CO2)6 (M = Zn, Cr, In, and Ga)
M2(CO2)4 (M = Cu, Zn, Fe, Mo, Cr, Co, and Ru)
Zr6O4(OH)4-(CO2)12
Zr6O8(CO2)8
M3O3(CO2)3 (M = Zn, Mg, Co, Ni, Mn, Fe, and Cu)
Al(OH)(CO2)2
VO(CO2)2
In(C5HO4N2)4
Na(OH)2(SO3)3
Cu2(CNS)4
Zn(C3H3N2)4
Ni4(C3H3N2)8
B
Oxalic acid
Fumaric acid
H2BDC
H2BDC-X (X = Br, OH, NO2, and NH2)
H4DOT
H2BDC-(X)2 (X = Me, Cl, COOH, OC3H5, and OC7H7)
H3BTC
H3BTE (X = C≡C)
H3BBC (X = C6H4)
H4ATC
H3THBTS
H3ImDC
H3BTP
DTOA
H3BTB (X = CH)
H3TATB (X = N)
H4ADB
TIPA
Gly-Ala
ADP
H6BTETCA
H6TPBTM (X = CONH)
H6BTEI (X = C≡C)
H6BTPI (X = C6H4)
H6BHEI (X = C≡C–C≡C)
H6BTTI (X = (C6H4)2)
H6PTEI (X = C6H4–C≡C)
H6TTEI (X = C≡C-C6H4-C≡C)
H6BNETPI (X = C≡C–C6H4–C≡C–C≡C)
H6BHEHPI (X = (C6H4–C≡C)2)
DCDPBN
BPP34C10DA
Ir(H2DPBPyDC)(PPy)2+
H4DH9PhDC
H4DH11PhDC

Figure 2.3 Constituents of metal-organic frameworks. (a) Metal clusters (the polyhedra demonstrate the metal coordination); (b) organic molecules from which linkers are formed. *Copyright 2013,* American Association for the Advancement of Science

2.1.3 MOFs: Catalytic Applications

Metal-organic frameworks (MOFs), as a new stable class of hybrid materials synthesized, regulated and decorated by rational incorporating organic bridging ligands and metal ions with well-defined coordination geometry, have become promising candidates for heterogeneous catalysis in industrial applications.

In the field of heterogeneous catalysis, MOFs have been investigated extensively [15]. In view of structure, MOFs are similar to homogeneous catalysts, which is alternatively regarded as an isolated unit in the infinite network of MOFs. Moreover, the periodic structure enables MOFs to disperse active sites uniformly throughout the framework; the porosity promotes the accessibility of active sites and the transport of catalytic reactants or products in MOFs. Therefore, MOFs might behave like metal complex catalysts and possess the advantages of homogeneous catalysis. On the other hand, being porous solid materials, MOFs are well recyclable after reaction as a character of heterogeneous catalysts. Hence, MOFs have the particular advantages of both "homogeneous catalyst—full usage of active sites and high reactivity" and "heterogeneous catalyst—recyclability."

The catalytic activity of MOFs either originates from uncoordinated metal centers or functional groups attached to the linkers of the framework [16]. The pore space of MOFs is able to accommodate a variety of additional active species (e.g., organic molecules, inorganic nanoparticles, metal complexes, enzymes) as guests and behaves as a nanoreactor to host catalytic reactions (Figure 2.4) [17]. An important factor is that the compounds are located inside the MOF cavities rather than on the outer surface of the MOF. Various methods are available for the incorporation of guest compounds in the MOF. For example, the MOF UiO-bpy was synthesized followed by post-functionalization with Cu^{2+} ions, which coordinated to the bpy sites and Zn^{2+} ions to react with them μ_3-OH sites on the secondary building units. The formation in situ of the active catalyst species, i.e. Cu/ZnO_x@MOF, with confined ultrasmall metal nanoparticles inside the cavities of the MOF, resulted in high selectivity and catalytic activity for the hydrogenation of CO_2 into MeOH [18]

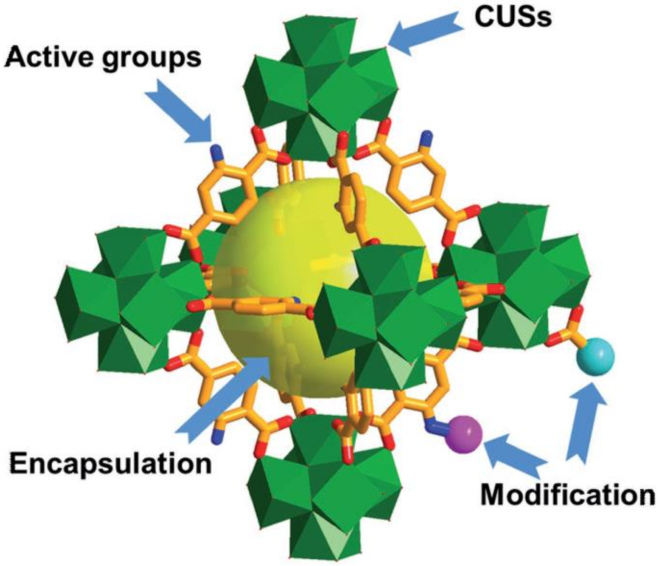

Figure 2.4 Different strategies to the incorporation of active species inside a MOF [17] . Copyright 2018 Wiley Online Library.

Some pristine MOFs have poor stability and low electronic conductivity, which limit their application to a certain degree [19]. Porous carbon materials have high specific surface area, high porosity, adjustable pore size, high electronic conductivity and good chemical stability in acid/alkaline conditions. At the same time, MOFs have regular structure, uniform composition, and high carbon content, which are considered as promising sacrificial templates and metal precursors for the synthesis of carbon materials [20].Compared with traditional methods of synthesizing carbon-based materials, MOF-derived carbons have outstanding advantages in the preparation process. The inherent diversity of MOFs provides the basis for precise control of the physical and chemical properties of materials. The changes in organic ligands, functional monomers and carbonization conditions create more possibilities for doping heteroatoms and improving performance, greatly expanding the types of materials. MOF-derived carbons include carbon skeletons encapsulating metal or metal oxide nanoparticles, nonmetal doped carbon hybrid materials, metal-free porous carbons and other composites. These carbons derived from MOFs have the advantages of porous carbons, which improve the stability and poor conductivity of the pristine MOFs. As shown in Figure 2.5, the MOFs can be combined with other nanostructures such as graphene and nanotubes in order to improve conductivity, and they can be calcinated to provide hybrid catalytically efficient metal−carbon and -heteroatom nanocomposites [21].

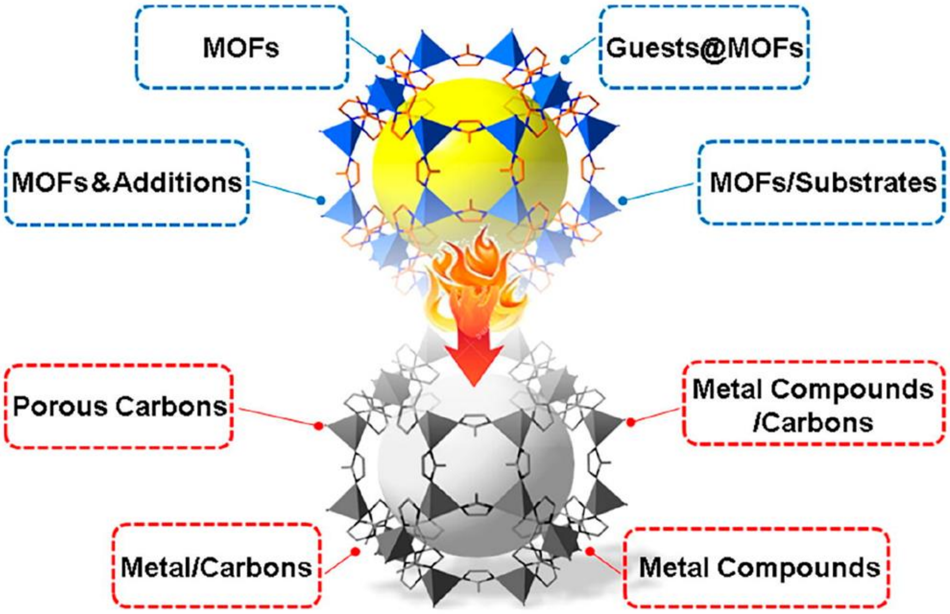

Figure 2.5 Fabrication of Numerous Porous Materials from MOFs and MOF-Based Composites through Pyrolysis [21]. Copyright 2018 Elsevier.

Many studies have shown that MOF-derived carbons have broad development prospects in the field of catalysis. Since the use of MOFs as precursors/templates for synthesis of porous carbons was first reported in 2008[22], the pyrolysis of MOFs has been widely adopted as an effective way to obtain carbon-based materials with various morphologies and compositions. Especially in the field of electrochemistry, the MOF-derived carbon materials can be used as catalysts or catalyst supports to promote oxygen reduction reaction (ORR) [23], oxygen evolution reaction (OER) [23], hydrogen evolution reaction (HER) [24], and nitrogen reduction reaction (NRR) [25] showing excellent performance in catalysis and energy conversion.

In this thesis, a series of Fe based MOF were synthesized and applied in nitrogen reduction reaction. Detailed background of MOFs materials applied in NRR were discussed in the next chapters.

2.2 MXenes

2.2.1 MXenes: Structure and properties

Since graphene was first prepared by mechanical exfoliation in 2004 [26], two-dimensional (2D) materials have drawn great attention on account of their unique physical and chemical properties [27]. In 2011, Naguib et al [28]. first prepared transition metal nitride/carbon nano-layered materials (MXenes), a new type of 2D layer material.

MXenes have a general formula of $M_{n+1}X_nT_x$ where n = 1−4, M = early transition metal such as Ti, V, and Mo, X = C or N or both, and T_x = surface termination groups such as −O, −OH, −F, and −Cl, which are formed on the outer M basal plane during the synthesis process. MXenes have representative structures of M_2XT_x, $M_3X_2T_x$, and $M_4X_3T_x$ with n layers of X elements covered by n+1 layers of M, shown in Figure 2.6 [29].

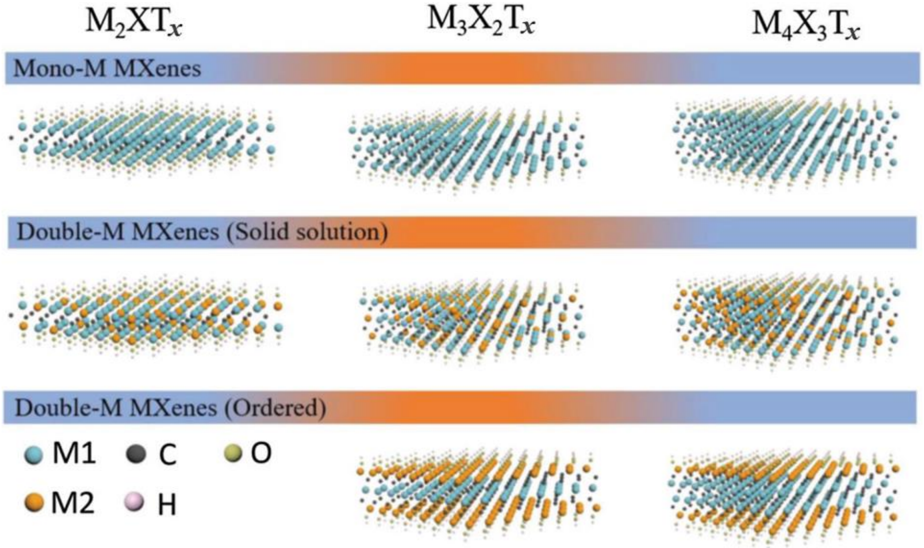

Figure 2.6 The structures of MXenes with different formulas (M_2XT_x, $M_3X_2T_x$, and $M_4X_3T_x$) and compositions (mono-M MXenes and double-M MXenes) [29].Copyright 2019, Wiley-VCH.

MXenes are usually obtained by selective etching of specific atomic layers from their layered precursors, such as MAX phases. “A” means group 13 or 14 elements such as Al, Si, and Ga. The A-group atom layers are preferentially etched away as the M−A bonds binding the MXene layers together in the MAX structure are chemically more active than the stronger M−X bonds within the MXene sheets [31]. Because the synthesis of MXenes related to etching with strong acids such as hydrofluoric acid, their surface are generally grafted with various terminal functional groups such as OH, O, and F. The surface termination exerts significant impacts on the properties of MXenes. Hu et al [32]. reported that the chemical origin of termination-functionalized MXenes by Bader charge analysis and thermodynamic calculations; the materials revealed stability in the order of $Ti_3C_2O_2$> $Ti_3C_2F_2$ > $Ti_3C_2(OH)_2$ > $Ti_3C_2H_2$ > Ti_3C_2, which was attributed to the splitting of the highly degenerated 3*d* orbitals of surface Ti. Hope et al [33]. quantified the surface functional groups of $Ti_3C_2T_x$ by 1H and 19F nuclear magnetic resonance (NMR) experiments and found that the proportions of different surface terminations highly rely on the preparation method of the material. Many researches showed that the surface chemistry of MXenes can be controlled to some extent by the selective etching conditions or through postetch processing to optimize binding toward specific electroactive species for efficient catalysis [34].

2.2.2 MXenes: Applications for electrocatalysis

MXenes have a unique 2D layered structure similar to graphene, with a large specific surface area, good hydrophilicity, conductivity, and stability. Research shows that they have broad prospects in terms of electrochemical energy storage [35], catalysis [29], photothermal conversion [36], water purification [37], gas separation [38], biomedical applications [39], and electromagnetic interference shielding [40]. Among them, it is in the field of catalysis that MXenes have currently received much attention.

Electrocatalysis is a promising approach for future clean energy conversion technologies, including hydrogen evolution reaction (HER), oxygen evolution reaction (OER), oxygen reduction reaction (ORR), nitrogen reduction reaction (NRR) and carbon dioxide reduction reaction (CORR). A summary of representative MXene-based materials for applications in electrocatalysis is shown in Table 2.2.

Table 2.2 Summary of representative MXene-based materials for applications in catalysis.

Catalytic reactions	Representative catalysts	Performance and activity origin
HER	$MoS_2/Ti_3C_2@C$[41]	Overpotential of 135 mV @ 10 mA cm^{-2} in acid solution. The 2D structure and surface terminations of Ti_3C_2 facilitate the coupling of few-layered Mo_2S nanoplates that provide edge active sites for HER.
	Mo_2CT_x[42]	Mo_2CT_x delivers 10 mA cm^{-2} at an overpotential of 283 mV in 0.5 M H_2SO_4. Mo_2CT_x in delaminated form shows improved HER activity, together with the theoretical calculations indicating that the basal planes of Mo_2CT_x are catalytically active.
OER	Co-P/3D Ti_3C_2 MXene[43]	Overpotential of 298 mV @ 10 mA cm^{-2} with a Tafel slope of 51 mV dec^{-1} for CoP/3D Ti_3C_2 MXene in alkaline electrolyte. CoP converts to high valence cobalt compounds as active sites.
	$Ni_{0.7}Fe_{0.3}PS_3@Ti_3C_2T_x$[44]	The catalysts exhibits an overpotential of 282 mV @ 10 mA cm^{-2} with a Tafel slope of 36.5 mV dec^{-1} in 1 M KOH. Fe cations lead to ionic metal center that improves the carrier concentration and electrical conductivity.
ORR	Iron phthalocyanine (FePc)/$Ti_3C_2T_x$[45]	Twofold and fivefold enhancement of ORR activity was achieved compared to pristine FePc and Pt/C, respectively. FeN_4 moiety on MXene induces redistribution of the local electron density, which modified the O_2 adsorption and reduction.

	$Ti_3C_2T_x$-$Ag_{0.9}Ti_{0.1}$ NWs	MXene/NW-$Ag_{0.9}Ti_{0.1}$ shows the best ORR activity with an initial potential of 0.564 V versus RHE. The bimetallic NWs offer more sites for adsorbed oxygen and boost the conductivity in ORR reaction.
NRR	$Ti_3C_2T_x$	A maximum faradic efficiency of 4.62% and a NH_3 yield rate of 4.72 μg h^{-1} cm^{-2} was achieved on $Ti_3C_2T_x$/SSM. The middle Ti at the edge sites are considered as the active sites for NRR.
Photocatalysts for CO_2 reduction	TiO_2/Ti_3C_2	0.22 μmol h^{-1} for CH_4 production, 3.7 times higher than that of commercial TiO_2. Ti_3C_2 MXene suppresses the electron–hole recombination and the rice curst–like morphology increases the density of active sites.
	Ti_3C_2/Bi_2WO_6	The conversion of CO_2 (to CH_4 and CH_3OH) of the 2 wt% Ti_3C_2/Bi_2WO_6 nanosheets is 4 times higher than that of the pristine Bi_2WO_6. The 2D/2D heterojunction increases the specific area and facilitates the charge separation.

In this thesis, a series of MXenes were synthesized and applied in nitrogen reduction reaction. Detailed background of MXenes materials applied in NRR were discussed in chapter 5.

2.3 References

[1] Furukawa, H.; Cordova, K. E.; O’Keeffe, M.; Yaghi, O. M., The chemistry and applications of metal-organic frameworks. *Science* **2013,** *341* (6149).

[2] Yaghi, O. M.; O'Keeffe, M.; Ockwig, N. W.; Chae, H. K.; Eddaoudi, M.; Kim, J., Reticular synthesis and the design of new materials. *Nature* **2003,** *423* (6941), 705-714.

[3] Li, J.-R.; Kuppler, R. J.; Zhou, H.-C., Selective gas adsorption and separation in metal-organic frameworks. *Chemical Society Reviews* **2009,** *38* (5), 1477-1504.

[4] Kreno, L. E.; Leong, K.; Farha, O. K.; Allendorf, M.; Van Duyne, R. P.; Hupp, J. T., Metal-organic framework materials as chemical sensors. *Chemical reviews* **2012,** *112* (2), 1105-1125.

[5] Yamada, T.; Otsubo, K.; Makiura, R.; Kitagawa, H., Designer coordination polymers: dimensional crossover architectures and proton conduction. *Chemical Society Reviews* **2013,** *42* (16), 6655-6669.

[6] Lazaro, I. A.; Forgan, R. S., Application of zirconium MOFs in drug delivery and biomedicine. *Coordination Chemistry Reviews* **2019,** *380*, 230-259.

[7] Farrusseng, D.; Aguado, S.; Pinel, C., Metal-organic frameworks: opportunities for catalysis. *Angewandte Chemie International Edition* **2009,** *48* (41), 7502-7513.

[8] Dhakshinamoorthy, A.; Asiri, A. M.; Garcia, H., 2D Metal-Organic Frameworks as multifunctional materials in heterogeneous catalysis and electro/photocatalysis. *Advanced Materials* **2019,** *31* (41), 1900617.

[9] Yaghi, O. M.; Li, G.; Li, H., Selective binding and removal of guests in a microporous metal-organic framework. *Nature* **1995,** *378* (6558), 703-706.

[10] Férey, G.; Serre, C.; Mellot-Draznieks, C.; Millange, F.; Surblé, S.; Dutour, J.; Margiolaki, I., A hybrid solid with giant pores prepared by a combination of targeted chemistry, simulation, and powder diffraction. *Angewandte Chemie* **2004,** *116* (46), 6456-6461.

[11] Férey, G.; Mellot-Draznieks, C.; Serre, C.; Millange, F.; Dutour, J.; Surblé, S.; Margiolaki, I., A chromium terephthalate-based solid with unusually large pore volumes and surface area. *Science* **2005,** *309* (5743), 2040-2042.

[12] Park, K. S.; Ni, Z.; Côté, A. P.; Choi, J. Y.; Huang, R.; Uribe-Romo, F. J.; Chae, H. K.; O'Keeffe, M.; Yaghi, O. M., Exceptional chemical and thermal stability of zeolitic imidazolate frameworks. *Proceedings of the National Academy of Sciences* **2006,** *103* (27), 10186-10191.

[13] Cavka, J. H.; Jakobsen, S.; Olsbye, U.; Guillou, N.; Lamberti, C.; Bordiga, S.; Lillerud, K. P., A new zirconium inorganic building brick forming metal organic frameworks with exceptional stability. *Journal of the American Chemical Society* **2008,** *130* (42), 13850-13851.

[14] Butova, V. V. e.; Soldatov, M. A.; Guda, A. A.; Lomachenko, K. A.; Lamberti, C., Metal-organic frameworks: structure, properties, methods of synthesis and characterization. *Russian Chemical Reviews* **2016,** *85* (3), 280.

[15] García-García, P.; Müller, M.; Corma, A., MOF catalysis in relation to their homogeneous counterparts and conventional solid catalysts. *Chemical Science* **2014,** *5* (8), 2979-3007.

[16] Hu, M.-L.; Safarifard, V.; Doustkhah, E.; Rostamnia, S.; Morsali, A.; Nouruzi, N.; Beheshti, S.; Akhbari, K., Taking organic reactions over metal-organic frameworks as heterogeneous catalysis. *Microporous Mesoporous Materials* **2018,** *256*, 111-127.

[17] Jiao, L.; Wang, Y.; Jiang, H. L.; Xu, Q., Metal–organic frameworks as platforms for catalytic applications. *Advanced Materials* **2018,** *30* (37), 1703663.

[18] An, B.; Zhang, J.; Cheng, K.; Ji, P.; Wang, C.; Lin, W., Confinement of Ultrasmall Cu/ZnO_x Nanoparticles in Metal-Organic Frameworks for Selective Methanol Synthesis from Catalytic Hydrogenation of CO_2. *Journal of the American Chemical Society* **2017,** *139* (10), 3834-3840.

[19] Chen, S.; Huang, R.; Zou, J.; Liao, D.; Yu, J.; Jiang, X., A sensitive sensor based on MOFs derived nanoporous carbons for electrochemical detection of 4-aminophenol. *Ecotoxicology Environmental Safety* **2020,** *191*, 110194.

[20] Yang, S. J.; Kim, T.; Im, J. H.; Kim, Y. S.; Lee, K.; Jung, H.; Park, C. R., MOF-derived hierarchically porous carbon with exceptional porosity and hydrogen storage capacity. *Chemistry of Materials* **2012,** *24* (3), 464-470.

[21] Chen, Y.-Z.; Zhang, R.; Jiao, L.; Jiang, H.-L., Metal-organic framework-derived porous materials for catalysis. *Coordination Chemistry Reviews* **2018,** *362*, 1-23.

[22] Liu, B.; Shioyama, H.; Akita, T.; Xu, Q., Metal-organic framework as a template for porous carbon synthesis. *Journal of the American Chemical Society* **2008,** *130* (16), 5390-5391.

[23] Li, J.-S.; Li, S.-L.; Tang, Y.-J.; Han, M.; Dai, Z.-H.; Bao, J.-C.; Lan, Y.-Q., Nitrogen-doped Fe/Fe_3C@ graphitic layer/carbon nanotube hybrids derived from MOFs: efficient bifunctional electrocatalysts for ORR and OER. *Chemical Communications* **2015,** *51* (13), 2710-2713.

[24] Zhou, W.; Lu, J.; Zhou, K.; Yang, L.; Ke, Y.; Tang, Z.; Chen, S., $CoSe_2$ nanoparticles embedded defective carbon nanotubes derived from MOFs as efficient electrocatalyst for hydrogen evolution reaction. *Nano Energy* **2016,** *28*, 143-150.

[25] Tao, H.; Choi, C.; Ding, L.-X.; Jiang, Z.; Han, Z.; Jia, M.; Fan, Q.; Gao, Y.; Wang, H.; Robertson, A. W., Nitrogen fixation by Ru single-atom electrocatalytic reduction. *Chem* **2019,** *5* (1), 204-214.

[26] Novoselov, K. S.; Geim, A. K.; Morozov, S. V.; Jiang, D.; Zhang, Y.; Dubonos, S. V.; Grigorieva, I. V.; Firsov, A. A., Electric field effect in atomically thin carbon films. *Science* **2004,** *306* (5696), 666-669.

[27] Bonaccorso, F.; Colombo, L.; Yu, G.; Stoller, M.; Tozzini, V.; Ferrari, A. C.; Ruoff, R. S.; Pellegrini, V., Graphene, related two-dimensional crystals, and hybrid systems for energy conversion and storage. *Science* **2015,** *347* (6217).

[28] Naguib, M.; Kurtoglu, M.; Presser, V.; Lu, J.; Niu, J.; Heon, M.; Hultman, L.; Gogotsi, Y.; Barsoum, M. W., Two-dimensional nanocrystals produced by exfoliation of Ti_3AlC_2. *Advanced materials* **2011,** *23* (37), 4248-4253.

[29] Li, Z.; Wu, Y., 2D early transition metal carbides (MXenes) for catalysis. *Small* **2019,** *15* (29), 1804736.

[30] Naguib, M.; Mashtalir, O.; Carle, J.; Presser, V.; Lu, J.; Hultman, L.; Gogotsi, Y.; Barsoum, M. W., Two-dimensional transition metal carbides. *ACS nano* **2012,** *6* (2), 1322-1331.

[31] Naguib, M.; Gogotsi, Y., Synthesis of two-dimensional materials by selective extraction. *Accounts of chemical research* **2015,** *48* (1), 128-135.

[32] Hu, T.; Li, Z.; Hu, M.; Wang, J.; Hu, Q.; Li, Q.; Wang, X., Chemical Origin of Termination-Functionalized MXenes: $Ti_3C_2T_2$ as a Case Study. *The Journal of Physical Chemistry C* **2017,** *121* (35), 19254-19261.

[33] Hope, M. A.; Forse, A. C.; Griffith, K. J.; Lukatskaya, M. R.; Ghidiu, M.; Gogotsi, Y.; Grey, C. P., NMR reveals the surface functionalisation of Ti_3C_2 MXene. *Physical Chemistry Chemical Physics* **2016,** *18* (7), 5099-5102.

[34] Handoko, A. D.; Fredrickson, K. D.; Anasori, B.; Convey, K. W.; Johnson, L. R.; Gogotsi, Y.; Vojvodic, A.; Seh, Z. W., Tuning the basal plane functionalization of two-dimensional metal carbides (MXenes) to control hydrogen evolution activity. *ACS Applied Energy Materials* **2017,** *1* (1), 173-180.

[35] Zhang, X.; Zhang, Z.; Zhou, Z. J. J. o. e. c., MXene-based materials for electrochemical energy storage. *Journal of energy chemistry* **2018,** *27* (1), 73-85.

[36] Lin, H.; Wang, X.; Yu, L.; Chen, Y.; Shi, J., Two-dimensional ultrathin MXene ceramic nanosheets for photothermal conversion. *Nano letters* **2017,** *17* (1), 384-391.

[37] Xie, X.; Chen, C.; Zhang, N.; Tang, Z.-R.; Jiang, J.; Xu, Y.-J., Microstructure and surface control of MXene films for water purification. *Nature Sustainability* **2019,** *2* (9), 856-862.

[38] Ding, L.; Wei, Y.; Li, L.; Zhang, T.; Wang, H.; Xue, J.; Ding, L.-X.; Wang, S.; Caro, J.; Gogotsi, Y., MXene molecular sieving membranes for highly efficient gas separation. *Nature communications* **2018,** *9* (1), 1-7.

[39] Soleymaniha, M.; Shahbazi, M. A.; Rafieerad, A. R.; Maleki, A.; Amiri, A., Promoting role of MXene nanosheets in biomedical sciences: Therapeutic and biosensing innovations. *Advanced healthcare materials* **2019,** *8* (1), 1801137.

[40] Liu, J.; Zhang, H. B.; Sun, R.; Liu, Y.; Liu, Z.; Zhou, A.; Yu, Z. Z., Hydrophobic, flexible, and lightweight MXene foams for high-performance electromagnetic-interference shielding. *Advanced Materials* **2017,** *29* (38), 1702367.

[41] Wu, X.; Wang, Z.; Yu, M.; Xiu, L.; Qiu, J., Stabilizing the MXenes by carbon nanoplating for developing hierarchical nanohybrids with efficient lithium storage and hydrogen evolution capability. *Advanced Materials* **2017,** *29* (24), 1607017.

[42] Seh, Z. W.; Fredrickson, K. D.; Anasori, B.; Kibsgaard, J.; Strickler, A. L.; Lukatskaya, M. R.; Gogotsi, Y.; Jaramillo, T. F.; Vojvodic, A., Two-dimensional molybdenum carbide (MXene) as an efficient electrocatalyst for hydrogen evolution. *ACS Energy Letters* **2016,** *1* (3), 589-594.

[43] Xiu, L.; Wang, Z.; Yu, M.; Wu, X.; Qiu, J., Aggregation-resistant 3D MXene-based architecture as efficient bifunctional electrocatalyst for overall water splitting. *ACS nano* **2018,** *12* (8), 8017-8028.

[44] Du, C. F.; Dinh, K. N.; Liang, Q.; Zheng, Y.; Luo, Y.; Zhang, J.; Yan, Q., Self-assemble and in situ formation of Ni_1− xFe_xPS_3 nanomosaic-decorated MXene hybrids for overall water splitting. *Advanced Energy Materials* **2018,** *8* (26), 1801127.

[45] Li, Z.; Zhuang, Z.; Lv, F.; Zhu, H.; Zhou, L.; Luo, M.; Zhu, J.; Lang, Z.; Feng, S.; Chen, W., The marriage of the FeN_4 moiety and MXene boosts oxygen reduction catalysis: Fe 3d electron delocalization matters. *Advanced materials* **2018,** *30* (43), 1803220.

[46] Zhang, Z.; Li, H.; Zou, G.; Fernandez, C.; Liu, B.; Zhang, Q.; Hu, J.; Peng, Q., Self-reduction synthesis of new MXene/Ag composites with unexpected electrocatalytic activity. *ACS Sustainable Chemistry* **2016,** *4* (12), 6763-6771.

[47] Luo, Y.; Chen, G.-F.; Ding, L.; Chen, X.; Ding, L.-X.; Wang, H., Efficient electrocatalytic N_2 fixation with MXene under ambient conditions. *Joule* **2019,** *3* (1), 279-289.

[48] Low, J.; Zhang, L.; Tong, T.; Shen, B.; Yu, J., TiO_2/MXene Ti_3C_2 composite with excellent photocatalytic CO_2 reduction activity. *Journal of Catalysis* **2018,** *361*, 255-266.

[49] Cao, S.; Shen, B.; Tong, T.; Fu, J.; Yu, J., 2D/2D heterojunction of ultrathin MXene/Bi_2WO_6 nanosheets for improved photocatalytic CO_2 reduction. *Advanced Functional Materials* **2018,** *28* (21), 1800136.

3 Nitrogen Reduction Reaction: Experimental Methods and Identification and Elimination of Contamination

3.1 Introduction

Ammonia is produced on a large-scale via the Haber–Bosch process, which was developed more than 100 years ago and is still operating at high temperatures and pressures. It is a massively energy-consuming process that uses fossil fuels as the hydrogen source and accounts for ∼1% of annual global greenhouse gas emission [1]. Developing alternative and sustainable approaches for ammonia synthesis under ambient conditions is highly desirable.

Nitrogen Reduction Reaction (NRR) is promising for achieving clean and sustainable NH_3 production with lower energy consumption using renewable energy sources. A specific challenge is related to the development of novel electrocatalysts and reaction systems with the aim of improving two aspects related to NRR performance: (i) the ammonia formation selectivity (expressed in terms of Faradaic efficiency, FE), and (ii) the yield rate. The kinetics and thermodynamics of the NRR system depend on many factors, such as electrode potential, solvent effect, surface coverage, and pH values of electrolytes [2]. Therefore, it is essential not only to investigate the advancement of the catalysts but also to examine both catalysts and electrolyte as a whole.

A promising class of materials to be used as electrocatalysts are metal-organic frameworks (MOFs). They are a class of porous materials assembled with metal ion centers/clusters and organic ligands. The chemistry of MOFs has provided an extensive class of crystalline materials with high stability, tunable properties, organic functionality, and porosity. [3] In particular, the functional groups and the metal ion centers in MOFs can be directly designed to create the catalytic active sites for a specific reaction. For electrocatalysis, apart from inherently high surface area, MOFs provide opportunity to tailor single atomic active metal centers, which can reduce the mass consumption and increase the electrode/electrolyte interface. [4] Moreover, the MOF structures can be modified in a number of ways to obtain electrochemically active species. For example, by pyrolysis of MOFs under an inert atmosphere at a suitable temperature, the metal ions can be transformed to metal nanoparticles (NPs), metal oxide nanostructures, or both depending on the reduction potential of metal atoms present in the MOFs, [5] which are highly dispersed on or embedded in a ligand-derived carbon matrix. In comparison with other carbon-based catalysts, MOF-derived carbon-based nanomaterials have great advantages in terms of tailorable morphologies, hierarchical porosity and easy functionalization with other heteroatoms and metal/metal oxides, which make them highly efficient as catalysts directly or as catalyst supports for many important reactions.

MOF (Fe) was first reported as efficient NRR electrocatalyst at 90^{o}C by Chen’s group, [6] with the highest ammonia formation rate and the highest current efficiency reached 2.12×10^{-9} mol s^{-1} cm^{-2} and 1.43%, respectively. It directed a new route to develop highly efficient MOFs-based catalysts for the electrochemical synthesis of ammonia at low temperature and ambient pressure. To improve the yield and efficiency of NRR, there's plenty of scope to push that further with MOFs-based catalysts.

In this chapter, we presented a series of MOF materials to be processed in NRR. These electrocatalytic materials were synthesized at the laboratory CNRS-CPE in Lyon and then assembled with a gas diffusion layer and tested in NRR at the University of Messina. The results obtained by these electrocatalytic tests were very useful to improve the design of the MOFs-based electrodes, evidencing the limits of these kinds of materials in terms of N content, stability and possibility to prepare more advanced electrocatalysts by carbonization.

Moreover, part of the study presented in this chapter was spent in developing new experimental strategies to avoid false positive in the detection of ammonia, which is one of the topics most studied from scientists working in NRR in the last two years. As accurate protocols were recently suggested in literature by using advanced analytical techniques (i.e. using ^{15}N labelled nitrogen), [7] an easier methodology was used in this chapter to avoid ammonia contaminations and false positive, although we are aware that the more sophisticated analysis would be opportune but also not easily accessible in all the laboratories.

3.2 Ammonia contamination

In general, the amount of ammonia produced in NRR at room temperature and pressure is as low as the nanomole level. Meanwhile, ammonia is also ubiquitous in laboratory environments and it is a common contaminant in chemicals, especially in gases. Recently, the presence of nitrogen-containing species in NO_x^- or nitrides at substantial levels were revealed from many commercial catalysts, influencing the performances in NRR.[8] As a volatile gas, ammonia tends to accumulate over time on the surface of ordinary glassware or in aqueous solutions. Any negligent operation would result in the mis-leading data in NRR, sometimes with vastly overestimated FEs due to these exogenous contaminations. By further research on electrocatalytic ammonia synthesis in the past two years, some researchers begun to re-evaluate the reliability of their previous reports and identify any work that qualifies as “genuine NRR”. In 2014, Licht et al. reported a direct synthesis of ammonia method from N_2 and H_2O and steam electrolysis in molten hydroxide suspensions of nanoscale Fe_2O_3.[9] However, on 14th August 2020, after six years, this highly cited article published on science was retracted by the authors.[10] Their recently purchased nanoscale Fe_2O_3 per gram contained 0.0005 g N as NO_x^- and one of the author suggests that this trace impurity, rather than N_2, was the major nitrogen reactant in the observed ammonia synthesis. Without sufficient and rigorous control experiments, it would be unreliable to evaluate the NRR activity of electrocatalysts.

The contamination sources can be classified into two groups: out-system and intra-system.

3.2.1 The out-system ammonia contaminations

Ammonia is easily dissolved into aqueous solutions and adsorbed on a wide range of surfaces due to its polarity and a high aqueous solubility.[10] The ubiquitous ammonia usually leads to high background interferences. The out-system contamination mainly includes ammonia or NO_x present in the air, in the liquid and experimental consumables.

The pure water or tap water might contains a small amount of ammonia, while the possible presence of some ions or other interferents in the tap water induces the false negative. The use of ultrapure water is thus highly recommended for the preparation of the electrolyte, as well as in washing operations of the electrodes/device. Moreover, a blank test of the water used and of the fresh electrolyte is needed.

Ambient air is also demonstrated to possess a content of ammonia, even within the human breath. On account of this severe gaseous contamination, the use of an air-tight system is crucial to ensure no ambient air entering the cell during the electrocatalytic test.

Moreover, the gaseous ammonia is easily adsorbed and accumulated in the experimental setups and consumables, thus a thorough cleaning with ultrapure water should be strictly executed prior to the NRR experiments. Li et al.[12] observed an ultrahigh ammonia amount of ~0.21 μg mL^{-1} in the new nitrile gloves.

As in a chemical laboratory many experiments may be carried out at the same time, the operator should make sure that no other operators use ammonia as reactant without a proper venting system. Moreover, if electrocatalysts/electrodes and other parts of the electrochemical device need any kinds of treatment (e.g. heating in the oven), sharing of equipment/tools should be handled with care to avoid contaminations. Finally, long term exposure of catalysts, electrolytes, experimental setups, and consumables in an ammonia polluted environment may introduce errors in the reporting data.

3.2.2 The intra-system ammonia contaminations

The intra-system contamination, such as nitrogen-containing compounds in the feed gas, electrocatalysts, and membrane, is more indeterminate and cannot even be probed independently, thus usually resulting in a significant impact on the ammonia yield and unreliable results.

For example, proton-exchange membranes (such as the Nafion®115 membrane used in the experimental work of this thesis) has a high ammonia adsorption capacity. A careful washing and purification of the membranes is highly recommended, especially if the proton-exchange membrane is re-used in many testing experiments to avoid any disturbance arising from ammonia adsorption and desorption.

The oxidised forms of nitrogen (NO_x) have been identified as the source of many false positives in the biochemical N_2 fixation field.[13] Similarly, NO_x in the feed gas or electrolyte can be electrochemically reduced to NH_3 and result in continuous production of ammonia. As already discussed above, Licht et al. [9] retracted highly cited 2014 Science paper indicating the NO_x^- contamination in the chemicals as the cause of a false positive.

Besides, many nitrogen doped catalysts were developed in recent research. Ou et al. proposed that Mo supported on N-doped black phosphorus can catalyse electrocatalytic NRR with a potential of 0.18 V via the distal mechanism. [14] Recently, Sun et al. reported the application of Ru single-atom catalysts ($Ru@ZrO_2/NC$) for electrochemical NRR in 0.1 M HCl electrolyte at room temperature. Ru/NC gave the highest ammonia yield of 3.665 mg h^{-1} mg_{Ru}^{-1} at -0.21 V vs. RHE. The nitrogen doping in the carbon support played an important role of stabilizing and dispersing Ru single atomic sites by coordination bonds. However, N doping might be the nitrogen source instead of the feeding nitrogen gas. If nitrogen-content catalysts are used in NRR, a strict set of control experiments to identify and then eliminate or quantify the sources of contamination, becomes crucial.

3.3 Scope of this chapter

The objective of this work is to explore advanced electrocatalysts for the preparation/realization of more efficient electrodes and devices for the electrocatalytic reduction of $N_{3.}$

The experimental methods and procedures developed for preparing and testing the electrocatalysts are discussed in detail in this chapter. Particularly, a 3D-type new electrode and a non-conventional type of electrocatalytic cell are here presented. As electrocatalysts, a series of Fe-based MOFs (Fe@Zn/SIM-1) were synthesized in collaboration with CNRS-CPE in Lyon. These electrocatalysts are then deposited on a carbon gas diffusion layer and tested in NRR, also in their carbonized form.

Many efforts have been made to avoid any kind of ammonia contamination (out-system or intra-system) and to understand if results from testing are affected by false positive. A very accurate UV-visible spectrophotometric method was used for ammonia detection. This analytical technique, coupled with blank tests with inert gas (such as He or Ar) are more reliable than the use of $^{15}N_2$, which requires to operate in batch reactors rather than in a continuous gas-phase due to the cost of this reactant. Additional blank tests to exclude that ammonia detected could form from other sources, such as N contaminations in the electrodes/membranes, or present in the gas feed (as NO_x, for example), were also made. Note also that this method used for ammonia detection was adapted from the very sensitive method used to monitor ammonium ions at sub-ppm level in environmental tests. Thus, we found it preferable with respect to alternative methods suggested in literature, such as by NMR, ammonia gas electrodes or mass quadrupole, as it resulted more accurate and reliable.

Specific objective of this chapter is to evaluate the electrocatalytic activity of this particular class of MOFs in NRR. In relation with the obtained results, also taking into account ammonia contaminations, the design of the MOF-based catalysts was then properly modified to improve their catalytic performance in NRR.

3.4 Design of electrochemical system for ammonia synthesis

3.4.1 Design of electrochemical cell

A homemade gas-solid-liquid three phase reactor was realized and used for the electrocatalytic tests. The schematic view of the electrocatalytic flow reactor for ammonia synthesis is shown in Figure 3.1.

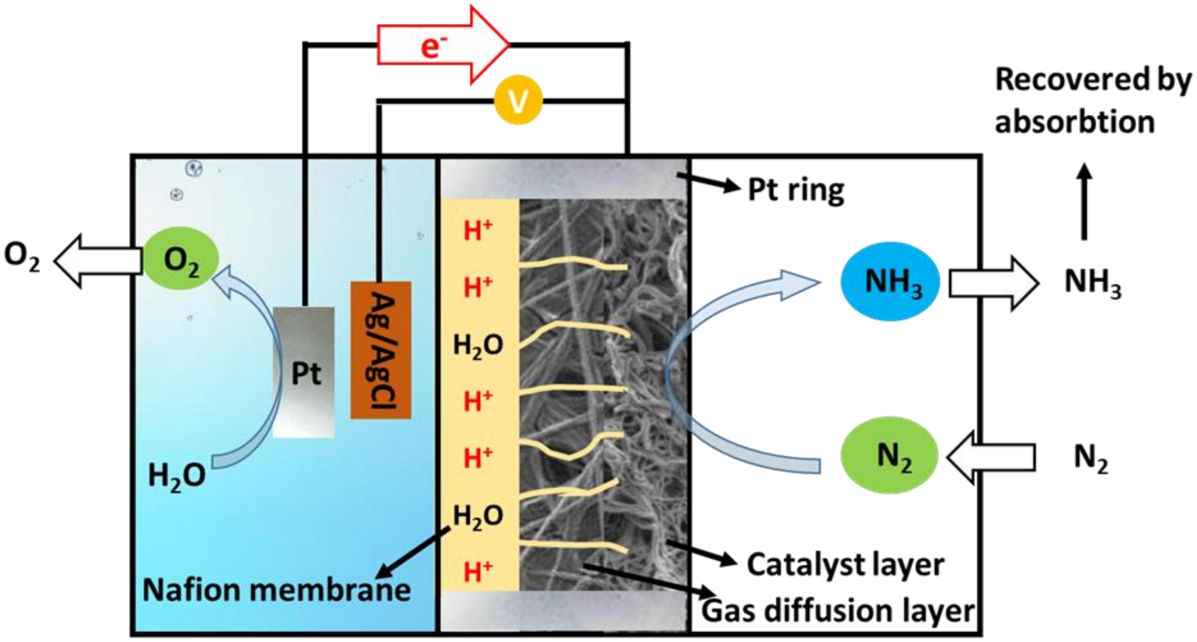

Figure 3.1 Schematic view of the three-phase reactor for electrochemical ammonia synthesis.

The cell operates at room temperature and atmospheric pressure. The counter and reference electrodes (Pt rod and Ag/AgCl, respectively) are immersed into the anode hemi-cell (where the oxidation of H_2O to O_2 occurs) containing a liquid electrolyte (the anolyte), while the cathode hemi-cell for NRR reaction operates in gas phase without a liquid electrolyte (electrolyte-less conditions). This type of electrocatalytic reactor is thus quite different from the conventional electrocatalytic reactors operating in liquid phase. The main advantages of this novel configuration are that gas-phase operation avoids issues related to low N_2 solubility in the electrolyte and allows an easier recovery of the ammonia produced. Moreover, a higher coverage of gas reactant (N_2) on the electrode surface, being not limited from solubility in the electrolyte and double-charge diffusion phenomena. The cathode hemi-cell (where ammonia is synthetized) operates with a continuous flow of nitrogen as reactant. After passing through the catalyst layer, the gas mixture (nitrogen containing the as-produced hydrogen and ammonia) exits from the reactor and goes to an absorber containing dilute sulfuric acid (0.001 M). The two compartments (the liquid anode and the gas cathode chambers) are physically separated by the membrane electrode assembly (GDL + electrocatalyst + Nafion), which represents the working electrode. The membrane electrode assembly was fabricated by hot pressing the electrocatalyst with a Nafion membrane (pre-purified) and a carbon-based gas diffusion layer (GDL), as described below.

3.4.2 Preparation of the membrane electrode

A commercial gas diffusion layer (SIGRACET GDL 29BC) supplied by SGL Group and a Nafion®115 membrane (Sigma Aldrich) were used to prepare the electrode. Nafion solution (10 wt %) was used to prepare the catalyst ink. All the other chemicals were of analytic grade and were used as received without any purification (supplied by Sigma Aldrich).

Electrocatalysts synthesis. In this chapter, a series of Fe-MOF and Fe-C catalyst, synthesized at the laboratories of CNRS-CPE Lyon, were tested at the University of Messina for testing in NRR. The samples were the following: 10 mol% Fe@Zn/SIM-1, 10 mol% Fe@Zn/SIM-1 Carbonized, 1 mol% Fe@Zn/SIM-1, 1 mol% Fe@Zn/SIM-1 Carbonized, and 2 mol% Fe@Zn/SIM-1. Notes, the 10 mol% Fe corresponds the percentage exchange between Fe and Zn in the structure of the SIM-1.

Synthesis of 10 mol% Fe@Zn-SIM-1 (Fe-SIM-1): In a typical synthesis, 3.993 g of 4-methyl-5-imidazolecarboxaldehyde (27 mmol) were placed in a round bottom flask with 100 mL of absolute ethanol under vigorous stirring. Then, 1.626 g of $Zn(NO_3)_2 \cdot 6\ H_2O$ (5.5 mmol) and 0.0903 g of $FeCl_2 \cdot 4\ H_2O$ (0. 45 mmol) were rapidly added to the solution. After refluxing for 48 h under stirring of 600 rpm, the powder was isolated by centrifugation and further washed with ethanol and dichloromethane for three times and finally dried at 90°C in oven.

Preparation of the catalyst on Gas diffusion layer. 10 mg of the electrocatalyst were suspended in 5 mL of ethanol and 50 μL of 10 wt% Nafion solution. The solution was sonicated for 90 min to obtain a homogeneous mixture, which is deposited by spray drying onto a gas-diffusion layer (GDL), and then dried at 80°C overnight.

Nafion membrane pretreatment. A commercial Nafion® 115 membrane was cut into small pieces and treated with 3 wt. % H_2O_2 water solution for 1 hour at 80 °C. Then, the pieces of membrane were treated in 0.5 mol/L H_2SO_4 solution for 1 hour at 80 °C under stirring, followed by rinsing until neutral pH. Finally, the obtained Nafion was kept in deionized water.

Membrane electrode assembly. The GDL, after depositing the catalyst, and the pre-treated Nafion membrane were hot-pressed together at 80 atm and 130 °C for 30 s. The active catalytic material was located between these two layers. The size of the electrodes was 2 cm^2. The actual loading amount was weighed and calculated.

3.5 Reaction conditions and calculations

All of the electrochemical measurements were carried out at 20°C using a potentiostat/galvanostat AMEL 2551. A Pt wire was used as the counter electrode. All potentials were measured against Ag/AgCl reference electrode (3 M KCl). The anodic section contains a liquid electrolyte (0.5 M KOH) for water electrolysis to generate the protons and electrons. The reactant N_2 was continuously fed (20 mL min^{-1} of N_2 with purity, 99.9999 %), and the flow coming out from the electrocatalytic reactor outlet (containing a mixture of N_2 and ammonia) is sent to a liquid absorber containing a 1 mL of 0.001 M H_2SO_4.

Ammonia formation rates were calculated using the following equation:

$$r_{NH_3}(\mu g \cdot mg_{eCAT}^{-1} \cdot h^{-1}) = \frac{x(ppm) \cdot V(mL)}{M_{eCAT}(mg) \cdot t(h)}$$

Where:

- r_{NH3}: ammonia formation rate in $\mu g \cdot mg_{CAT}{}^{-1} \cdot h^{-1}$.

- x (ppm): ammonia concentration in the detection solution in ppm (mg/L).

- V (mL): is volume of solution in liter.

- M_{eCAT} (mg): the amount of the electrocatalyst (mg) in the electrode.

- t (h): the reaction time in hours.

Faraday Efficiency (FE) of ammonia was determined using the following equations:

$$FE_{NH_3}(\%) = \frac{3 \times r_{NH_3}^{*}(mol \cdot cm^{-2} \cdot s^{-1}) \times t(s) \times S(cm^{-2}) \times F}{I(A) \times t(s)} \times 100\%$$

Where:

- F: Faraday constant (96485 $C \cdot mol^{-1}$).

- r^*_{NH3}: ammonia formation rate in $mol \cdot cm^{-1} \cdot s^{-1}$.

- S: is active area of the membrane electrode in cm^2.

- I (A): the average of current during the reaction,

- t (s): the reaction time in seconds.

3.6 Low level of ammonia detection methods: Ultraviolet-visible spectrophotometry (UV-Vis) with salicylic acid analysis method

In this thesis, the amount of ammonia formed was monitored by a highly-sensitive Ultraviolet-visible (UV-Vis) spectrophotometry method, which resulted preferable with respect to the alternative methods of ammonia detection, i.e. by using ammonium ion selective electrodes or using Nuclear Magnetic Resonance (NMR) [15]. Due to a discontinuous access to NMR equipment, differently from the spectrophotometric method that allows immediate analytic response during the experiments, we found less convenient the NMR method, although widely used by other authors [16] [17]. On the other hand, the UV-Vis spectrophotometric technique is the established method to analyse ammonium ions in environmental analysis.

The method used for low ammonia concentration detection was adapted from the standard methods for analysing ammonia in wastewater [15]. Under alkaline conditions, $Na_2\,[Fe\,(CN)_5\,NO]\bullet 2H_2O$ as catalyst, NH_3 and NH_4^+ in water react with salicylic and hypochlorite ions to form blue compounds. After 1 hour of reaction, the absorbance was measured by a UV-Vis spectrophotometric. Reproducibility tests indicate an average error of less than ±5% in the estimation of the ammonia formation rate.

An UV-Vis spectrophotometer (Thermo Fischer Evolution 200) was used at fixed wavelength (λ=655 nm) with a light path of 1 cm.

Reagents used:

1. Colouring solution: sodium salicylate (0.4 M) and sodium hydroxide (0.32 M);

2. Oxidation solution: sodium hypochlorite (active chlorine = 3.5 g/L) and sodium hydroxide (0.75 M);
3. Catalyst solution: 0.1g $Na_2 [Fe (CN)_5 NO]•2H_2O$ dissolved in 10 mL with deionized water.
4. Standard ammonium solution (10 ppm NH_4^+).

All these are aqueous solutions prepared with ultrapure water.

Procedure:

The ammonia determination was made by sampling 5 mL from the absorbing trap (sample solution) after NRR tests. Then 50 μL of oxidizing solution, 500 μL of colouring solution and 50 μL of catalyst solution were added respectively to the sample solution. Absorbance measurements were performed after 1 hour at $\lambda = 655$ nm at room temperature. It is of great importance to analyse the resulting solution by UV-Vis exactly after 1 h from the addition of the three reactant solutions to the sample solution. The calibration curve used for estimation of NH_3 was obtained after applying the above procedure to standard ammonia solutions at different concentrations, as shown in Figures 3.2.

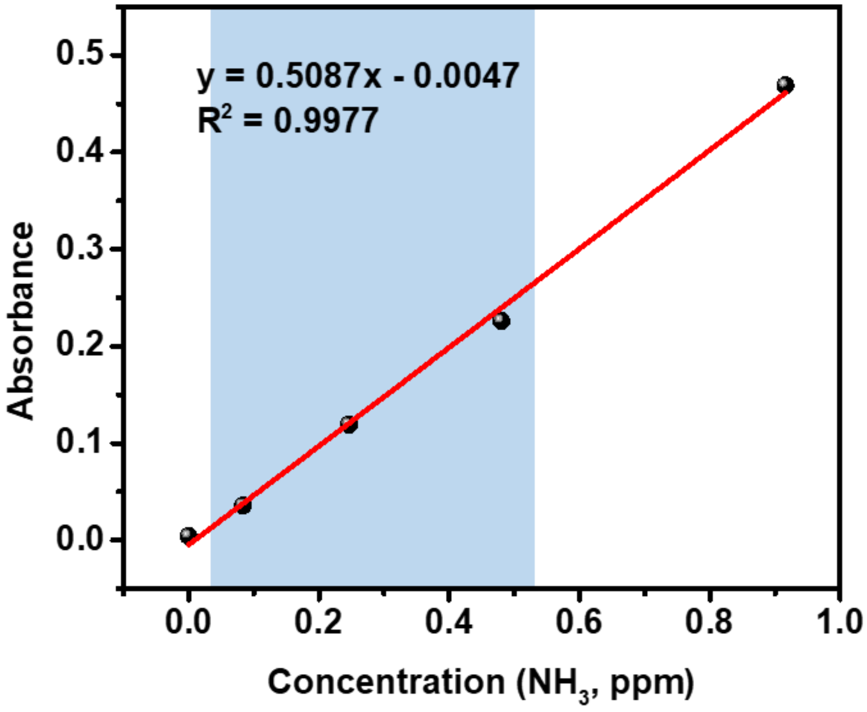

Figure 3.2 Spectrophotometry with salicylic acid: calibration curve used for calculation of NH_3 concentrations.

Wavenumber selectivity:

The wave scan of the solution to select the detection wavenumber of light is shown in Figure 3.3. The maximum absorbance is centred at 655 nm for all the ammonia solution concentrations.

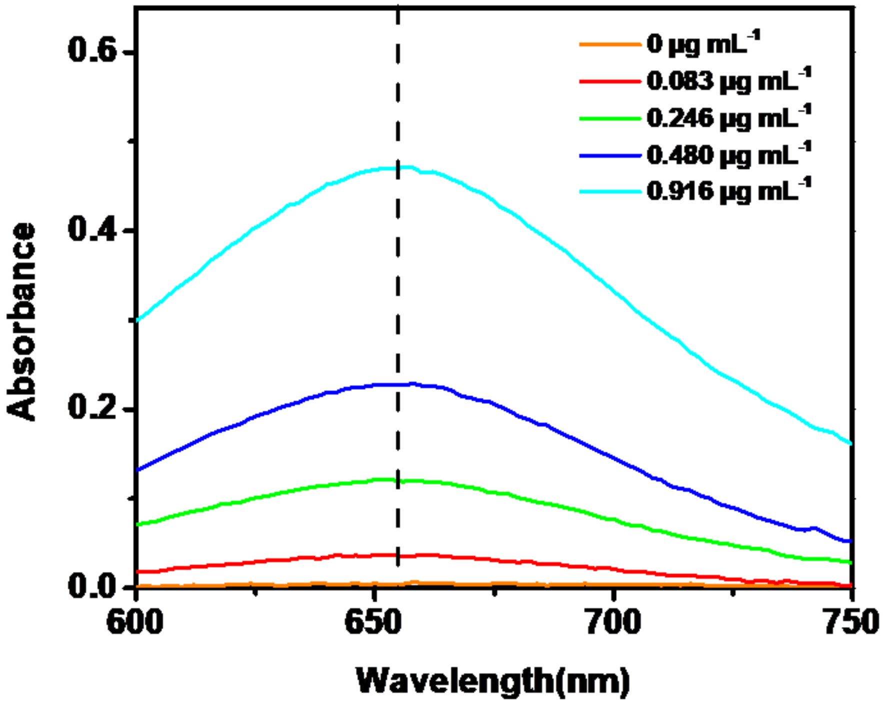

Figure 3.3 Wave scan of the solution to select the detection wavenumber of the light.

3.7 Experimental protocol operations in NRR.

3.7.1 Preliminary exploration: Fe@Zn/SIM-1 in NRR

The effect of iron loading in MOF electrocatalysts on the performances in NH_3 formation by N_2 and H_2O co-electrolysis at room temperature and atmospheric pressure is summarized in Figure 3.4. The ammonia absorber solution was collected and tested per hour. After each test, the absorber was filled with new solution. Figure 3.4 is a cumulative plot, thus the ammonia formation rate (that is the slope of this curve) decreases with time.

The following membrane-electrode assemblies were tested (in Table 3.1): 10 mol% Fe@Zn/SIM-1, 10 mol% Fe@Zn/SIM-1 Carbonized, 1 mol% Fe@Zn/SIM-1, 1 mol% Fe@Zn/SIM-1 Carbonized, and 2 mol% Fe@Zn/SIM-1 Carbonized as the electro catalyst. These series of Fe based MOF materials were synthesized and carbonized at the laboratory CNRS-CPE in Lyon and then assembled with a gas diffusion layer and tested in NRR at the University of Messina.

Table 3.1 A list of tested catalysts and reaction results.

Catalysts	**Cumulative production ammonia / µg**	**Reaction time / h**
10 mol% Fe@Zn/SIM-1	90.41	19
10 mol% Fe@Zn/SIM-1 Carbonized	3.38	20
1 mol% Fe@Zn/SIM-1	48.54	24
1 mol% Fe@Zn/SIM-1 Carbonized	6.18	24
2 mol% Fe@Zn/SIM-1 Carbonized	7.81	24
Fe_2O_3-CNT	7.17	6

The different iron content carbonized Fe-MOF shows similar low activity. The final values after 24 h of electrochemical reaction are 7.81, 6.18, and 3.38 µg of ammonia for the catalysts of 1 mol%, 2 mol%, and 10 mol% Fe@Zn/SIM-1 Carbonized, respectively, which is much lower than Fe@Zn/SIM-1 catalysts. The MOF structure seemed to promot the ammonia synthesis. The different iron content Fe@Zn/SIM-1 samples show different higher activity. 10 mol% Fe@Zn/SIM-1 exhibited a total ammonia amount of 90.04 µg, which is significantly higher than that of 1mol% Fe@Zn/SIM-1 (48.54 µg). The iron content in MOF structure is the key factors that influenced the catalytic activities. Otherwise, during the reaction, there was a yellow foam coming out from the catalyst. The Fe@Zn/SIM-1 is not stable in liquid phase.

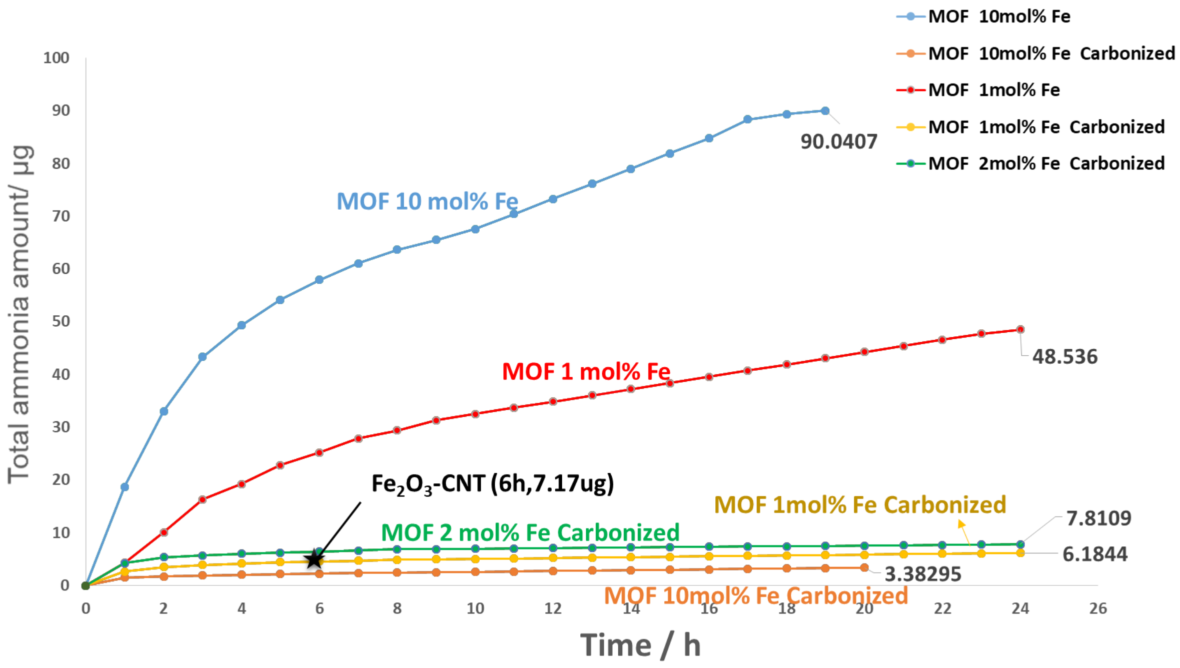

Figure 3.4 Total ammonia amount with the Fe@Zn/SIM-1, Fe@Zn/SIM-1 carbonized catalyst. 0.5 M KOH as an electrolyte, at −1.5 V vs. Ag/AgCl with room temperature and ambient pressure.

In order to confirm that ammonia was generated from feed N_2 gas in NRR and not from other sources, some blank tests were carried out on Fe@Zn/SIM-1 catalysts by replacing nitrogen with helium as feed gas. These blank tests were thus performed under the same conditions (at −1.5 V vs. AgCl) but in absence of feeding nitrogen into the electrocatalytic reactor. The results are shown in Figure 3.5. Unfortunately, ammonia is detectable in both N_2 and He atmosphere with the 10 mol% Fe@Zn/SIM-1 used as catalyst. Considering in this system, the linker in Fe based MOF is the 4-methyl-5-imidazolecarboxaldehyde, which contain Nitrogen atom in the MOF structure. It can be speculated that the ammonia comes from the MOF structure or the environment, considering the nitrogen in MOF structure and the poor catalytic activity. It could be better to carbonize the MOF catalyst or develop another suitable MOF catalyst not containing N atoms in the structure.

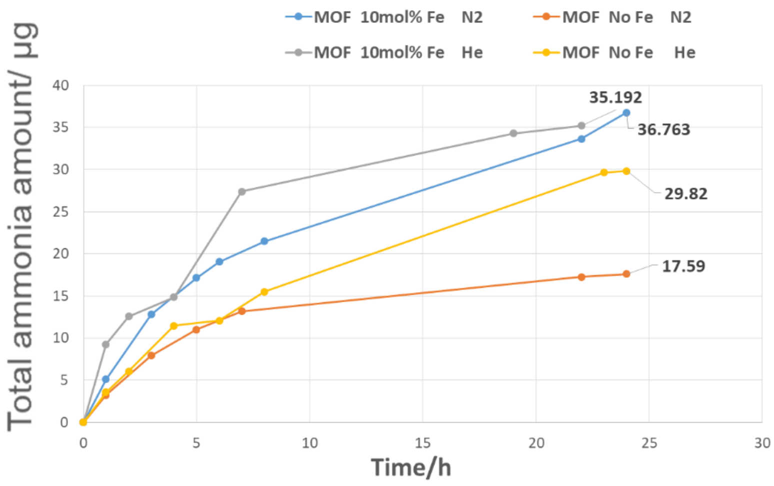

Figure 3.5 Total ammonia amount with the Fe@Zn/SIM-1, Fe@Zn/SIM-1 carbonized catalyst in He and N_2 saturated 0.50 M KOH

3.7.2 Identification and Elimination of Contamination in this thesis

A series of control tests were made to assure that ammonia form from N_2 feed rather than from other N sources and to verify that ammonia derives from an electrocatalytic process.

Gas purification. Gases (Ar, N_2) need to be scrubbed to remove background NH_3 or NH_3 from exogenous sources (x-NH_3), as well as NO_x contaminants, and the level of such species present (at a relevant limit of detection) demonstrated via salicylic acid analysis methods in control samples. A verification was made that NO_x was not present in the N_2 pure feed used in the present tests, and that contaminations by NH_3 were also not present in the feed section of the electrocatalytic apparatus. These control experiments were further supported by switching tests with He or Ar feed.

Membrane and catalysts purification. The Nafion membrane was purified and stored in ultrapure water. To remove the ammonia accumulated on the membrane during the period of storage, the assembled electrode (GDL-catalysts-Nafion membrane) was pre-treated at a lower potential for 30 minutes before the formal testing. The results are shown in Figure 3.6, after the 30-minute pre-treatment, the 2.48 μg contamination in membrane and catalyst was released into the electrolyte. In the next two-hours test, almost no ammonia was detected (-0.1 V vs. Ag/AgCl is too low to active the catalyst). It can be assumed that the pre-treatment removes the contamination in the assembled electrode.

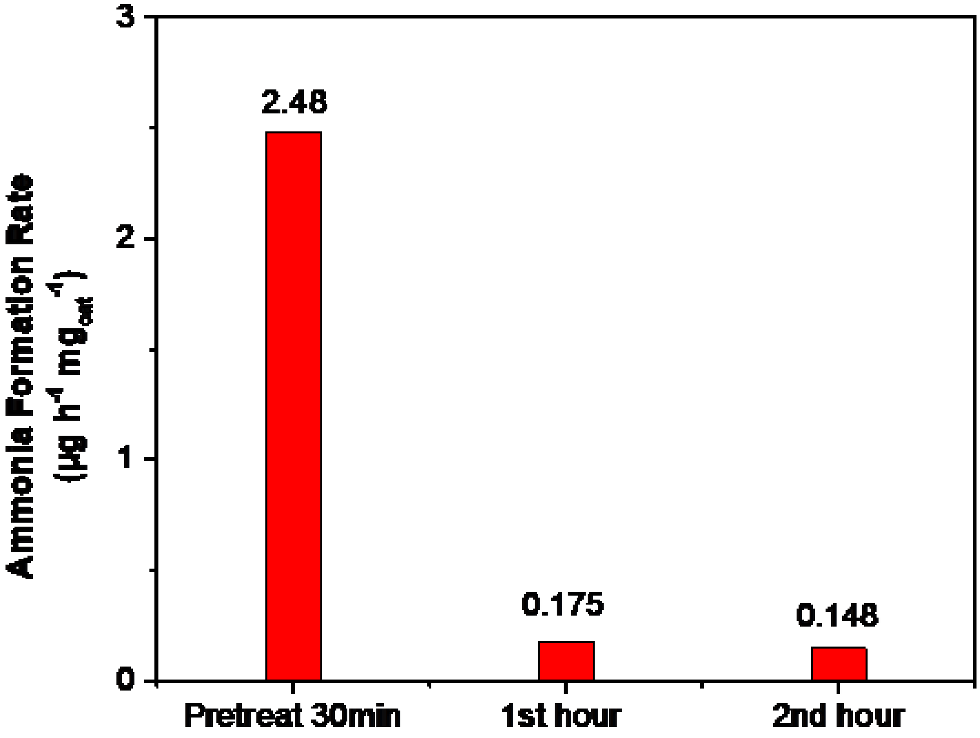

Figure 3.6 The identification of ammonia contaminations in assembled electrode at -0.1 V vs. RHE after 30-minute pre-treatment and 2 h of electrocatalytic tests at room temperature and ambient pressure.

Meanwhile, to eliminate the contaminations from the atmosphere and various surfaces, all electrochemical setups and consumables were carefully cleaned just before the NRR experiments.

Proof of NRR in control experiments. Especially for N-containing catalysts, more definite proof using isotope measurements with $^{15}N_2$ was recently reported to verify that the produced ammonia originate from the electro-reduction of nitrogen.[18] A number of detection methods have been well developed by the N_2 fixation community. [10] Isotope labelling tracer experiments are used to qualitatively confirm the source of ammonia by using a gas rich in $15N_2$ as the feed gas. After NRR, the $^{15}NH_4^+$ in the reaction solution was tested, usually using ^1H NMR spectroscopy. The characteristic $^{14}NH_4^+$ triplet can be used to quantify ammonia separately from $^{15}NH_4^+$, which is detectable as a strong doublet.[19] Quantification is possible by calibration with internal standard. Background $^{14}N_2$ and $^{14}NH_4^+$ are difficult to avoid in this 15NRR experiment, either quantification of both $^{15}NH_4^+$ and $^{14}NH_4^+$ is required, or demonstration that $^{15}NH_4^+$ is within experimental error of total NH_4^+ determined for the same experiment is necessary. The determined mol ($^{15}NH_4^+$) must be substantially greater than mol ($^{14}NH_4^+$) and be quantitatively consistent with the other measurements of NRR yield for this experiment to represent a sufficient proof of NRR.[20]

Although we stress the importance of isotope labelling experiments, it is acknowledged that the high price and small volume of $15N_2$ gas bottles makes such measurements challenging. The development of an easier methodology to avoid contamination and understand false positive is thus necessary. In our research, the further control experiments using Ar and N_2 at the same reaction potential are shown in Figure 3.7. After the initial phase of pre-treatment to stabilize the electrode, the first two hours of electrocatalytic tests are made by applying the chosen potential, but feeding Ar; then, the feed is switched to N_2, maintaining constant the applied potential and ammonia formation is monitored for at least 3h; after these tests, the potential is decreased to zero, and a feed of N_2 + 5% H_2 is fed to verify the catalytic (rather than electrocatalytic) activity in ammonia formation.

These latter control experiments regarded tests feeding N_2 and H_2, but without application of a potential to the electrocatalyst, to confirm that i) ammonia does not derive from the catalytic reduction of contaminant N-species and ii) the behaviour observed derives from the electrocatalytic reduction rather than from the catalytic reduction in presence of in-situ generated H_2.

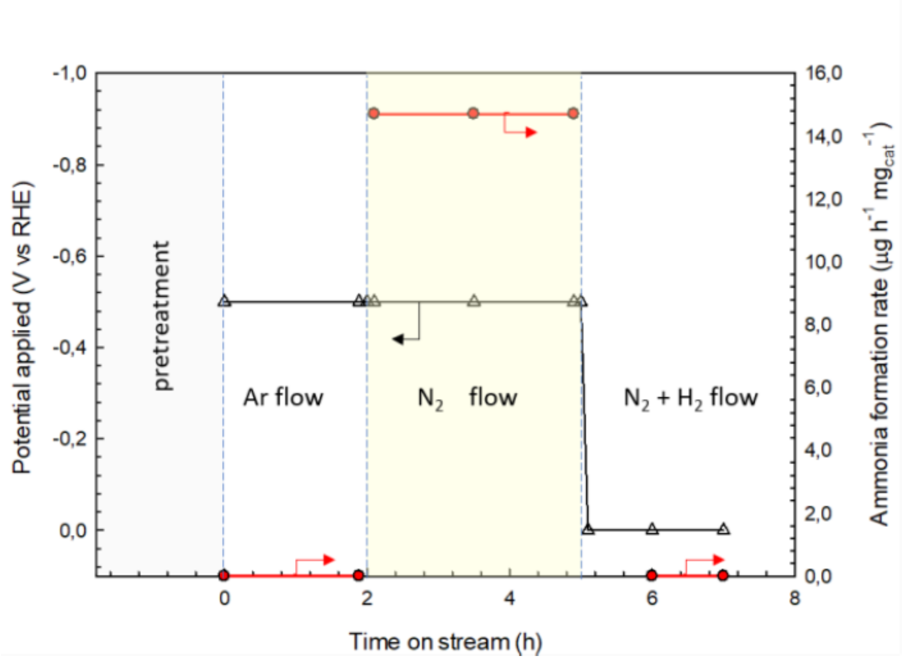

Figure 3.7 A sketch map of Argon control experimental protocol for NRR tests.

3.8 Conclusions

In this chapter, Fe-MOF-based (Fe@Zn/SIM-1) electrodes were prepared and assembled to be used in ammonia reduction process by using an advanced engineered three-phase reactor, working in gas-phase. After the preliminary exploration, it can be speculated that the ammonia comes from the MOF structure or the environment, considering the nitrogen in MOF structure and the poor catalytic activity. Therefore, a more water-stable Fe-MOF catalyst with no nitrogen atoms in the structure is required for NRR.

The identification and elimination of contamination in electrochemical nitrogen reduction studies were discussed in depth. A range of experimental control measurements were applied in this thesis work to ensure that the detected ammonia is produced from dinitrogen rather than other extraneous contamination. Argon control electrochemical measurements were presented as an easier and convenient alternative to isotope labelling methods.

3.9 Connected Experimental Section

Low level of ammonia detection methods: Ultraviolet-visible spectrophotometry (UV-Vis) with salicylic acid analysis methods. The amount of ammonia formed is monitored by a highly-sensitive Ultraviolet-visible (UV-Vis) spectrophotometry method, which resulted preferable with respect to the alternative tested methods of ammonia detection, i.e. by using ammonium ion selective electrodes or using Nuclear Magnetic Resonance (NMR) [21]. Due to a discontinuous access to NMR equipment, differently from the spectrophotometric method that allows immediate analytic response during the experiments, we found less convenient the NMR method, although widely used by other authors [22]. On the other hand, the UV-Vis spectrophotometric technique is the established method to analyze ammonium ions in environmental analysis.

The method used for low ammonia concentration detection was adapted from the standard methods for analyzing ammonia in wastewater [23]. Ammonia concentration was detected by spectrophotometry with salicylic acid, which gives higher sensitivity and reproducibility with respect to the alternative tested methods, such as ion selective electrode analysis (Orion™ High- Performance Ammonia Electrode 9512HPBNWP) or ammonia detection by NRM. Reproducibility tests indicate an average error of less than ±5% in the estimation of the ammonia formation rate.

An UV-Vis spectrophotometer (Thermo Fischer Evolution 200) was used at fixed wavelength (λ=655 nm) with a light path of 1 cm.

3.10 References

[1] Ye, L.; Nayak-Luke, R.; Banares-Alcantara, R.; Tsang, E., Reaction:“green” ammonia production. *Chem* **2017,** *3* (5), 712-714.

[2] Yu, L.; Pan, X.; Cao, X.; Hu, P.; Bao, X., Oxygen reduction reaction mechanism on nitrogen-doped graphene: A density functional theory study. *Journal of Catalysis* **2011,** *282* (1), 183-190.

[3] Yaghi, O. M.; O'Keeffe, M.; Ockwig, N. W.; Chae, H. K.; Eddaoudi, M.; Kim, J., Reticular synthesis and the design of new materials. *Nature* **2003,** *423* (6941), 705-714.

[4] Falcaro, P.; Ricco, R.; Yazdi, A.; Imaz, I.; Furukawa, S.; Maspoch, D.; Ameloot, R.; Evans, J. D.; Doonan, C. J., Application of metal and metal oxide nanoparticles@ MOFs. *Coordination Chemistry Reviews* **2016,** *307*, 237-254.

[5] Das, R.; Pachfule, P.; Banerjee, R.; Poddar, P. J. N., Metal and metal oxide nanoparticle synthesis from metal organic frameworks (MOFs): finding the border of metal and metal oxides. *Nanoscale* **2012,** *4* (2), 591-599.

[6] Zhao, X.; Yin, F.; Liu, N.; Li, G.; Fan, T.; Chen, B., Highly efficient metal–organic-framework catalysts for electrochemical synthesis of ammonia from N_2 (air) and water at low temperature and ambient pressure. *Journal of Materials Science* **2017,** *52* (17), 10175-10185.

[7] Greenlee, L. F.; Renner, J. N.; Foster, S. L., The use of controls for consistent and accurate measurements of electrocatalytic ammonia synthesis from dinitrogen. *ACS Catalysis* **2018**.

[8] Chen, Y.; Liu, H.; Ha, N.; Licht, S.; Gu, S.; Li, W., Revealing nitrogen-containing species in commercial catalysts used for ammonia electrosynthesis. *Nature Catalysis* **2020**, 1-7.

[9] Licht, S.; Cui, B.; Wang, B.; Li, F.-F.; Lau, J.; Liu, S. J. S., Ammonia synthesis by N_2 and steam electrolysis in molten hydroxide suspensions of nanoscale Fe_2O_3. *Science* **2014,** *345* (6197), 637-640.

[10] Stuart Licht1, Baochen Cui, Baohui Wang, Fang-Fang Li, Jason Lau, Shuzhi Liu1, Science 14 Aug 2020:Vol. 369, Issue 6505, pp. 780, DOI: 10.1126/science.abe0412

[11] Greenlee, L. F.; Renner, J. N.; Foster, S. L., The use of controls for consistent and accurate measurements of electrocatalytic ammonia synthesis from dinitrogen. *ACS Catalysis* **2018**.

[12] Li, L.; Tang, C.; Yao, D.; Zheng, Y.; Qiao, S.-Z. J. A. E. L., Electrochemical nitrogen reduction: identification and elimination of contamination in electrolyte. **2019,** *4* (9), 2111-2116.

[13] Foster, S. L.; Bakovic, S. I. P.; Duda, R. D.; Maheshwari, S.; Milton, R. D.; Minteer, S. D.; Janik, M. J.; Renner, J. N.; Greenlee, L. F., Catalysts for nitrogen reduction to ammonia. *Nature Catalysis* **2018,** *1* (7), 490-500.

[14] Ou, P.; Zhou, X.; Meng, F.; Chen, C.; Chen, Y.; Song, J., Single molybdenum center supported on N-doped black phosphorus as an efficient electrocatalyst for nitrogen fixation. *Nanoscale* **2019,** *11* (28), 13600-13611.

[15] Hodgetts, R. Y.; Kiryutin, A. S.; Nichols, P.; Du, H.-L.; Bakker, J. M.; Macfarlane, D. R.; Simonov, A. N., Refining Universal Procedures for Ammonium Quantification via Rapid ^{1}H NMR Analysis for Dinitrogen Reduction Studies. *ACS Energy Letters* **2020,** *5* (3), 736-741.

[16] Nielander, A. C.; McEnaney, J. M.; Schwalbe, J. A.; Baker, J. G.; Blair, S. J.; Wang, L.; Pelton, J. G.; Andersen, S. Z.; Enemark-Rasmussen, K.; Colic, V., A versatile method for ammonia detection in a range of relevant electrolytes via direct nuclear magnetic resonance techniques. *ACS Catalysis* **2019**, 9 (7), 5797-5802.

[17] Duan, G. Y.; Ren, Y.; Tang, Y.; Sun, Y. Z.; Chen, Y. M.; Wan, P. Y.; Yang, X. J., Improving the Reliability and Accuracy of Ammonia Quantification in Electro‐and Photochemical Synthesis. *ChemSusChem* **2020,** *13* (1), 88-96.

[18] Andersen, S. Z.; Čolić, V.; Yang, S.; Schwalbe, J. A.; Nielander, A. C.; McEnaney, J. M.; Enemark-Rasmussen, K.; Baker, J. G.; Singh, A. R.; Rohr, B. A., A rigorous electrochemical ammonia synthesis protocol with quantitative isotope measurements. *Nature* **2019,** *570* (7762), 504-508.

[19] Zhou, F.; Azofra, L. M.; Ali, M.; Kar, M.; Simonov, A. N.; McDonnell-Worth, C.; Sun, C.; Zhang, X.; MacFarlane, D. R., Electro-synthesis of ammonia from nitrogen at ambient temperature and pressure in ionic liquids. *Energy Environmental Science* **2017,** *10* (12), 2516-2520.

[20] Suryanto, B. H.; Du, H.-L.; Wang, D.; Chen, J.; Simonov, A. N.; MacFarlane, D. R., Challenges and prospects in the catalysis of electroreduction of nitrogen to ammonia. *Nature Catalysis* **2019,** *2* (4), 290-296.

[21] Hodgetts, R. Y.; Kiryutin, A. S.; Nichols, P.; Du, H.-L.; Bakker, J. M.; Macfarlane, D. R.; Simonov, A. N., Refining Universal Procedures for Ammonium Quantification via Rapid 1H NMR Analysis for Dinitrogen Reduction Studies. *ACS Energy Letters* **2020,** *5* (3), 736-741.

[22] Nielander, A. C.; McEnaney, J. M.; Schwalbe, J. A.; Baker, J. G.; Blair, S. J.; Wang, L.; Pelton, J. G.; Andersen, S. Z.; Enemark-Rasmussen, K.; Colic, V., A versatile method for ammonia detection in a range of relevant electrolytes via direct nuclear magnetic resonance techniques. *Acs Catalysis* **2019,** *9* (7), 5797-5802.

[23] Perathoner, S.; Centi, G.; Su, D., Turning perspective in Photoelectrocatalytic cells for solar fuels. *ChemSusChem* **2016,** *9* (4), 345-357.

4 Fe based MOFs for N_2 Electrochemical Reduction under Ambient Conditions

4.1 Introduction

Metal-organic frameworks (MOFs), constructed by joining metal ions with organic ligands, have emerged as a category of functional materials for diverse applications. MOFs own fantastically high specific surface areas, easily tunable structures and functions [1]. MOFs are currently widely applied in many fields, such as molecular sensing [2], battery [3], catalysis [4], gas adsorption and separation [5], biomedicine [6], drug delivery [6], template materials [7], and pesticide testing [8]. In recent research, MOFs or their derived materials with diverse pore structure and metal centered sites have shown promising performances in electrocatalytic nitrogen reduction reaction (NRR).

Recently, Zhao et al. investigated three kinds of MOFs in NRR: Fe-based MIL-100(Fe), Co-based ZIF-67 and Cu-based HKUST-1 [9]. Among those, Fe-based MIL-100(Fe) displayed the best catalytic activity with the highest ammonia formation rate and current efficiency (2.12×10^{-9} mol s^{-1} cm^{-2} and 1.43 %, respectively), under 1.2 V cell voltage and 90 ^{o}C. The rich 3D interconnected porous structure of MOFs is beneficial for the enrichment and diffusion of reactant nitrogen molecules, while the massive atomically distributed metal ions (Fe^{3+}, Co^{3+}, and Cu^{2+}) in MOFs acting as Lewis acids are believed to be the active sites, which withdraw p-electrons from N_2 molecules, weakening the $N{\equiv}N$ bonds.

Ling's group reported a catalyst@metal organic framework (MOF) hybrid (Ag-Au@ZIF) providing excellent NRR performances with a high Faradaic efficiency to ammonia (18 ± 4%) at ambient conditions.[10] Here, a hydrophobic layer of zeolitic imidazolate framework-71 (ZIF) was introduced over a traditional NRR electrocatalyst's (Ag-Au particle) surfaces to suppress competing HER and enhance reactant-catalyst interactions. The mechanism of analytical interpretation showed that the ZIF layer played a vital role in the whole reaction process. By encapsulating the catalytically active surfaces, the ZIF not only serves as a hydrophobic barrier to block the entry of water for inhibiting hydrogen evolution reaction (HER), but also allows the selective N_2 access to the enclosed electrocatalyst and provides interfacial cavities for N_2 accumulation as a standby.

Very recently, Duan et al [11]. reported a class of zero-dimensional (0D), bimetallic nickel, iron-MOF (NiFe-MOF) electrocatalysts, affording a Faradaic efficiency to ammonia of 11.5% and ammonia yield rate of 9.3 μg h^{-1} $mg_{cat}{}^{-1}$ at -345 mV (RHE). By dramatically decreasing MOF size, the charge transport pathway is shortened to a few nanometers, thus greatly improving the electron transfer at electrode/electrolyte interface. A large mesoporosity (9–38 nm) also formed between adjacent nano-sized MOFs for providing numerous gas transport channels at the three-phase boundary of the electrode.

Moreover, the MOF structures can be modified in a number of ways to obtain electrochemically active species. For example, by pyrolysis of MOFs under an inert atmosphere at a suitable temperature, the metal ions can be transformed to metal nanoparticles (NPs), metal oxide nanostructures, or both depending on the reduction potential of the metal atoms present in the MOFs [12], which are highly dispersed on or embedded in a ligand-derived carbon matrix. In comparison with other carbon-based catalysts, MOF-derived carbon-based nanomaterials have great advantages in terms of tailorable morphologies, hierarchical porosity and easy functionalization with other heteroatoms and metal/metal oxides, which make them highly efficient as direct catalysts or as catalyst supports for many important reactions.

Mukherjee et al [13]. reported a metal-organic framework derived nitrogen-doped nanoporous carbon as an electrocatalyst for the NRR at a high rate of 3.4×10^{-6} mol cm^{-2} h^{-1} with a Faradaic efficiency to ammonia of 10.2% at room temperature. What is noteworthy is that the alkali metal ions such as K^+ played a promotional role in donating electrons, thereby driving the evolution of the second NH^3 molecule without adding even higher potential.

Very recently, Sun et al [14]. reported the application of Ru single atom catalysts for NRR in 0.1 M HCl electrolyte at room temperature. Composites with single Ru sites encapsulated in a nitrogen-doped porous carbon matrix with ZrO_2 nanoparticles ($Ru@ZrO_2/NC$) were prepared from a Ru-loaded Zr-based MOF with amino-containing ligands (UiO-66-NH_2) via a thermal pyrolysis method, and the ZrO_2 particles were further washed off by HF leaching to give Ru/NC. Ru/NC gave the highest ammonia yield of 3.665 mg h^{-1} mg_{Ru}^{-1} at -0.21 V vs. RHE. These results indicate that only the reduction of Ru particle size to the atomic-level can effectively suppress HER. The nitrogen doping in the carbon support played an important role in stabilizing and dispersing Ru single atomic sites by coordination bonds, and the presence of ZrO_2 significantly suppressed the HER, contributing to the higher Faraday efficiency to ammonia of $Ru@ZrO_2/NC$ comparing to Ru/NC.

In the previous chapter, the electrocatalytic behavior of Fe@Zn/SIM-1 MOF class in NRR was reported through preliminary tests using a compact three-phase electrochemical device. As described, these tests were carried out adopting a rigid protocol to avoid false positive due to contaminations, on both the Fe@Zn/SIM-1 forms (as MOFs and in the pyrolyzed form). Results showed some activity of these materials in NRR; however, the performances strongly decreased after pyrolysis of the electrocatalysts, and in general this class of MOFs were not much stable in the reaction environment. A possible explanation is that ammonia produced in these tests majorly came from the Fe@Zn/SIM-1 itself, which contained nitrogen atoms in the molecular structure. This hypothesis was also confirmed by check analysis with inert gas (He, or Ar), as required by the analytical protocol adopted to avoid false positive. These results also confirmed that Fe@Zn/SIM-1 MOFs are nor stable in aqueous solution, permeated from the Nafion membrane directly assembled with the MOF-based electrode.

Therefore, a different MOF electrocatalyst would be required, more stable and suitable to be used as efficient electrode for NRR, and thus not containing nitrogen atoms in its structure. Moreover, as currently used in the industrial process for ammonia synthesis, the introduction of potassium in the catalysts can facilitate charge transfer from K^- ions to the iron-based catalyst surface, balancing the dissociative chemisorption between H_2 and N_2, and suppressing side reactions, thus improving both activity and stability [15].

4.2 Scope of the chapter

In the view of exploiting the great properties of MOF materials, scope of this chapter is to design a more suitable electrode based on MOFs but trying to overcome limitations encountered with Fe@Zn/SIM-1 MOFs (as described in the previous chapter).

The main aspects to take into account in designing the new electrodes are i) the MOF should not contain nitrogen atoms in the molecular structure (thus eliminating false positive in ammonia detection and ii) the MOFs materials should be more stable in water and/or in basic aqueous solution.

A series of improved Fe-based and Fe-alkali metal-based MOF UiO-66-$(COOH)_2$ were thus synthesized by cation exchange reaction technique, the proton of carboxylic acid was replaced by an iron cation. This new class of MOFs are more stable both in water and in air, and can be a good candidate for the preparation of efficient electrodes for NRR. After proper assembling with a carbon gas diffusion layer (GDL), the electrodes were studied for the room temperature electrocatalytic synthesis of NH_3 from H_2O and N_2 in a gas–liquid–solid three-phase reactor. On the basis of the information obtained by the characterization of catalyst composition, structure and morphology, activity behaviors are discussed.

4.3 Experimental

4.3.1 Synthesis of Fe@UiO-66-$(COOH)_2$

UiO-66 is a zirconium (IV) based MOF with a highly stable $Zr_6O_4(OH)_4$ inorganic brick, where each Zr_6-Octahedra is bound to twelve 1,2,4-benzenedicarboxylic acid

(BDC) linkers [16]. UiO-66 was functionalized with two free carboxylic groups on the terephthalate linkers labelled as UiO-66-$(COOH)_2$. The introduction of free carboxylic acid groups on the organic linker induced modifications of the pristine UiO-66(Zr), which, for both solids, led to an enhanced Brønsted acidity and proton conductivity, due to the sufficient mobility of the acidic protons of the free carboxylic groups.[17] One $Zr_6O_4(OH)_4$ inorganic brick (Zr_6-octahedra) is bound to twelve 1,2,4,5-benzenetetracarboxylic acid (BDC-$(COOH)_2$). The UiO-66-$(COOH)_2$ crystalline structure is shown in Figure 4.1. The reactive nature of the uncoordinated carbonyl groups, as well as the high thermal and chemical stabilities of UiO-66-$(COOH)_2$, turn it into a good candidate to bind with metal cations. During the stay in Lyon, a series of Fe-base and Cu-based MOF UiO-66-$(COOH)_2$ by cation exchange reaction were designed and synthesized. The UiO-66-$(COOH)_2$ was supplied by Centre national de la recherche scientifique (CNRS) Lyon.

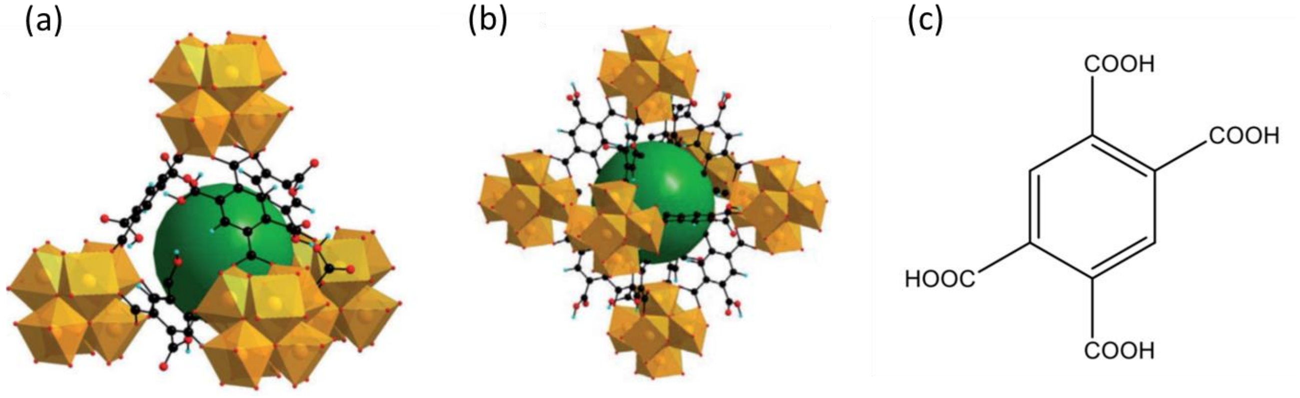

Figure 4.1 The UiO-66(Zr)-$(COOH)_2$ crystalline structure: (a) tetrahedral cage, (b) octahedral cage. The large green spheres represent the void regions inside the

cages (Zr polyhedra; C black; O red, and H cyan), (c) The structure of BDC-$(COOH)_2$.

I: Fe@UiO-66-$(COOH)_2$ Synthesis- Start from Fe (II) Oxalate

Based on the assumption of eight exchangeable protons per formula unit of UiO-66-$(COOH)_2$, the experimental applied amount of acid and metal oxalate solution always contained the twelve-fold amount of exchangeable charges.

Experimental applied quantities for the cation exchange with Iron in H_2SO_4 are summarized in Table 4.1. In a round bottom flask, the metal oxalate and MOF were suspended in H_2O; then, H_2SO_4 was added. The suspension was heated to 80°C for 4 h, allowed to cool down at room temperature overnight, afterwards washed with deionized water until the supernatant was at pH 7 and then dried at 80°C for 24 h.

Table 4.1 Experimental applied quantities for the cation exchange with Iron in H_2SO_4. The quantity %Fe is defined as the experimental applied ratio of charges from Fe to protons. S% Fe= n (Fe): n (Zr).

Sample	S %Fe	m(MOF)/g	M(Fe oxalate)/g	M(H_2SO_4)/g	V(H_2O)/mL	Calculated wt% Fe
HWI-A-001-01	10	3.0	1.030	5.055	226.33	1.51
HWI-A-002-01	30	3.0	3.091	3.932	226.94	4.39
HWI-A-003-01	50	3.0	5.151	2.808	227.55	7.12

II: Fe/Fe-K/Fe-Na based UiO-66-$(COOH)_2$ Synthesis- Start from Fe(II) Acetate.

A summary of the optimized synthesis conditions is given in Figure 4.2. The reaction time was set to 5 minutes for all the exchange reactions. On the right-hand side of Figure 4.2, the values of metal acetate concentration were also reported (mol/L). The suspension was placed in a preheated oil-bath and stirred for 5 min. The supernatant before filtration was colourless in case of Fe infiltration.

The synthesized Fe@UiO-66-$(COOH)_2$, Fe-K@UiO-66-$(COOH)_2$ and Fe-Na@UiO-66-$(COOH)_2$ are reported in Table 4.2.

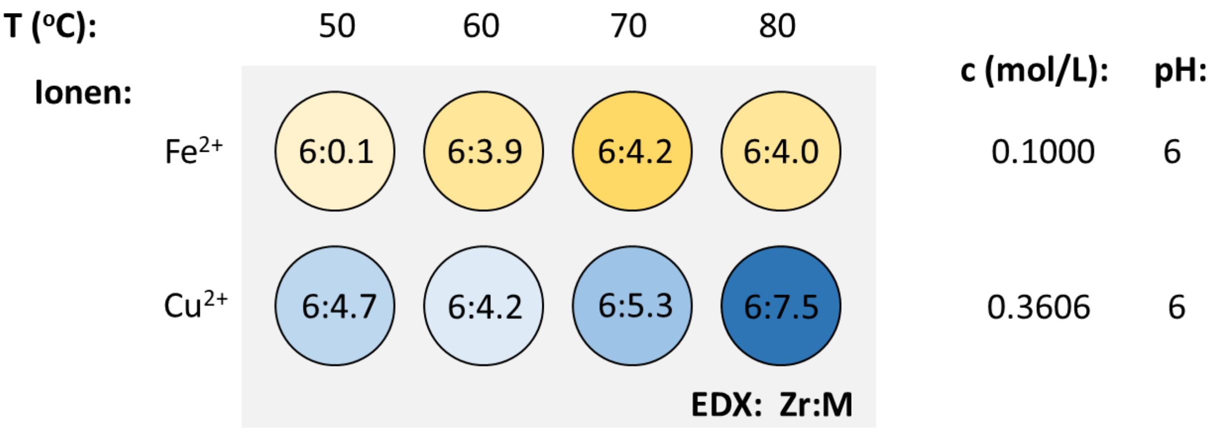

T (°C):	50	60	70	80	c (mol/L):	pH:
Ionen:						
Fe^{2+}	6:0.1	6:3.9	6:4.2	6:4.0	0.1000	6
Cu^{2+}	6:4.7	6:4.2	6:5.3	6:7.5	0.3606	6

EDX: Zr:M

Figure 4.2 Overview of optimized reaction conditions, the Zr: metal ratios as determined by EDX, as well as pH values of metal solutions before infiltration.[18]

Table 4.2 Experimental applied quantities for the cation exchange with Fe, Na, K. S% M means the theoretical metal cation exchange rate. S% M= n (M): n (Zr).

Sample	m(MOF)/ g	S %Fe	M(Fe acetate)/g	S % Na	M(Na acetate)/g	S % K	M(K acetate)/g
HWI-A-002-02	2.5	30%	0.4383	-	-	-	-
HWI-A-006-01	2.5	66%	0.8697	-	-	-	-
HWI-A-008-01	2.5	80%	1.0436	-	-	-	-
HWI-A-004-01	2.5	30%	0.4383	5%	0.0821	-	-
HWI-A-009-01	2.5	80%	1.0436	20%	0.2461	-	-
HWI-A-005-01	2.5	30%	0.4383	-	-	5%	0.099
HWI-A-010-01	2.5	80%	1.0436	-	-	10%	0.1472
HWI-A-007-01	2.5	80%	1.0436	-	-	20%	0.2944

4.3.2 Preparation of the membrane electrode

Preparation of the catalyst on gas diffusion layer. 40 mg of the electrocatalyst was suspended in a 5 mL of ethanol and 100 µL of 10 wt% Nafion solution. The solution was sonicated for 60 min to obtain a homogeneous ink, which was then deposited by spray-drying onto a gas diffusion layer (on both side) and then dried at 80^{o}C overnight.

Nafion membrane pretreatment. Nafion® 115 membrane was cut into small pieces and treated with some amount of 3 wt. % H_2O_2 water solution for 1 hour at 80 ^{o}C. Then, the pieces of membrane were treated in 0.5 mol/L H_2SO_4 solution for 1 hour at at 80 ^{o}C under stirring, followed by rinsing until neutral pH. Finally, the obtained Nafion was kept in deionized water.

Membrane electrode assembly. The GDL after depositing the catalyst and pretreated Nafion membrane were hot pressed together at 80 atm and 130 ºC for 30 s. The loading amount was around 1 mg cm^{-2} and size of the electrodes was 2 cm^2.

4.3.3 Reaction conditions and calculations

All the electrochemical measurements on Fe-based MOF were carried out in a three-phase reactor, working in gas phase. The liquid anode chamber contained a liquid electrolyte (the anolyte) for oxygen evolution reaction (OER) also generating the protons and electrons, which moved towards the cathode where they were used in the solid membrane (gas-diffusion) electrode for NRR.

The solid zone consisted of a Nafion membrane, a catalyst layer and a gas diffusion layer. The reactant N_2 was continuously fed (20 mL min^{-1} of N_2 with purity 99.99%) to the cathode gas side. The amount of ammonia formed was monitored by a spectrophotometry method, as described in the previous chapter. Both the solution in the cathode output absorber and the anode electrolyte were analysed to measure the total ammonia/ammonium production. The N_2 flow was introduced to the cathode part of the cell 30 min before starting the reaction and then continuously fed till the end of the test. A potentiostat /galvanostat (AMEL 2551) provided the working potential. A Pt rod was used as the counter electrode. All the potentials were measured against Ag/AgCl reference electrode (3 M KCl). The Fe-MOF loaded on the gas diffusion layer was used as the working electrode.

4.4 Results

4.4.1 Morphological measurements: SEM and XRD

The catalysts were characterized using Scanning Electron Microscope (SEM) and X-Ray Diffraction.

The UiO-66-$(COOH)_2$ was supplied by the “Centre national de la recherche scientifique (CNRS) Lyon”. Figure 4.3 shows SEM images of the spray-dried material, evidencing the formation of spherical superstructures with diameters between 2 and 4µm.

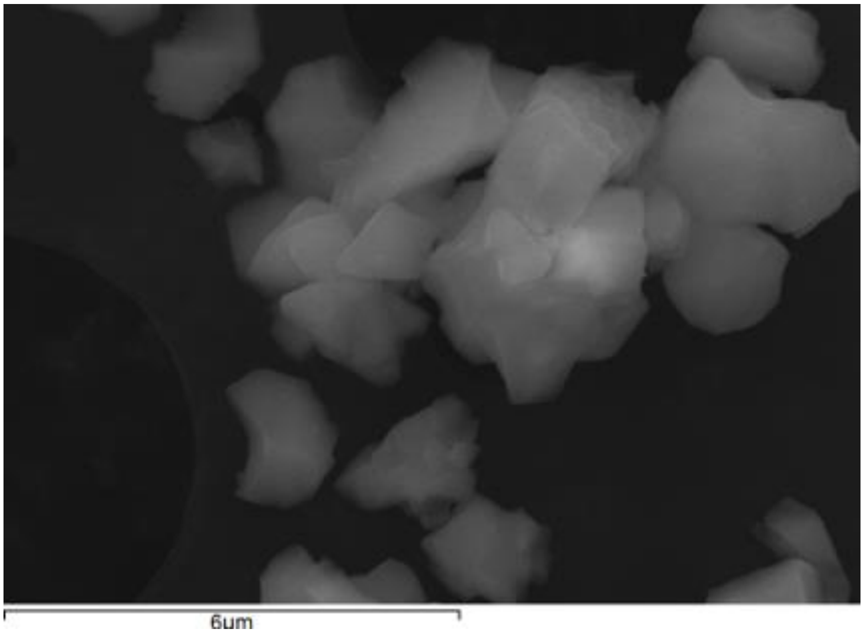

Figure 4.3 SEM images of UiO-66-$(COOH)_2$.

XRD patterns of the as-synthesized and activated samples were obtained and compared with patterns from simulated data to test the impact of activation and addition of functional groups on the crystal structure.

Figure 4.4 shows the XRD patterns of Fe@ UiO-66-$(COOH)_2$ from iron oxalate at different Fe % exchange compared to the pattern of pristine UiO-66-$(COOH)_2$. The patterns of the samples with Fe were significant changed, which means that unfortunately the crystalline MOF structure was highly modified after metal insertion procedure, except for the lower Fe-content sample. It is assumed that the structure of oxalate was destroyed, probably oxalic acid formed during exchange, and we were looking for more suitable alternative. Acetate is the most obvious choice as far as acetic acid could be removed by evaporation during the exchange.

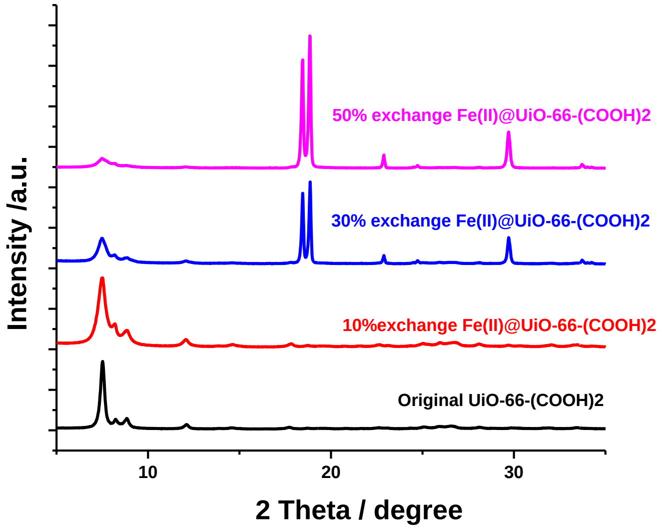

Figure 4.4 Comparison between XRD patterns of pristine UiO-66-$(COOH)_2$ and Fe@ UiO-66-$(COOH)_2$ from iron oxalate

The metal insertion procedure was thus modified starting from Fe (II) acetate, and also inserting K or Na in the MOF structure, which may strongly improve the electrocatalytic performance in NRR, as discussed in the introduction. A series of Fe@UiO-66-$(COOH)_2$, Fe-K@UiO-66-$(COOH)_2$ and Fe-Na@UiO-66-$(COOH)_2$ were synthesised from Fe (II) Acetate.

XRD patterns were collected for all the samples and compared to the pattern of the pristine UiO-66-$(COOH)_2$, as shown in Figure 4.5. It can be observed that the XRD patterns remained unaltered after metal insertion, evidencing that the MOF structure did not undergo any modification in the crystalline structure.

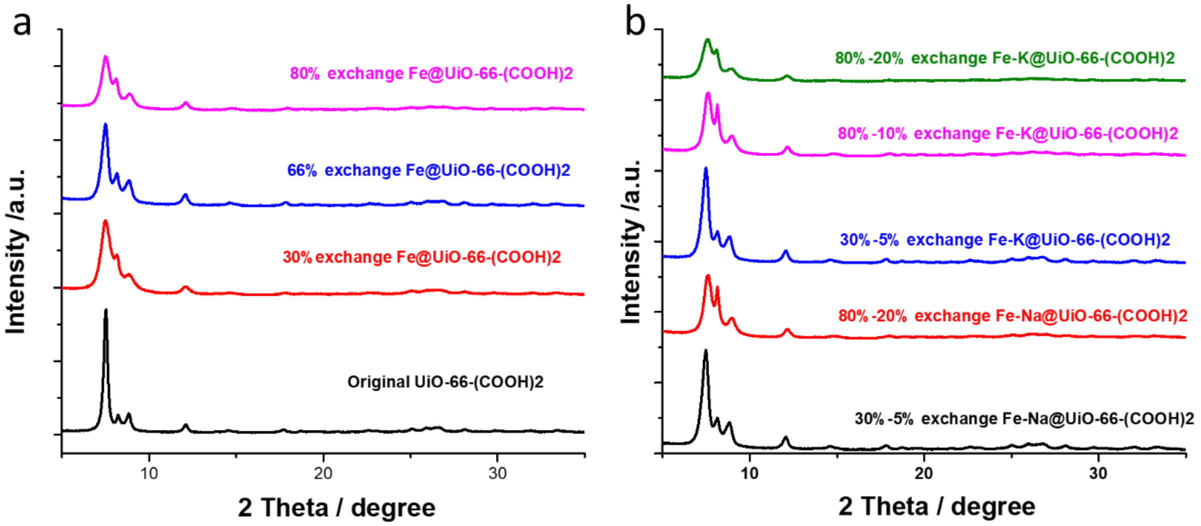

Figure 4.5 Comparison between XRD patterns of (a) UiO-66-$(COOH)_2$ and Fe@UiO-66-$(COOH)_2$, (b) Fe-Na@UiO-66-$(COOH)_2$ and Fe-K@UiO-66-$(COOH)_2$

4.4.2 Elemental analysis: ICP-MS

The metal element content of the metal-based MOF samples was determined by Inductively Coupled Plasma Mass Spectrometry (ICP-MS) analysis.

I: Fe@UiO-66-$(COOH)_2$ Synthesis- Start from Fe (II) Oxalate

Iron loading values obtained by ICP-MS measurements are reported in Table 4.3. It can be noted that the effective loading values are higher than the calculated loading values, except for the 10% exchange Fe@UiO-66-$(COOH)_2$ sample.

Table 4.3 The actual Iron content in Fe@UiO-66-$(COOH)_2$

Sample	Description	S %Fe	Calculated wt% Fe	ICP Result wt% Fe
HWI-A-001-01	10% exchange Fe@UiO-66-$(COOH)_2$	10	1.51	$<$0.1
HWI-A-002-01	30% exchange Fe@UiO-66-$(COOH)_2$	30	4.39	12.14
HWI-A-003-01	50% exchange Fe@UiO-66-$(COOH)_2$	50	7.12	18.77

II: Fe/Fe-K/Fe-Na based UiO-66-$(COOH)_2$ Synthesis- Start from Fe(II) Acetate.

Fe, Na and K loading values obtained by ICP-MS measurements are reported in Table 4.4. The effective alkali metal loading values are lower than what expected, due to the way of preparation. In general, whatever we put inside a MOF, the actual loading amount is lower than the theoretical calculating value due to diffusion limitations. Here, the Fe loading is quite good in accordance to the expected value. But when we try to introduce additional Na or K, there can be both diffusion limitation and the exchange with those cations might be less electronically favored that with Fe. In further improvement, only Na or K would be introduced to compare expected and actual exchange rate and develop a more reasonable experimental scheme.

Table 4.4 The actual Fe, Na, K content in Fe@UiO-66-(COOH)$_2$, Fe-Na@UiO-66-(COOH)$_2$, and Fe-K@UiO-66-(COOH)$_2$

Sample	Description	Calculated wt% Fe	ICP Result wt% Fe	Calculated wt% Na	ICP Result wt% Na	Calculated wt% K	ICP Result wt% K
HWI-A-002-02	30% exchange Fe@UiO-66-(COOH)$_2$	4.39	2.23	-		-	
HWI-A-006-01	66% exchange Fe@UiO-66-(COOH)$_2$	9.20	4.97	-		-	
HWI-A-008-01	80% exchange Fe@UiO-66-(COOH)$_2$	10.94	7.96	-		-	
HWI-A-004-01	30%-5% exchange Fe-Na@UiO-66-(COOH)$_2$	4.37	2.93	0.60	0.18	-	
HWI-A-009-01	80%-20% exchange Fe-Na@UiO-66-(COOH)$_2$	10.09	8.67	2.08	0.08	-	
HWI-A-005-01	30%-5% exchange Fe-K@UiO-66-(COOH)$_2$	4.35	2.83	-		1.02	0.13
HWI-A-010-01	80%-10% exchange Fe-K@UiO-66-(COOH)$_2$	10.12	8.67	-		1.77	0.06
HWI-A-007-01	80%-20% exchange Fe-K@UiO-66-(COOH)$_2$	9.95	8.32	-		3.48	0.16

4.4.3 N_2 adsorption/ desorption measurement

Figure 4.6 shows the N_2 adsorption/desorption isotherm profiles of chosen MOFs, while the textural property results are reported in Table 4.5.

The pore distribution estimated from BJH desorption branch ranges from 27.2 to 57.9 nm. Considering the classification of pores [17], the prepared Fe-based MOFs are mesoporous materials. The BET surface area increased from 6.46 to 15.13 m^2 g^{-1} by enhancing the amount of Fe exchange (from 30% to 80% cation exchange Fe@UiO-66-$(COOH)_2$, respectively). The introduction of Na further increased the BET surface area 17.67 m^2 g^{-1}, while the presence of K in the MOF materials decreased it.

However, the morphological and structural properties should be still improved as the metal exchange procedure worsened these properties with respect to the pristine UiO-66-$(COOH)_2$ [17]. A possible explanation can be ascribed to the synthesis conditions adopted, e.g. the long-time treatment in aqueous solution and the excess of metal salt remaining on the MOF surface. A further optimization of the metal exchange technique is needed to improve adsorption nitrogen performances of these MOF materials.

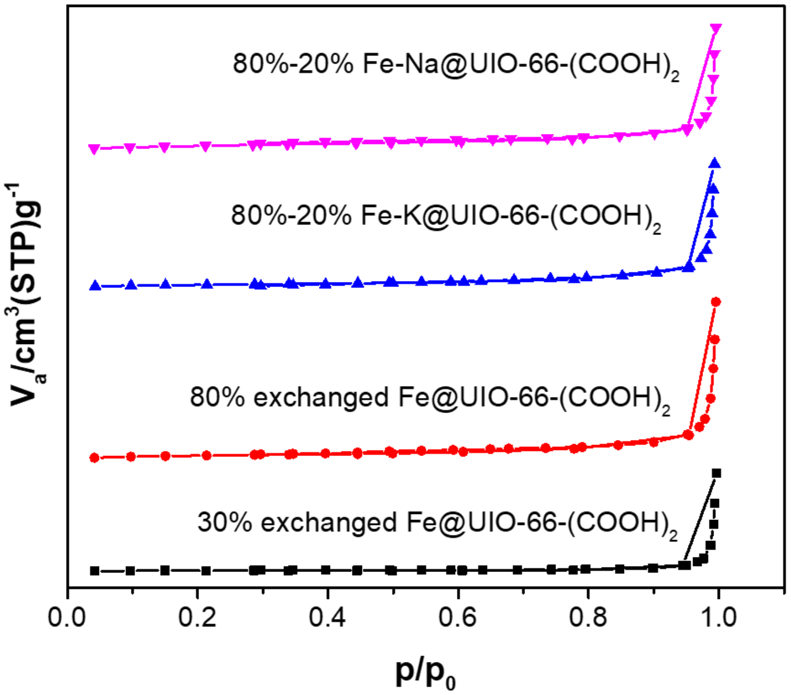

Figure 4.6 N_2 adsorption/ desorption isotherm of 30% cation exchange Fe@UiO-66-$(COOH)_2$, 80% cation exchange Fe@UiO-66-$(COOH)_2$, 80%-20% Fe-K@UiO-66-$(COOH)_2$ and 80%-20% Fe-Na@UiO-66-$(COOH)_2$.

Table 4.5 Textural properties of Fe-based UiO-66-$(COOH)_2$.

Sample	Description	S_{BET} (m^2g^{-1})	V_{pore} (cm^3g^{-1})	D_p (nm)
HWI-A-002-02	30% exchange Fe@UiO-66-$(COOH)_2$	6.46	0.094	57.9
HWI-A-008-01	80% exchange Fe@UiO-66-$(COOH)_2$	15.13	0.152	40.2
HWI-A-009-01	80%-10% exchange Fe-Na@UiO-66-$(COOH)_2$	17.67	0.120	27.2
HWI-A-007-01	80%-20% exchange Fe-K@UiO-66-$(COOH)_2$	10.53	0.125	47.4

4.5Electro-catalytic N_2 reduction in gas phase

4.5.1 Improved cell design.

Electrode and cell design plays an important role in electrochemical processes. For example, Giusi et al [20] recently observed that a gas flow-through device, having a particular electrode design with a nanomembrane catalytic layer crossed by a water-saturated reactant gas, allows to radically change performances with respect to conventional reactors using the same electrocatalytic materials. Even if in that case the application referred to CO_2 reduction rather than ammonia synthesis, the concept is that electrode design may strongly improve the formation of the desired product. Depending on the kind of electrocatalytic materials used, it is thus of great importance to find the right layer configuration of the electrode in order to maximize the electrocatalytic activity of this specific kind of material.

In this context, a rational design of the membrane electrode assembly was studied in detail for the case of Fe-based UiO-66-$(COOH)_2$ MOF materials. To find the optimal electrode configuration, the MOF materials were deposited and assembled in different ways:

i) in the middle between GDL and Nafion (1-Nafion/2-MOF/3-GDL);

ii) externally towards the gas phase (1-Nafion/2-GDL/3-MOF);

iii) in both sides of the GDL (1-Nafion/2-MOF/3-GDL/4-MOF).

The schematic views of the different membrane electrode assembly configurations are shown in Figure 4.7.

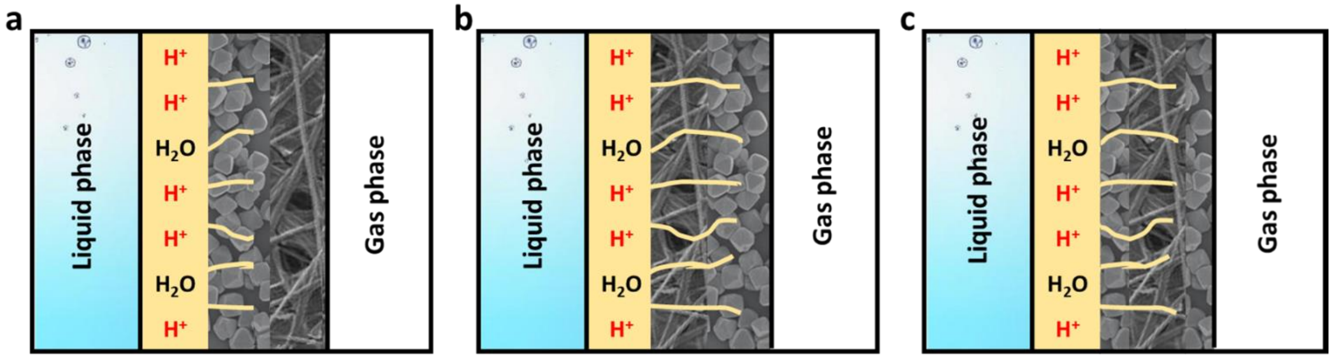

Figure 4.7 The different membrane electrode assembly configurations. (a)The catalyst deposited in the middle between GDL and Nafion (1-Nafion/2-MOF/3-GDL); (b) the catalyst towards the gas phase (1-Nafion/2-GDL/3-MOF); (c)The catalyst loaded on both side of GDL (1-Nafion/2-MOF/3-GDL/4-MOF).

Firstly, the catalyst was deposited in the middle between GDL and Nafion (see Figure 4.7 a). According to the working mechanism of the three-phase cell for NRR, water electrolysis occurs in the liquid cell (anode) and the hydrogen ions move to the gas phase cell (cathode) through the Nafion membrane and then combine with N_2 to form NH_3. The catalysts deposited in the middle between GDL and Nafion provides a full contact with Nafion membrane and electrolyte. Note that Nafion-MOF-GDL assembly was prepared by hot-pressing technique to guarantee a perfect adherence of the three layers. However, during the operations, a partial separation of Nafion membrane from MOFs@GDL occurred, with consequent decrease in NRR reactivity.

Then, Nafion/MOF/GDL/MOF the configuration with MOF-based catalyst deposited towards the gas phase was investigated (see Figure 4.7b). This layer configuration allowed to maximize nitrogen absorption due to rich porous structure of the MOF material, which is beneficial for the enrichment and diffusion of reactant nitrogen molecules [8]. The main advantage of Nafion/GDL/MOF configuration is that the Fe-MOFs catalysts was in intimate contact with the reactant nitrogen molecules, as shown in the scheme of Figure 4.7b. However, proton diffusion was more difficult in this configuration.

In order to overcome issues related to the application of these two configurations, the strategy was to deposit MOF materials on both the sides of the GDL, as shown in Figure 4.7c. Thus, Nafion-MOFs-GDL-MOFs electrode assembly allowed to balance the functions of reacting with hydrogen ions (limiting charge diffusion) and enrichment the reactant nitrogen (limiting gas diffusion). Note that the amount of catalyst deposited in the middle between GDL and Nafion was reduced to limit problems of adherence.

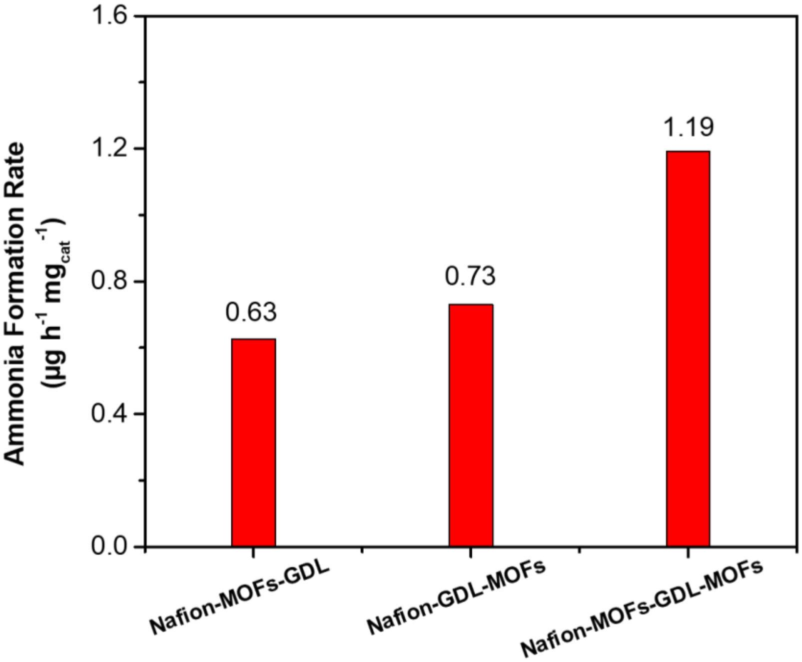

Figure 4.8 The average NH_3 formation rate of 80% cation exchange Fe@UiO-66-$(COOH)_2$ in 3 hours with different membrane electrode assembly configurations at -0.5 V vs. RHE in 0.5 M KOH.

These three types of electrode assembly configurations were tested in the three-phase compact reactor, with the procedure described in the previous chapter, at -0.5 V vs. RHE in 0.5 M KOH. The sample 80% cation exchange Fe@UiO-66-$(COOH)_2$ was chosen as the working electrode MOF material. Note that in the case of Nafion/MOF/GDL/MOF (MOF deposited on both the GDL sides), the total MOF loading was the same than the amount deposited on only one side for the other two configurations (Nafion/MOF/GDL and Nafion/GDL/MOF assembly). The ammonia absorber solution and electrolyte were sampled each hour during NRR testing and analysed by UV spectroscopic methods for the detection of ammonia, and the absorber and the liquid phase hemi-cell were filled with new solutions (0.001M H_2SO_4 and anolyte, respectively). The reaction lasted three hours and the overall NH_3 formation rate is shown in Figure 4.8.

The NH_3 yields are determined as 0.63, 0.73 and 1.19 μg h^{-1} mg_{cat}^{-2} with Nafion/MOF/GDL, Nafion/GDL/MOF and Nafion-MOF-GDL-MOF electrode assembly configurations, respectively. The electrode with the MOF loading on both the sides of the GDL showed a better stability and a higher yield to ammonia.

Thus, the Nafion-MOF-GDL-MOF electrode assembly configuration was adopted for the other experimental tests (see the scheme of the improved electrode and cell design in Figure 4.9).

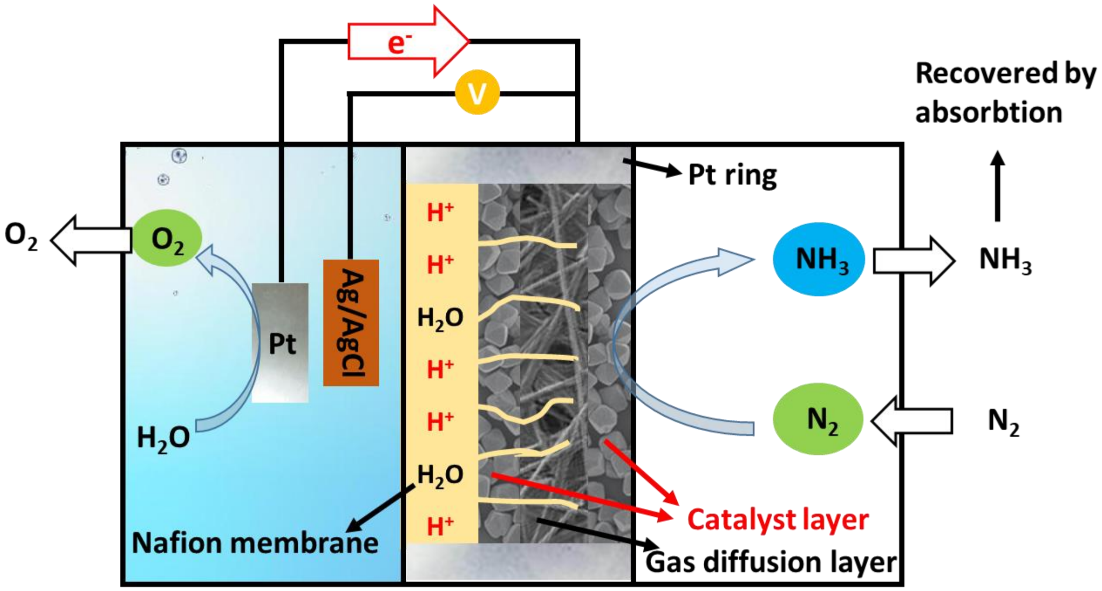

Figure 4.9 Schematic view of the improved flow-through reactor for electrochemical ammonia synthesis, with MOFs based catalysts.

4.5.2 The effect of applied voltage.

To explore suitable reaction conditions, initial electrocatalytic tests were made to evaluate the effect of the applied potential in the range from -0.1V to -0.6V vs. RHE, performed on 80% cation exchange Fe@UiO-66-$(COOH)_2$. The results are summarized in Figure 4.10.

At lower potential ($\leqslant$ -0.4 V vs RHE), the NH_3 formation rates were very low, in the range between 0.1 and 0.35 $\mu g \cdot h^{-1} \cdot mg_{cat}^{-1}$. Likewise, the values of Faraday efficiency calculated from ammonia yield and current were quite low and inaccurate.

Moreover, current density profiles (with 80% cation exchange Fe@UiO-66-$(COOH)_2$ as the working electrode) at low potentials ($\leqslant$ -0.4 V vs RHE) were quite lower, as shown in Figure 4.10b. It can be surmised that with the potential lower than -0.4 V vs RHE, the catalytic reaction cannot be active.

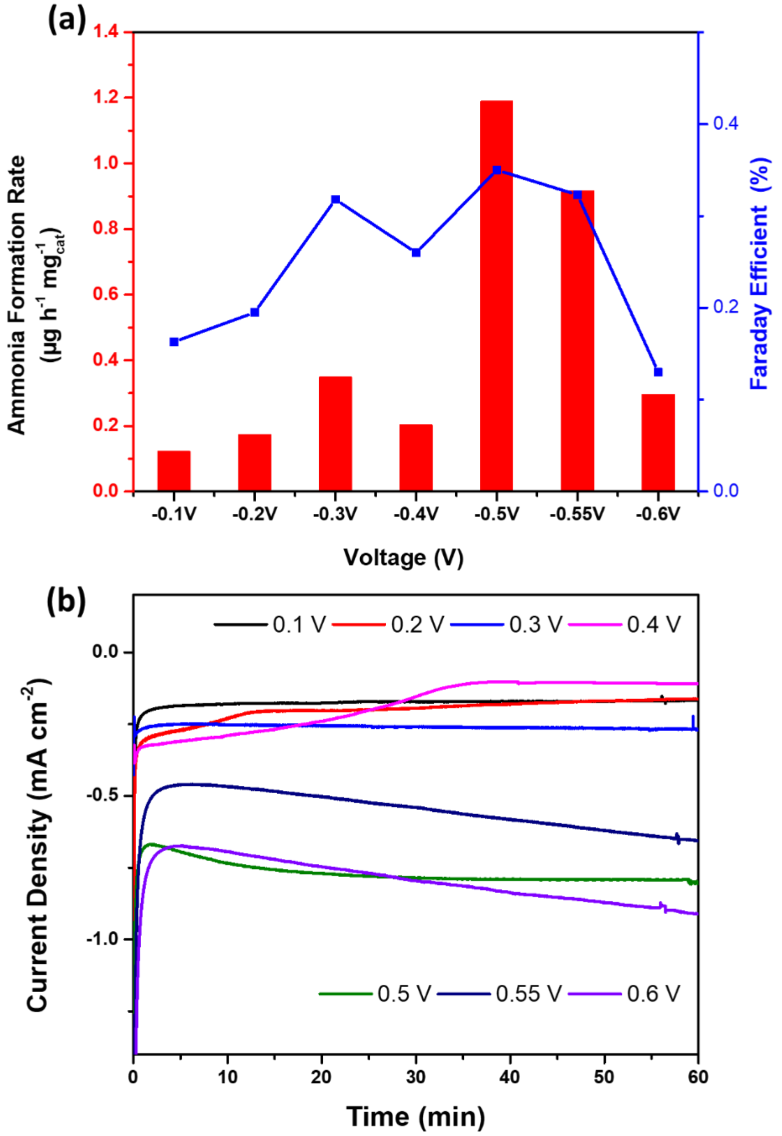

Figure 4.10 (a) NH_3 formation rate and Faradaic efficiency (b)Current density of 80% cation exchange Fe@UiO-66-$(COOH)_2$ at different potentials vs. RHE in 0.5M KOH.

At higher potential (⩾ -0.5 V vs RHE), a higher NH_3 formation rate was observed. As shown in Figure 4.10a, the best NH_3 formation rate was 1.19 μg· h^{-1}·mg_{cat}^{-1} at the applied voltage of -0.5 V vs RHE.

Moreover, in Figure 4.10b (reporting the current density as a function of time on stream reaction in 1 hour), the current densities of -0.77 mA cm^{-2}, -0.56 mA cm^{-2} and -0.80 mA cm^{-2} were obtained for the applied voltages of -0.5 V, -0.55 V and -0.60 V vs. RHE, respectively. Further tests were thus made at -0.5 V vs RHE.

4.5.3 Fe based UiO-66-$(COOH)_2$ in NRR

After the series of exploratory reactions described in the previous section, the optimal reaction conditions were confirmed as follows: The MOFs loaded on both the sides of the GDL and assembled in Nafion-MOF-GDL-MOF electrode configuration. The tests were performed using the compact gas-liquid-solid three-phase reactor at ambient pressure/temperature under an applied voltage of -0.5 V vs. RHE in 0.5 M KOH electrolyte.

The reactant N_2 (acting both as reactant and transport gas for generated ammonia) was continuously fed (20 mL/min of N_2 with purity, 99.9999%), and the flow coming out from the electrocatalytic reactor outlet (containing a mixture of N_2 and ammonia) was sent to a liquid absorber containing a 0.001 M H_2SO_4 solution. The amount of ammonia formed was monitored by a spectrophotometry method. The N_2 flow was introduced to the cathode part of the cell 30 min before the starting the reaction and then continuously fed till the end of the test. Further details were described in the previous chapter.

The following chosen samples:

- 30% cation exchange Fe@UiO-66-(COOH)$_2$,
- 80% cation exchange Fe@UiO-66-(COOH)$_2$,
- 80%-20% Fe-K@UiO-66-(COOH)$_2$,
- 80%-20% Fe-Na@UiO-66-(COOH)$_2$

were tested in the optimized gas-liquid-solid three-phase reactor for direct from N_2 and H_2O at ambient pressure/room temperature under an applied voltage of -0.5 V vs. RHE. The electrolyte in the anode was 0.5 M KOH solution, while the cathode operated in gas phase.

All the catalysts were tested for 4 hours and evidenced a constant and stable ammonia production rate (Figure 4.11). Their electrocatalytic performances are shown in Figure 4.12.

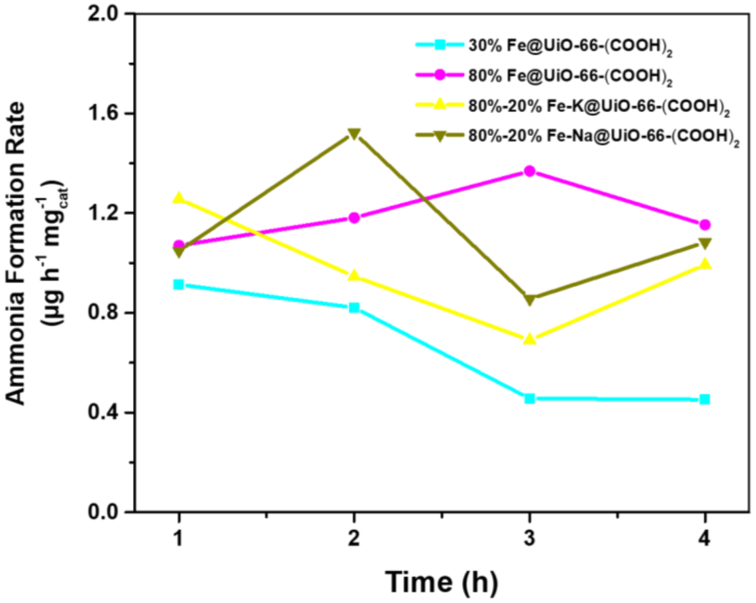

Figure 4.11 Ammonia formation rate in 4-hour test at -0.5 V vs RHE.

The ammonia in absorption solution and electrolyte were collected and tested in each hour. A stable current density of the first hour was shown in Figure 4.12a for all samples, indicating a stable behavior at this applied voltage.

The higher current density (in absolute value) was obtained by processing the sample with lower Fe exchange loading (30% Fe@UiO-66-(COOH)$_2$), providing an initial current density of -1.6 mA, then increasing (in negative) to about -2.3 mA (after about 1 h). The current density was lower for 80% Fe@UiO-66-(COOH)$_2$, and even more lower for 80%-20% Fe-Na@UiO-66-(COOH)$_2$ and 80%-20% Fe-K@UiO-66-(COOH)$_2$ samples.

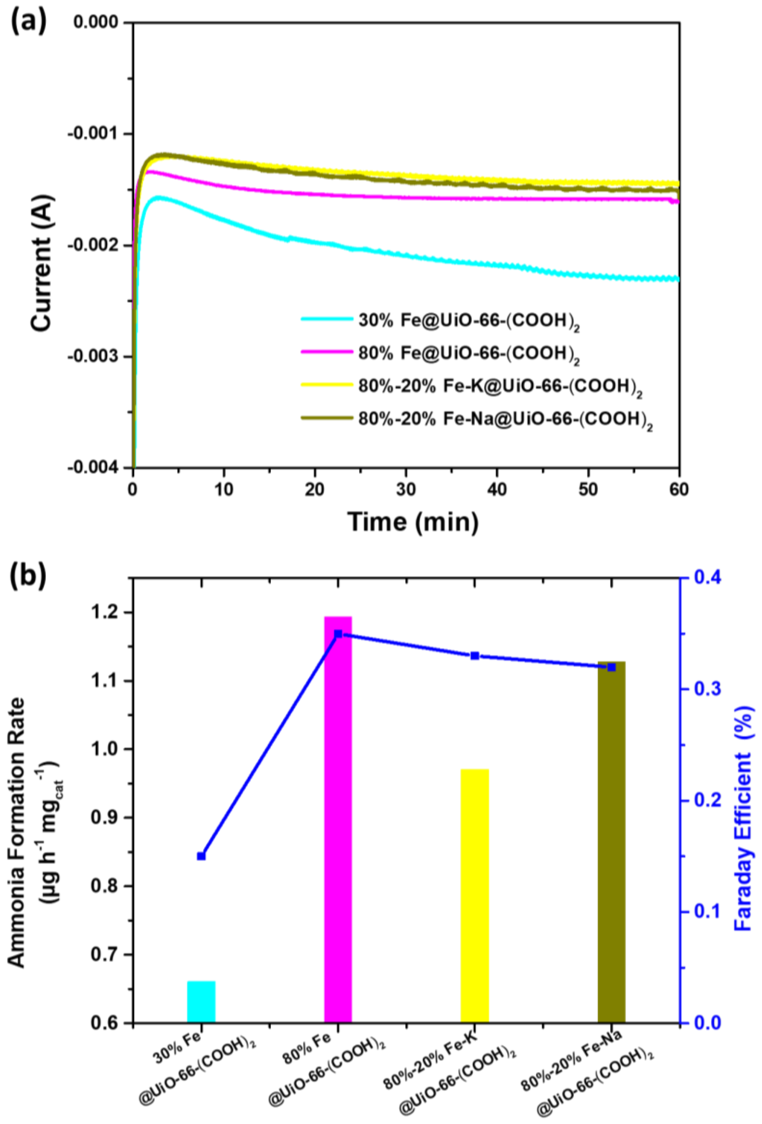

Figure 4.12 Electrocatalytic performances of 30% cation exchange Fe@UiO-66-(COOH)$_2$, 80% cation exchange Fe@UiO-66-(COOH)$_2$, 80%-20% Fe-K@UiO-66-(COOH)$_2$ and 80%-20% Fe-Na@UiO-66-(COOH)$_2$ (a) current in the first hour; (b) the Faraday Efficiency and average ammonia formation rate at -0.5 V vs RHE in 4 hour test.

However, the highest ammonia formation rate (1.193 μg· h^{-1}· mg_{cat}^{-1}) at the applied voltage of -0.5 V vs. RHE was provided by the 80% Fe@UiO-66-$(COOH)_2$ (see Figure 4.12b), with a best FE of 0.35%.

The catalytic performance of 80%-20% Fe-Na@UiO-66-$(COOH)_2$ was similar to that of 80% Fe@UiO-66-$(COOH)_2$, with a yield of 1.128 μg· h^{-1}· mg_{cat}^{-1} and a FE of 0.32%. Considering the actual Na^+ content in 80%-20% Fe-K@UiO-66-$(COOH)_2$ was quite lower (0.08 wt %), the effect of introduced Na^+ could be neglected. The NH_3 yields are determined as 0.661 and 0.971 μg· h^{-1}· mg_{cat}^{-1} with 30% Fe@UiO-66-$(COOH)_2$ and 80%-20% Fe-K@UiO-66-$(COOH)_2$ as catalyst, respectively.

In order to improve understanding of the relationship between structure and activity, a linear trend (shown in Figure 4.12) was observed between the rate of ammonia formation in the Fe based MOF samples reported in Figure 4.7 and S_{BET} (m^2 g^{-1}) as detected by N_2 adsorption/ desorption isotherm (Table 4.5), suggesting a relationship between these two aspects. The Fe based MOF with higher specific surface area shows a better NRR activity. Meanwhile, a higher iron content exhibited better catalytic activity. Based on the above results, the synthesis and processing procedure of Fe based MOFs still needs to be improved and optimized. This UiO-66-$(COOH)_2$ based MOFs was temperature-sensitive. If this MOF was desorbed at too low temperature, the molecules would be entrapped in the structure. If the MOF was desorbed at too high temperature, the structure would be destroyed and make anhydrides from two carboxylic acids.

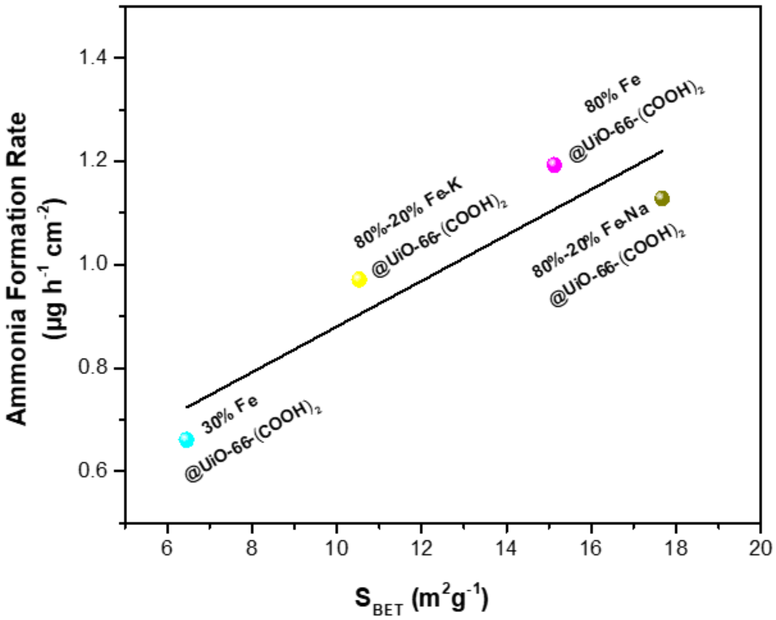

Figure 4.13 A liner trend between ammonia formation rate at −0.5 V vs. RHE and S_{BET} (m^2 g^{-1}) as detected by N_2 adsorption/ desorption isotherm.

A brief overview from literature about the NH_3 electrosynthesis activity for Fe-based or MOF-based catalysts is reported in Table 4.6. Up to now, no specific works on the use of Fe-based MOFs as cathode catalysts in the electrochemical synthesis of ammonia at low temperature have been reported. Moreover, the operating conditions are quite different from those we adopted in this PhD work, especially the reactor and electrode configuration; thus, it is hard to make comparison of performances in NRR. However, our preliminary exploration indicates that the prepared MOFs are promising in NRR as they are quite active, but further work is needed to improve the yield and efficiency to ammonia.

Table 4.6 Comparison with state-of-the-art representative electrocatalysts in NRR.

Composition (*)	FE (%)	NH_3 Formation rate	Potential applied (V) and electrolyte	Conditions	Ref.
80% Fe@UiO-66-$(COOH)_2$	0.35	$1.19\ \mu g\cdot h^{-1}\cdot mg_{cat}^{-1}$	-0.5 vs RHE 0.5 M KOH	Room temperature	This work
Fe_2O_3-CNTs	0.15	$0.22\ \mu g\cdot h^{-1}\cdot mg_{cat}^{-1}$	-2.0 vs Ag/AgCl diluted $KHCO_3$	Room temperature	[24]
Fe_2O_3/CNT 3h activated in situ	17.0	$41.6\ \mu g\cdot h^{-1}\cdot mg_{cat}^{-1}$	-0.5 vs RHE 0.5 M KOH	Room temperature	[25]
Fe-based MIL-100	22.2	$1.31\ \mu g\cdot h^{-1}\cdot mg_{cat}^{-1}$	-1.2 vs Ag/AgCl 2 M KOH	90°C	[9]
Ag-Au@ZIF	18 ± 4	$0.61\ \mu g\cdot h^{-1}\cdot cm^{-2}$	-2.9 vs Ag/AgCl THF-solution containing LiTf	25°C	[10]
Zero-dimensional NiFe-MOF	11	$9.3\ \mu g\cdot h^{-1}\cdot mg_{cat}^{-1}$	-0.345 mVvs RHE 0.1 M $NaHCO_3$	Room temperature	[11]
N-doped carbon from ZIF-8 pyrolysis	10.2	$72.25\ \mu g\cdot h^{-1}\cdot mg_{cat}^{-1}$	-0.3 vs RHE 0.1 M KOH	Room temperature	[13]
Ru Single-Atom Ru@ZrO_2/NC	15	$3.665\ mg\cdot h^{-1}\cdot mg_{Ru}^{-1}$	-0.21 vs RHE 0.1 M HCl	Room temperature	[14]

4.6 Conclusions

In this chapter, a series of improved Fe-based and Fe-alkali metal-based MOF UiO-66-$(COOH)_2$ were synthesized by cation exchange reaction technique. Present data evidence that 80% cation exchange Fe@UiO-66-$(COOH)_2$ (with an actual Fe content of 7.96 wt %) is the best electrocatalyst among iron based MOF catalysts. The performances highly depend on the cell design, a Nafion-MOFs-GDL-MOFs type electrode assembly was developed which allowed to balance the functions of reacting with protons(limiting charge diffusion) and enrichment the reactant nitrogen (limiting gas diffusion). The effect of applied voltage were observed, a good activity and stability were found for an applied voltage at -0.5 V vs. RHE. From the catalytic test with different Fe based MOF catalysts, the material with higher specific surface area shows a better NRR activity. Therefore, optimizing the catalysts synthesis steps to obtain a higher specific surface area is required in further research.

Moreover, as currently used in the industrial catalysts for Haber-Bosh process, the introduction of potassium in the electrocatalysts was also investigated, in order to facilitate charge transfer from K^- ions to the iron-based catalyst surface, balancing the dissociative chemisorption between H_2 and N_2, and suppressing side reactions, thus improving both activity and stability. These results were very promising, although a further experimentation is needed to improve their performances in NRR, to overcome limitations related to MOF materials themselves, majorly due to their low conductivity and stability.

4.7 Connected Experimental Section

X-ray Powder Diffraction (XRD). X-ray Powder Diffraction (XRD) is a rapid and widely used analytical technique, which can provide information about composition from details of phases present in the sample, lattice parameter, crystal structure, (hkl) parameters, crystalline size (estimated from Scherrer equation) and so on [21].

When a sample is irradiated by X-rays with certain wavelength and at certain incident angles, intense reflected X-rays are produced when the wavelengths of the scattered X-rays interfere constructively. This phenomenon can be summarized in the Bragg's Law. The diffraction peaks including positions and intensities provide information of the sample.

In this work, XRD measurements were carried out on a Bruker D-8 Advance diffractometer with a Lynx-Eye detector (Cu Kα radiation) in the 10-100° (2θ) range with a scan step of 0.020°, step time 0.1s. The characteristic incident X-ray by Cu radiation was 1.5418 Å.

Inductively Coupled Plasma with Optical Emission Spectrometry (ICP-OES). Inductively Coupled Plasma (ICP) is one method of optical emission spectrometry. When plasma energy is given to an analysis sample from outside, the component elements (atoms) are excited. When the excited atoms return to low energy position, emission rays (spectrum rays) are released and the emission rays that correspond to the photon wavelength are measured. The element type is determined by the position of the photon rays, while the content of each element is determined by the rays' intensity [22].

To generate plasma, first, argon gas is supplied to torch coil, and high frequency electric current is applied to the work coil at the tip of the torch tube. Using the electromagnetic field created in the torch tube by the high frequency current, argon gas is ionized and plasma is generated. This plasma has high electron density and temperature (10000 K) and this energy is used in the excitation-emission of the sample. Solution samples are introduced into the plasma in an atomized state through the narrow tube in the center of the torch tube.

In this research, ICP-OES analysis was performed under inert atmosphere at the Mikroanalytisches Labor Pascher (Remagen, Germany) using an Activa from Jobin Yvon.

N_2 adsorption/desorption measurement. The textural properties of material can be measure by N_2 adsorption/desorption method. It can give the information of specific surface area, pore volume and pore distribution, which is of great significance for the catalyst characterization. For example, a higher surface area provides more possibility for the contact of reactants with the catalyst. Molecular sieve is employed in gas separation process based on pore size and dynamic diameter of molecular gas. The pores in porous materials can be classified into: i) micropore (< 2nm), such as zeolite, activated carbon, metal organic framework, ii) mesopore (2-50 nm), such as mesoporous silica, activated carbon and iii) macropore (> 50 nm), such as sintered metals and ceramics according to the pore size [23].

N_2 isotherms at 77K were performed using a BELSORP-mini apparatus (BELJapan). Specific surface area was calculated by Brunauer– Emmet– Teller (BET) method. Pore volume was determined by Barrett- Joyner- Halenda (BJH) method. Pore distribution were determined using desorption branch by BJH method. The samples were outgassed under vacuum (≈10-4 mbar) at 80°C for 12h before starting the measurements.

4.8 References

[1] Wang, H.; Zhu, Q.-L.; Zou, R.; Xu, Q. J. C., Metal-organic frameworks for energy applications. Chem 2017, 2 (1), 52-80.

[2] Xie, S.; Ye, J.; Yuan, Y.; Chai, Y.; Yuan, R., A multifunctional hemin@ metal-organic framework and its application to construct an electrochemical aptasensor for thrombin detection. *Nanoscale* **2015,** *7* (43), 18232-18238.

[3] Yamada, T.; Shiraishi, K.; Kitagawa, H.; Kimizuka, N., Applicability of MIL-101 (Fe) as a cathode of lithium ion batteries. *Chemical Communications* **2017,** *53* (58), 8215-8218.

[4] Sun, H.; Yu, X.; Ma, X.; Yang, X.; Lin, M.; Ge, M., MnO$_x$-CeO$_2$ catalyst derived from metal-organic frameworks for toluene oxidation. *Catalysis Today* **2019**.

[5] Li, J.-R.; Kuppler, R. J.; Zhou, H.-C., Selective gas adsorption and separation in metal-organic frameworks. *Chemical Society Reviews* **2009,** *38* (5), 1477-1504.

[6] Lazaro, I. A.; Forgan, R. S., Application of zirconium MOFs in drug delivery and biomedicine. *Coordination Chemistry Reviews* **2019,** *380*, 230-259.

[7] Agostoni, V.; Horcajada, P.; Noiray, M.; Malanga, M.; Aykaç, A.; Jicsinszky, L.; Vargas-Berenguel, A.; Semiramoth, N.; Daoud-Mahammed, S.; Nicolas, V., A “green” strategy to construct non-covalent, stable and bioactive coatings on porous MOF nanoparticles. *Scientific reports* **2015,** *5* (1), 1-7.

[8] He, K.; Li, Z.; Wang, L.; Fu, Y.; Quan, H.; Li, Y.; Wang, X.; Gunasekaran, S.; Xu, X., A water-stable luminescent metal-organic framework for rapid and visible sensing of organophosphorus pesticides. *ACS applied materials interfaces* **2019,** *11* (29), 26250-26260.

[9] Zhao, X.; Yin, F.; Liu, N.; Li, G.; Fan, T.; Chen, B. J. J. o. M. S., Highly efficient metal–organic-framework catalysts for electrochemical synthesis of ammonia from N$_2$ (air) and water at low temperature and ambient pressure. Journal of Materials Science 2017, 52 (17), 10175-10185.

[10] Lee, H. K.; Koh, C. S. L.; Lee, Y. H.; Liu, C.; Phang, I. Y.; Han, X.; Tsung, C.-K.; Ling, X. Y. J. S. a., Favoring the unfavored: selective

electrochemical nitrogen fixation using a reticular chemistry approach. Science advances 2018, 4 (3), eaar3208.

[11] Duan, J.; Sun, Y.; Chen, S.; Chen, X.; Zhao, C., A zero-dimensional nickel, iron–metal–organic framework (MOF) for synergistic N_2 electrofixation. *Journal of Materials Chemistry A* **2020,** *8* (36), 18810-18815.

[12] Das, R.; Pachfule, P.; Banerjee, R.; Poddar, P. J. N., Metal and metal oxide nanoparticle synthesis from metal organic frameworks (MOFs): finding the border of metal and metal oxides. Nanoscale 2012, 4 (2), 591-599.

[13] Mukherjee, S.; Cullen, D. A.; Karakalos, S.; Liu, K.; Zhang, H.; Zhao, S.; Xu, H.; More, K. L.; Wang, G.; Wu, G. J. N. E., Metal-organic framework-derived nitrogen-doped highly disordered carbon for electrochemical ammonia synthesis using N_2 and H_2O in alkaline electrolytes. Nano Energy 2018, 48, 217-226.

[14] Tao, H.; Choi, C.; Ding, L.-X.; Jiang, Z.; Han, Z.; Jia, M.; Fan, Q.; Gao, Y.; Wang, H.; Robertson, A. W., Nitrogen fixation by Ru single-atom electrocatalytic reduction. *Chem* **2019,** *5* (1), 204-214.

[15] Yan, P.; Guo, W.; Liang, Z.; Meng, W.; Yin, Z.; Li, S.; Li, M.; Zhang, M.; Yan, J.; Xiao, D., Highly efficient K-Fe/C catalysts derived from metal-organic frameworks towards ammonia synthesis. *Nano Research* **2019,** *12* (9), 2341-2347.

[16] Cavka, J. H.; Jakobsen, S.; Olsbye, U.; Guillou, N.; Lamberti, C.; Bordiga, S.; Lillerud, K. P. J. J. o. t. A. C. S., A new zirconium inorganic

building brick forming metal organic frameworks with exceptional stability. Journal of the American Chemical Society 2008, 130 (42), 13850-13851.

[17] Ragon, F.; Campo, B.; Yang, Q.; Martineau, C.; Wiersum, A. D.; Lago, A.; Guillerm, V.; Hemsley, C.; Eubank, J. F.; Vishnuvarthan, M. J. J. o. M. C. A., Acid-functionalized UiO-66 (Zr) MOFs and their evolution after intra-framework cross-linking: structural features and sorption properties. *Journal of Materials Chemistry A* **2015**, 3 (7), 3294-3309.

[18] Vanessa Meyer, 2018. Steigerung der ammoniakabsorptionskapazitat von Zr-UiO-$(COOH)_2$ (BCU) durch die einlagerung von ubergangsmetallione. Christian-Albrechts-Universität zu Kiel, Kiel, Germany.

[19] Sing, K. S. J. P.; chemistry, a., Reporting physisorption data for gas/solid systems with special reference to the determination of surface area and porosity (Recommendations 1984). *Pure and applied chemistry* **1985**, 57 (4), 603-619.

[20] Giusi, D.; Ampelli, C.; Genovese, C.; Perathoner, S.; Centi, G., A novel gas flow-through photocatalytic reactor based on copper-functionalized nanomembranes for the photoreduction of CO_2 to C1-C2 carboxylic acids and C1-C3 alcohols. *Chemical Engineering Journal* **2020**, 127250.

[21] Thamaphat, K.; Limsuwan, P.; Ngotawornchai, B., Phase characterization of TiO_2 powder by XRD and TEM. *Kasetsart J.* **2008,** *42* (5), 357-361.

[22] Olesik, J. W., Elemental analysis using ICP-OES and ICP/MS. *Analytical Chemistry* **1991,** *63* (1), 12A-21A.

[23] Sing, K. S., Reporting physisorption data for gas/solid systems with special reference to the determination of surface area and porosity (Recommendations 1984). *Pure applied chemistry* **1985,** *57* (4), 603-619.

[24] Chen, S.; Perathoner, S.; Ampelli, C.; Mebrahtu, C.; Su, D.; Centi, G., Electrocatalytic synthesis of ammonia at room temperature and atmospheric pressure from water and nitrogen on a carbon-nanotube-based electrocatalyst. *Angewandte Chemie International Edition* **2017,** *56* (10), 2699-2703.

[25] Chen, S.; Perathoner, S.; Ampelli, C.; Wei, H.; Abate, S.; Zhang, B.; Centi, G., Enhanced performance in the direct electrocatalytic synthesis of ammonia from N_2 and H_2O by an in-situ electrochemical activation of CNT-supported iron oxide nanoparticles. *Journal of Energy Chemistry* **2020,** *49*, 22-32.

5 Efficient Electrocatalytic N_2 Reduction reaction with Alkalized Ti_3C_2 MXene nanoribbons.

5.1 Introduction

MXenes are metal carbide or nitride materials with a two-dimensional (2D) structure, which have recently attracted a large interest for a broad range of applications such as materials for energy and environmental applications [1] [2], and catalysis[3] [4].In the latter area, several papers deal on N_2 fixation (NRR) [5], a topic of current large interest to directly produce ammonia from nitrogen[6]. MXene presents the unusual electronic property of the 2D structure and also the unique property of transition metal carbides, such as metallic conductivity, and the hydrophilic nature of their hydroxyl or oxygen terminated surfaces. For these properties there is a large interest on the use of MXenes as novel NRR electrocatalysts, as emerges also from the state-of-the-art comparison of NRR electrocatalysts. They have properties well comparable with those of the best reported NRR electrocatalysts, with the advantage of a flexible way to tune further their properties, and thus a large potential for further improvement.

Most of studies on MXenes as electrocatalysts for NRR indicated the need to have a 2D nanostructure, with the activity in N_2 fixation attributed generally to edge sites of the nanosheets. Luo et al.[7], for example, indicate the middle Ti at the edge sites as the active sites for NRR. The mechanism proposed involved hydrogenation of undissociated N_2 molecules. Gouveia et al. [8] considered instead that N_2 dissociation occurs easily on the MXene (0001) surface. The top site above the metal ions on the surface of MXene nanosheets was also indicated by Wang et al.[9] as the sites for end-on adsorption of N_2, which is then hydrogenated, rather than dissociated.

Johnson et al.[10] indicated that edge sites of MXene are involved in NRR reaction and that F functional groups enhance the NRR performance in comparison to O functional groups. Xia et al., [11] on the contrary, indicated that exposed Ti sites in Ti_3C_2OH facilitate the electron transfer and promote the adsorption and activation of dinitrogen. Guo et al. [12] suggested that OH terminal groups of MXene are inactive, indicating thus that a modification of the surface chemical states by introducing Fe heteroatoms is necessary to increase the activity.

Most of the studies based their conclusions mainly on theoretical modelling. However, notwithstanding the discordances in the nature of the active MXene materials for NRR reaction, a common agreement is that a 2D configuration is needed.

2D-type materials are an area of intense research interest for a number of applications in the field of materials for energy, including catalysis [13]. On the other hand, it is possible to assemble and master 2D materials to form other type of 3D-like nanomaterials [14]. MXenes nanosheets can be subjected to a transformation from a 2D to a 3D-like nanostructures [15]. This will allow to clarify the relationship between performances and type of nanostructure. In the specific case of NRR, this method of manipulating nanostructures allows to understand the role and relevance of the presence of a 2D nanostructure on edge or planar bases, by comparing the behaviour of very analogous materials but with different nanoshapes.

5.2 Scope of the chapter

In the previous chapters, the use of MOF materials for the preparation/assembling of efficient electrodes for the process of nitrogen reduction reaction (NRR) was explored. Although the electrodes showed some electrocatalytic activity and results are very promising, further studies are needed in terms of electrode design to overcome limitations related to MOF materials themselves, majorly due to their low conductivity and stability. However, to increase performances in NRR and to show the potentiality of the compact homemade three-phase electrocatalytic device, a more efficient class of materials are needed.

In this view, this chapter is dedicated to the exploration of MXene advanced materials and to the tentative of synthesizing a 3D nanoarchitecture starting from 2D-dimensional MXene-based catalysts. To understand the role of the nanostructure of MXene materials in NRR, Ti_3C_2 nanosheets were treated with KOH to obtain a final shape of three-dimensional (3D) porous frameworks nanoribbons. The specific objective of this chapter is to investigate how the conversion of Ti_3C_2 nanosheets to 3D-like nanoribbons influence the NRR reactivity in the three-phase electrochemical cell. A full characterization of Mxenes nanoribbons (SEM, TEM, HRTEM, XRD, XPS and EDX) was also presented.

The results presented in this chapter have been published in *ChemSusChem* 2020, **13**, 5614–5619 DOI: 10.1002/cssc.202001719 [16].

5.2 Material and Methods

5.2.1 Synthesis of Ti_3C_2 MXene nanosheets and nanoribbons

Ti_3C_2 MXene nanosheets. To synthesize Ti_3C_2 MXene nanosheets (MNSs), 5 g of Ti_3AlC_2 starting precursor were etched by 120 mL of 40% HF at 50°C for 72 h under stirring. Then, the suspension was washed and centrifugated by deionized water until pH>6, followed by vacuum drying at 60°C overnight to obtain Ti_3C_2 MXene nanosheets.

Ti_3C_2 MXene nanoribbons. 0.5 g MNSs powder was then treated with 60 mL of 6 M KOH for 72 h under Ar atmosphere to avoid the oxidation by oxygen, followed by steps as above. Ti_3C_2 MXene nanoribbons (MNRs) are obtained in this way. The method of preparation is analogous to that used by Lian et al [17].

5.2.2 Preparation of the membrane electrode

Preparation of the catalyst on Gas diffusion layer. 8 mg of the electrocatalyst was suspended in 5 mL of ethanol and 50 μL of 10 wt% Nafion solution. The solution was sonicated for 90 min to obtain a homogeneous mixture, which was deposited by spray drying onto a gas-diffusion layer (GDL), and then dried at 80^oC overnight.

Nafion membrane pretreatment. A commercial Nafion® 115 membrane was cut into small pieces and treated with 3 wt. % H_2O_2 water solution for 1 hour at 80 ^oC. Then, the pieces of membrane were treated in 0.5 M H_2SO_4 solution for 1 hour at 80 ^oC under stirring, followed by rinsing until neutral pH. Finally, the obtained Nafion was kept in deionized water.

Membrane electrode assembly. The GDL (after depositing the catalyst) and the pretreated Nafion membrane were hot pressed together at 80 atm and 130 ^oC for 90 s. The active catalytic material was located between these two layers. The loading amount was 0.2 mg cm^{-2} and size of the electrodes was 2 cm^2.

5.2.3 Reaction conditions and calculations

All the electrochemical measurements on MXene materials were carried out in a three-phase reactor, working in gas phase. The liquid anode chamber contained a liquid electrolyte (the anolyte) for oxygen evolution reaction (OER) also generating the protons and electrons, which moved towards the cathode where they were used in the solid membrane (gas-diffusion) electrode for NRR. Schematic view of the improved design in the three-phase reactor for electrochemical ammonia synthesis is shown in Figure 5.1.

The solid zone consisted of a Nafion membrane, a catalyst layer and a gas diffusion layer. The reactant N_2 was continuously fed (20 mL min^{-1} of N_2 with purity 99.99%) to the cathode gas side. The amount of ammonia formed was monitored by a spectrophotometry method, as described in the previous chapter. Both the solution in the cathode output absorber and the anode electrolyte were analysed to measure the total ammonia/ammonium production. The N_2 flow was introduced to the cathode part of the cell 30 min before starting the reaction and then continuously fed till the end of the test. A potentiostat /galvanostat (AMEL 2551) provided the working potential. A Pt rod was used as the counter electrode. All the potentials were measured against Ag/AgCl reference electrode (3 M KCl). The Fe-MOF loaded on the gas diffusion layer was used as the working electrode.

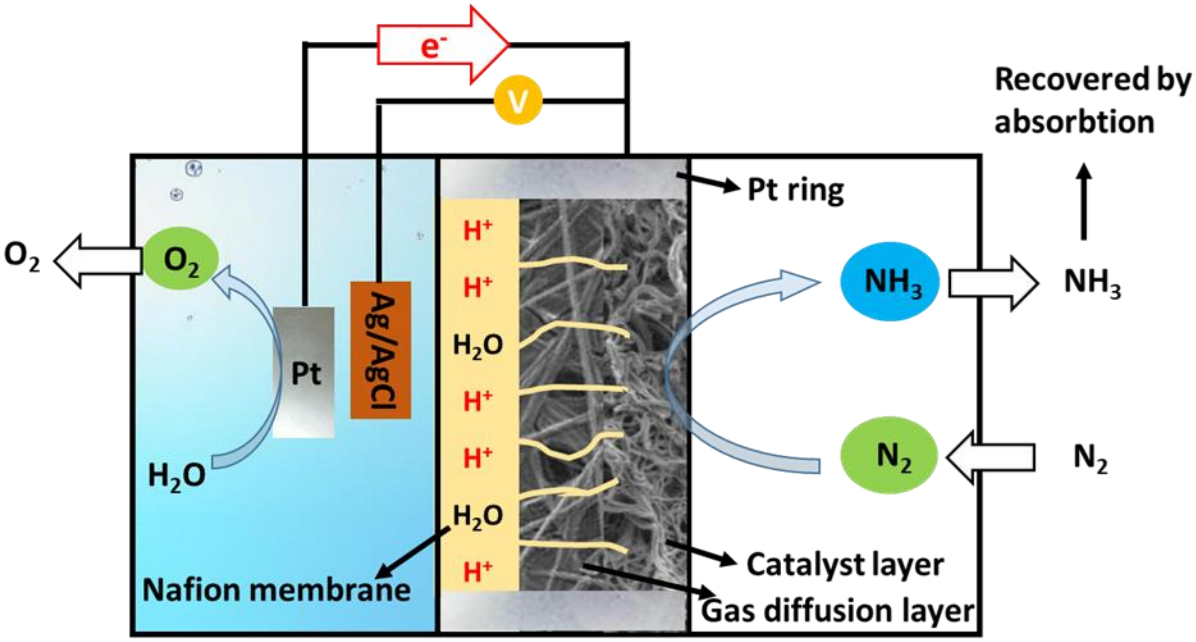

Figure 5.1 Schematic view of the three-phase reactor for electrochemical ammonia synthesis with MXene materials.

5.3 Characterization

5.3.1 Crystalline phase and morphology: SEM, TEM and XRD

The scanning electron microscopy (SEM) images (Figure 5.2 a) for $Ti_3C_2T_x$ (where T=F, OH) after the HF etching, show a MXene loosely layered 2D structure, indicating the successful exfoliation of Al from the MAX phase (Ti_3C_2Al). The transparency of the nanosheet presented in Figure 5.2 b suggests the likely presence of a single layer sheet [19]. It presents a monocrystal as shown by diffraction pots of the selected area electron diffraction (SAED) reported in the inset of Figure 5.2 b. The HRTEM image (Figure 5.2 c) shows the interlayer spacing of 1.00 nm corresponding to the (002) plane [19], which is consistent with the value measured by XRD and with results obtained by Ghidiu et al [20]. After Ti_3C_2 nanosheets treatment by KOH, nanoribbons could be well evidenced (Figure 5.4 d). The nanoribbons have a diameter around 16 nm, in agreement also with HRTEM images (Figure 5.2 e and f).

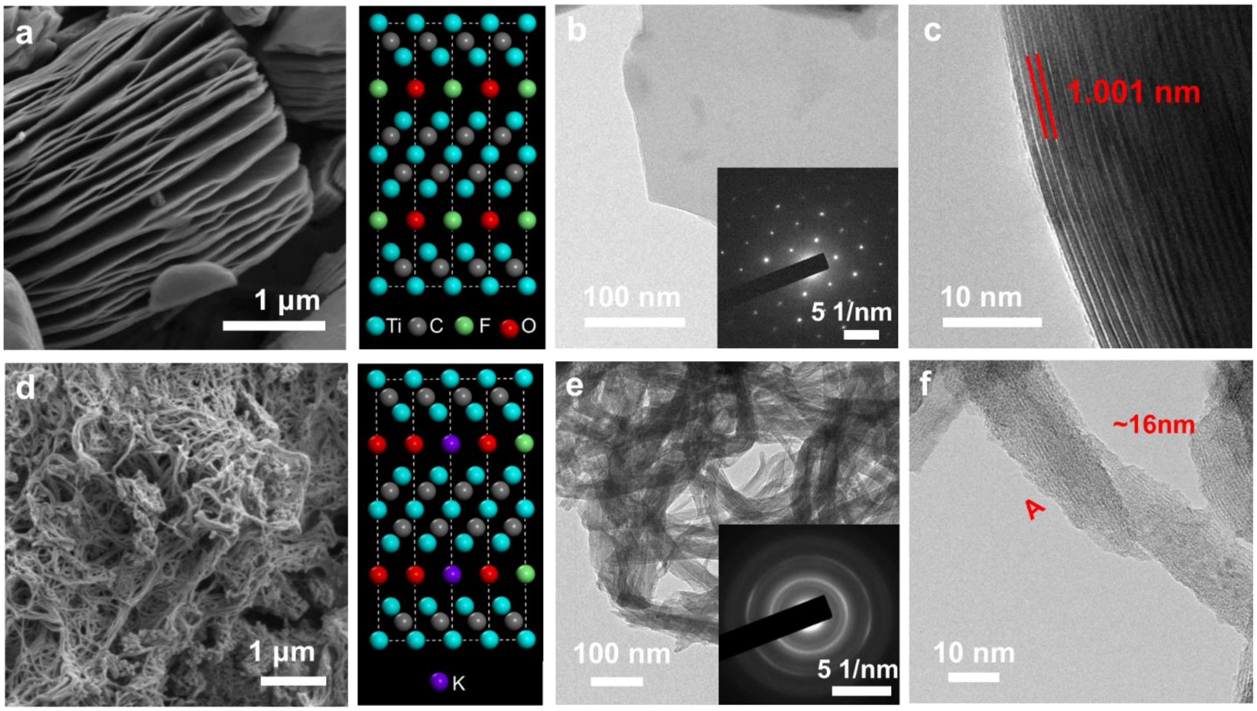

Figure 5.2 (a) SEM image and structural model of Ti_3C_2 MNSs (b) Top-view TEM image and electron diffraction pattern of Ti_3C_2 MNSs. (c) Cross-sectional TEM image of Ti_3C_2 MNSs. d) SEM image and structural model of Ti_3C_2 MNRs. (e) TEM image of Ti_3C_2 MNRs and electron diffraction pattern of Ti_3C_2 MNRs. (f) HRTEM image of Ti_3C_2 MNRs, a single MNR with a width of ~16 nm, taken from position A.

The conversion of Ti_3AlC_2 (MAX phase) to Ti_3C_2 MNSs and MNRs is confirmed by X-ray diffraction (XRD) (Figure 5.3). Compared with the pattern of Ti_3AlC_2, the most intense peak (104) of Ti_3AlC_2 disappears and the (002) reflection of MXene shifts from 9.7° to 9.1° broadening at the same time. This is consistent with the expected interlayer spacing expansion in passing from Ti_3AlC_2 to Ti_3C_2 MNSs [21]. When the Ti_3C_2 MNSs is further treated in KOH solution, the (002) reflection shifts to 7.1° and further broaden, consistently with the further expansion of interlayer spacing [17].

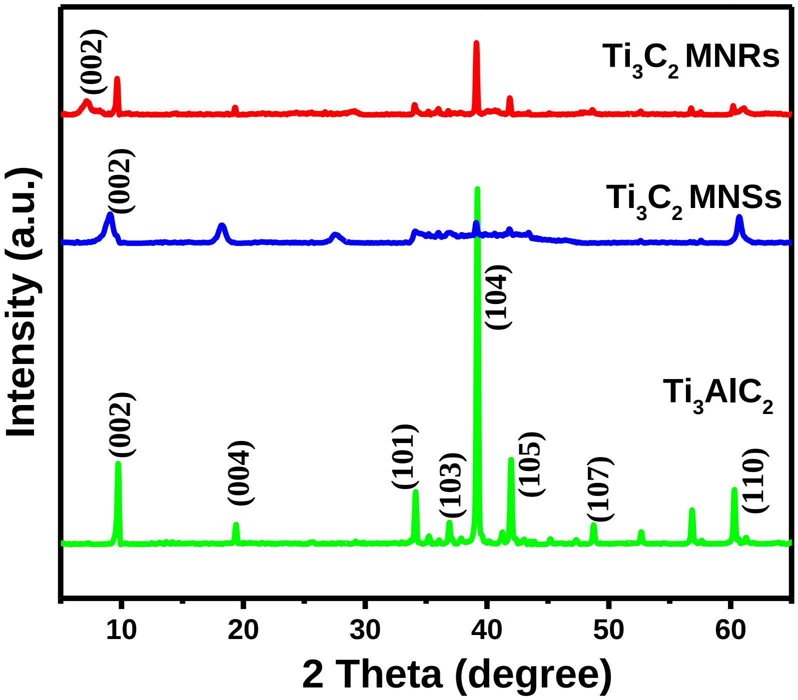

Figure 5.3 XRD patterns of Ti_3C_2 MNRs, Ti_3C_2 MNSs, and pristine Ti_3AlC_2.

5.3.2 Surface Analysis: XPS and EDX

The full spectrum X-ray photoelectron spectroscopy (XPS) and associated elemental analysis (Figure 5.4 a) confirm the existence of C, K, O and F in Ti_3C_2 MNRs.

It also evidenced the large enhancement of the O content which becomes over twice the initial value after the KOH treatment, indicating that the nanoribbon edges are rich in OH groups. In the C 1s region (Figure 5.4 b), the characteristic peaks of K $2p_{3/2}$ at 292.4 eV and K $2p_{1/2}$ at 295.2 eV are present only in Ti_3C_2 MNRs, but K presence was not detected in Ti_3C_2 MNSs neither in Ti_3AlC_2. This is consistent with XPS elemental analysis (Figure 5.5 c). This accounts for the alkalization of MNRs, consistent with XRD measurement. However, the K atoms do not enter in the Ti_3C_2 MNRs structure to occupy the anion sites, as confirmed by analysis of the lattice spacing of (002) plane in XRD diffractograms.

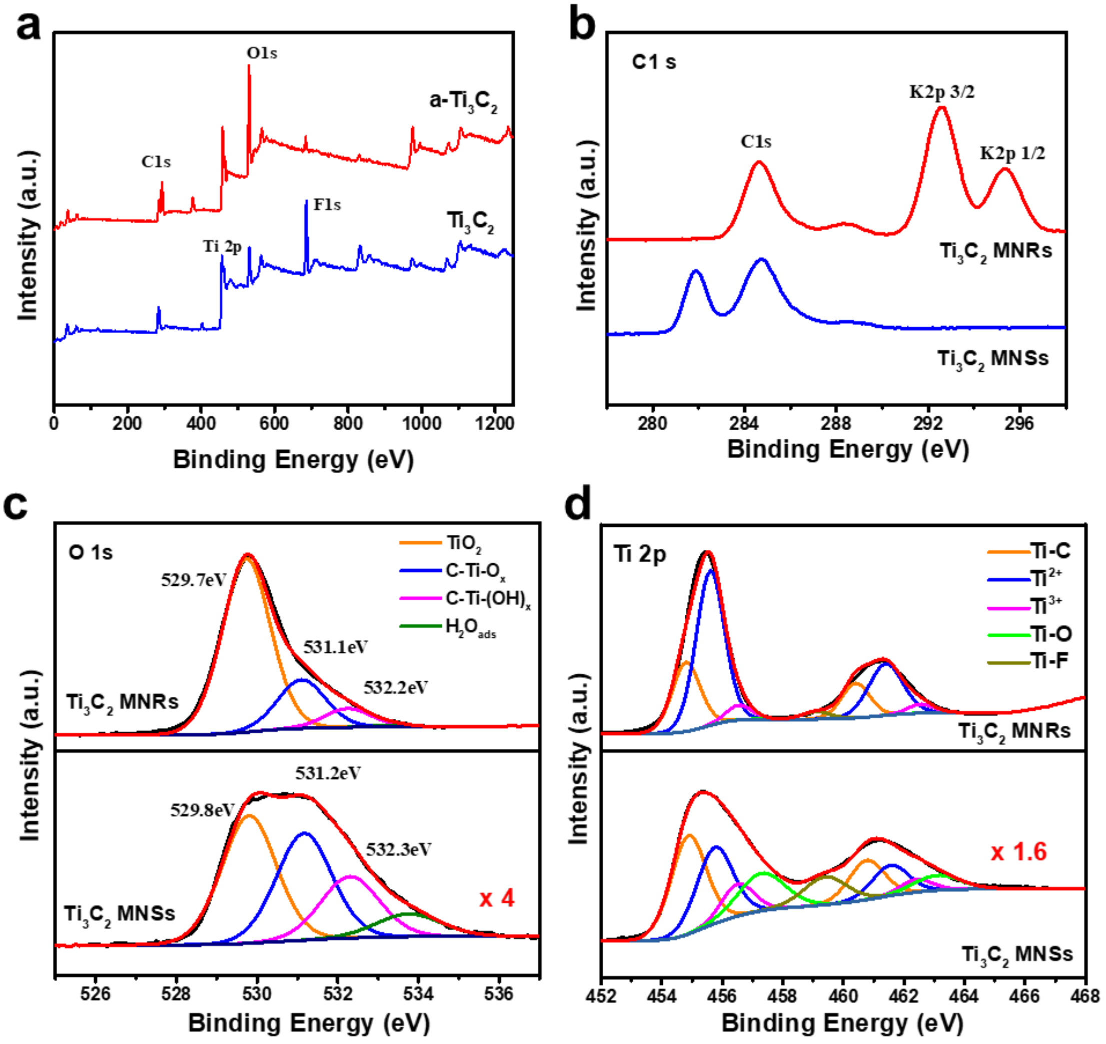

Figure 5.4 (a) Full XPS patterns of Ti_3C_2 MNRs and Ti_3C_2 MNSs. (b–d) XPS spectra of Ti_3C_2 MNRs and Ti_3C_2 MNSs in the (b) C 1s, (c) O 1s, and (d) Ti 2p regions.

After the treatment by KOH, the intensity of the XPS Ti-F peaks decreased markedly (Figure 5.4 a), while the contents of -OH on the surface increases significantly, indicating that a large amount of -F terminal groups were replaced by hydroxyl groups and consequently the formation of O-terminated Ti_3C_2 MNRs [22]. Energy-dispersive X-ray spectroscopy (EDX) analysis of Ti_3C_2 MNSs and Ti_3C_2 MNR samples confirm this indication (Figure 5.5 a, b). The comparison of the elemental composition by XPS and EDX (SEM) (Figures 5.5) show that after the treatment by KOH, the Ti/C ratio increases owing to the carbon corrosion by KOH. Being XPS detecting the surface composition with a depth less than about 5 nm while the detection depth for SEM is up to about 1 μm, the comparison of Ti/C ratios measured by XPS and EDX indicates a preferential surface carbon removal by the KOH treatment. The EDX of MAX phase (Ti_3AlC_2) and Ti_3C_2 MNSs (Table 5.1) indicates also that the oxygen content is similar in these two samples.

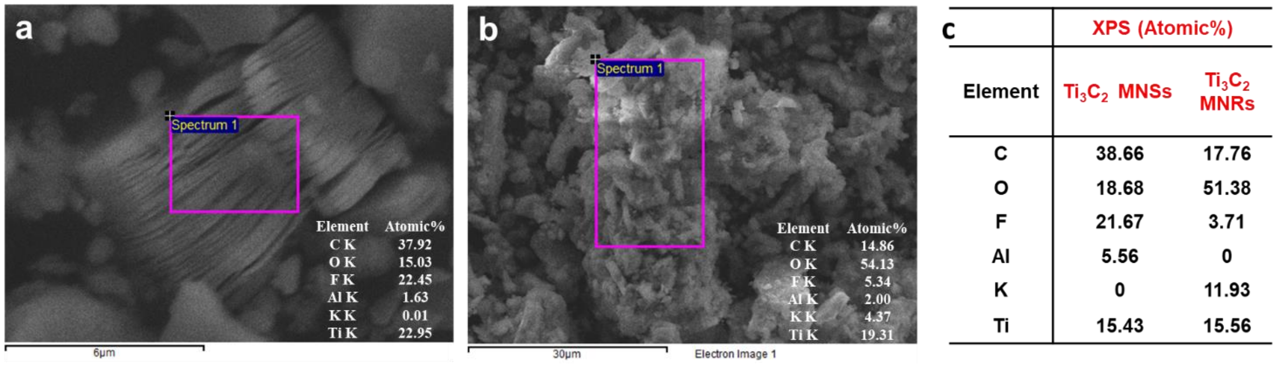

Element	Atomic%
C K	37.92
O K	15.03
F K	22.45
Al K	1.63
K K	0.01
Ti K	22.95

Element	Atomic%
C K	14.86
O K	54.13
F K	5.34
Al K	2.00
K K	4.37
Ti K	19.31

	XPS (Atomic%)	
Element	Ti_3C_2 MNSs	Ti_3C_2 MNRs
C	38.66	17.76
O	18.68	51.38
F	21.67	3.71
Al	5.56	0
K	0	11.93
Ti	15.43	15.56

Figure 5.5 SEM image and EDX analysis of the marked zone in (a) Ti_3C_2 MNSs and (b) Ti_3C_2 MNR. (c) XPS elemental content analysis of Ti_3C_2 MNSs and Ti_3C_2 MNR.

Table 5.1 Comparison of the EDX elemental composition (atomic % content) of Ti_3AlC_2 (MAX phase) and Ti_3C_2 MNS.

Element (K line)	Ti_3AlC_2 (MAX)	Ti_3C_2 MNS
C	42.15	37.92
O	16.88	15.03
F	0.64	22.45
Al	10.02	1.63
K	0.00	0.01
Ti	30.32	22.95

Figure 5.4 c and d report the XPS Ti 2p and O 1s regions for the Ti_3C_2 MNRs (top) and MNSs (bottom) samples, respectively. Deconvolution of the spectra is also reported according to Lian et al [17] and Halim et al [23]. For the Ti 2p region, spectra were deconvoluted for Ti-C, Ti^{2+}, Ti^{3+} and TiO_2 components, whereas for O 1s region spectra were deconvoluted in Ti-O and -OH components. Figure 5.4 c well indicates that the relative content of Ti-C decreased after KOH treatment with part of Ti-C transformed into Ti^{2+} and Ti^{3+}, This result is well consistent with the increase of O content commented before. Ti- F component also disappears after the MNSs to MNRs conversion. Figure 5.4 d evidences that the conversion leads to a significant increase in the Ti-O component (note that the spectra of Ti_3C_2 MNSs are multiplied by a factor three in intensity).

5.4 Performance tests in ammonia synthesis

5.4.1 NRR with different potentials

CV tests were initially made with the MXene nanoribbon cathode to analyze the range to explore for the electrocatalytic tests. Figure 5.6a reports the CV curves obtained in the full range (from -1V to +1 V vs. RHE), while Figure 5.6b reports an expansion in the 1V to +0.2 V vs. RHE.

Apart from a slight change in the first cycle, the CV curves are very well coincident, indicating the stability of performances during consecutive cycles.

Based on these tests, three values of potential to apply for the electrocatalytic tests were identified: -0.2 V, which corresponds to the value close to onset potential, -0.5 V corresponding to the maximum of current of the first reduction peaks, and -0.8 V corresponding to the onset of a new reduction.

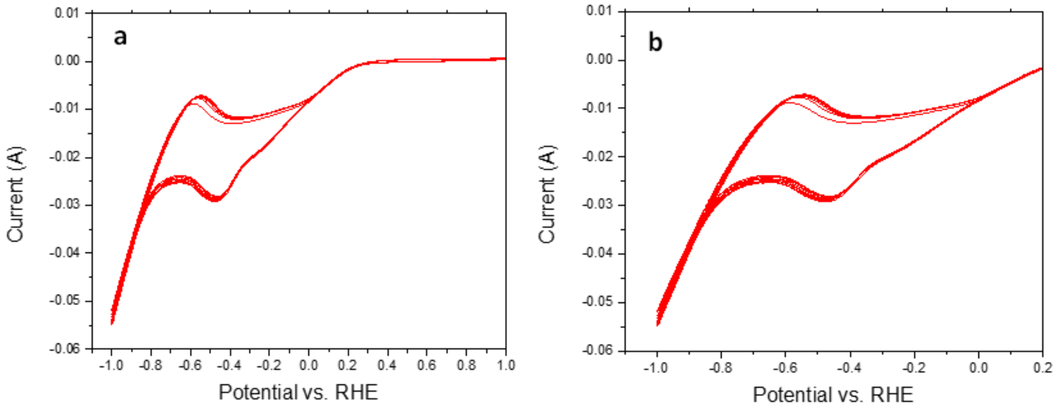

Figure 5.6 Cyclic voltammetry (CV) tests on Ti_3C_2 MNR. (a) Full range from -1V to +1 V vs. RHE. (b) Expansion in the -1 V to +0.2 V vs. RHE.

These initial tests were performed on Ti_3C_2 MNRs. Note that the scope of this work is not to obtain the maximum possible performances, but to understand better the effect of changing from 2D to 3D like nanostructure. Thus, no intermediate voltages were applied.

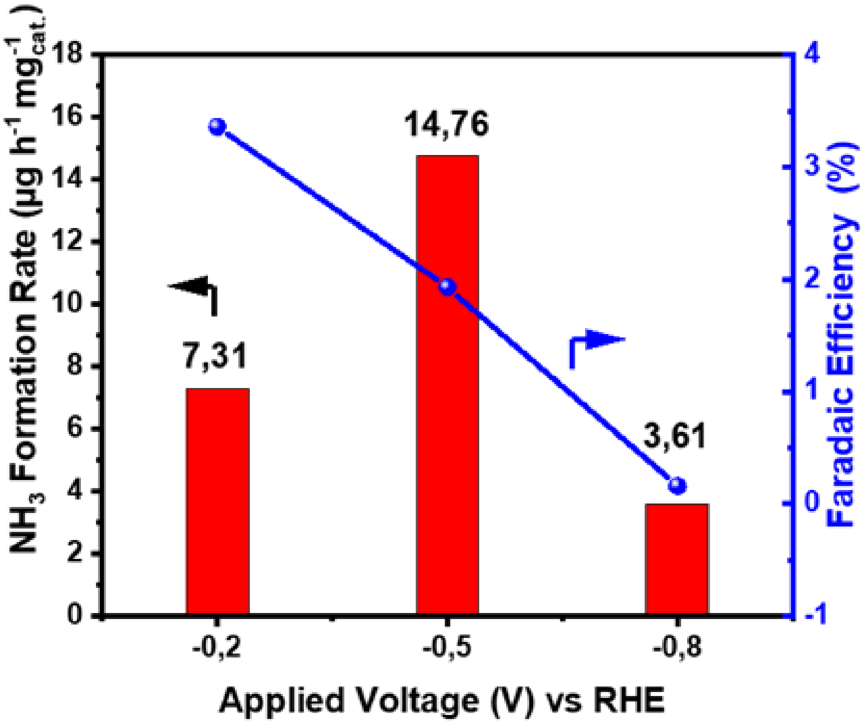

Figure 5.7 NH_3 formation rate and Faradaic efficiency of Ti_3C_2 MNRs at different potentials vs. RHE

The highest NH_3 yield was obtained at -0.5 V vs RHE (Figure 5.7). Current density at this voltage is about -1.5 µA and remains stable for at least 3 h of continuous tests (Figure 5.8). The current density remains stable also in longer term tests (up to about 10 h), showing that the electrocatalyst is stable under these experimental conditions.

This result is also in well agreement with CV tests (see Figure 5.6). At more negative voltage (-0.8 V), the current density instead increases (in negative) from the initial -3.5 μA value to about -4.5 μA (after 2 h), thus indicating an in situ transformation during the electrocatalytic tests. At a voltage of -0.2 V, the current density (about -0.5 μA) is instead low, indicating low catalytic activity. Further tests were thus made at - 0.5 V. Data reported refer to the behaviour determined after 3 h of continuous tests.

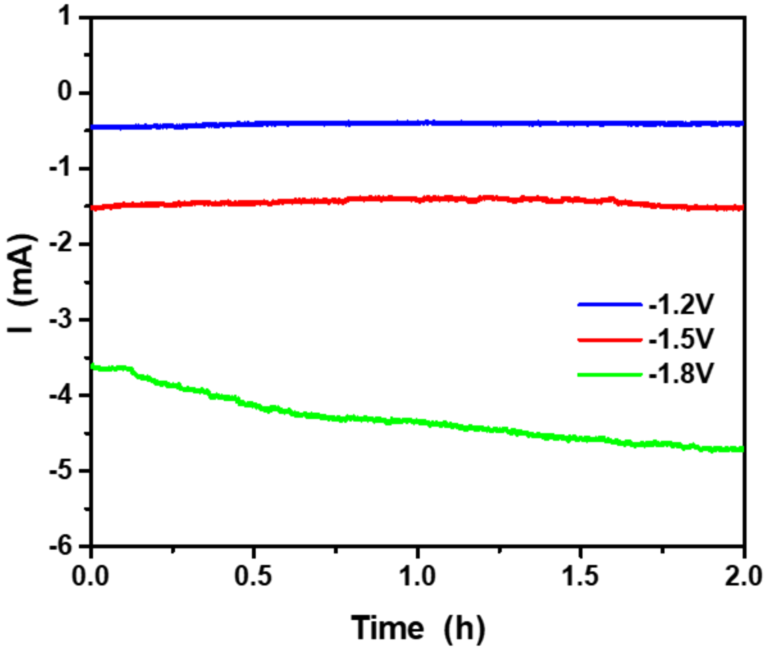

Figure 5.8 Time-dependent current density curves for Ti_3C_2 MNRs at different potentials vs. RHE.

5.4.2 NRR with different catalysts

Figure 5.9 reports the comparison of the rate of ammonia formation per mg of electrocatalysts for the pristine Ti_3AlC_2, Ti_3C_2 MNSs and Ti_3C_2 MNRs samples. The NH_3 yields are determined as 3.09, 2.37 and 14.76 μg h^{-1} $mgcat^{-2}$ with pristine Ti_3AlC_2, Ti_3C_2 MNSs and Ti_3C_2 MNRs as catalyst, respectively. The highest NH_3 yield is obtained on Ti_3C_2 MNRs with a FE of 1.93%. Pristine Ti_3AlC_2 and Ti_3C_2 MNSs have a quite comparable low activity in NRR, while Ti_3C_2 MNRs show a more than 5 times higher activity. Faradaic efficiency also increases to about 2% after transformation to nanoribbon. A stable current density was shown for all samples, indicating a stable behaviour at the applied voltage at least for 3h of continuous tests.

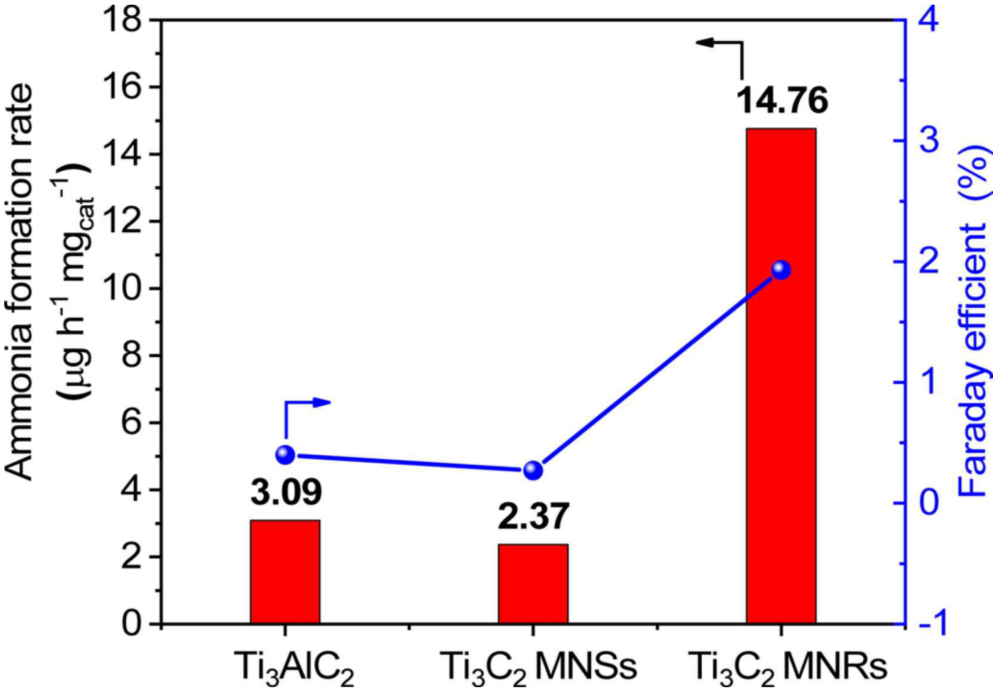

Figure 5.9 Ammonia formation rate and Faradaic efficiency with different electrodes at −0.5 V vs. RHE after 3 h of electrocatalytic tests at room temperature and ambient pressure.

SEM characterization of the most active Ti_3C_2 MNRs sample, fresh and after 2h and 10h of catalytic tests are reported in Figure 5.10a, b, c, respectively. There is no evidence of morphological changes with the time on stream of the nanoribbons, with respect to the fresh sample. These data are in well agreement with also CV experiments during extended cycling tests.

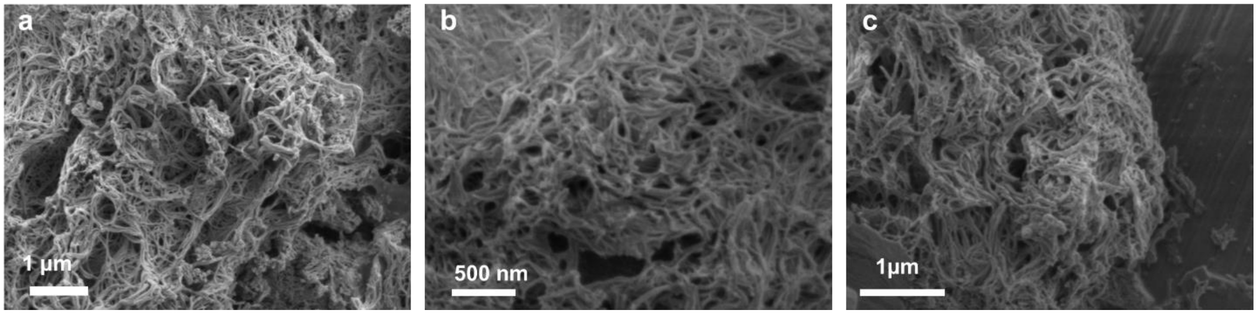

Figure 5.10 SEM images of Ti_3C_2 MNRs fresh (a) and after 2h (b) and 10h (c) of catalytic tests at a potential of -0.5 V vs. RHE.

XPS Ti2p spectra of fresh and used Ti_3C_2 MNRs (Figure 5.11) also do not evidence changes in the surface characteristics of this electrocatalyst before and after the catalytic tests, confirming the stability during NRR electrocatalytic tests.

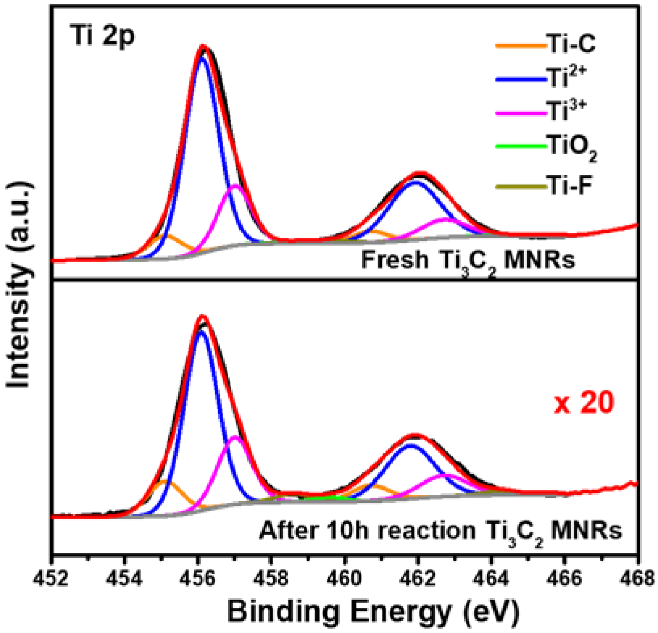

Figure 5.11 XPS spectra (Ti2p region) of Ti_3C_2 MNRs after extended catalytic tests (10h) at a potential of -0.5 V vs. RHE.

These results thus show that morphological, structural, surface and reactivity characteristics of Ti_3C_2 MNRs remain unchanged at least for 10h of continuous electrocatalytic tests at -0.5V vs. RHE.

A linear relationship could be observed between the rate of ammonia formation in the three samples reported in Figure 5.9 and the amount of oxygen on the surface (atomic %) as detected by XPS measurements (Figure 5.12), suggesting a relationship between these two aspects. The relationship presented in Figure 5.12 agrees (among others) with (i) Xia et al [11]. indications that exposed Ti sites (Ti_3C_2OH) are responsible for the improved electron transfer, adsorption and activation of dinitrogen, (ii) theoretical results of Tang et al [24] that exposed Ti atom close to extra oxygen vacancy are responsible for activity in (defective) MXenes electrocatalysts, (iii) Jin et al [25] indications that OH-rich MXenes (Ti_3C_2OH) show high NRR performances and (iv) Xia et al [11] results that surface hydroxyl modification of MXene Ti_3C_2 facilitates the electron transfer and the adsorption and activation of dinitrogen. Therefore, this work shows that the transformation from a 2D-like morphology (nanosheets) to a 3D-like morphology (nanoribbons) leads to a large improvement in the NRR activity, due to an enhanced formation of active sites (likely Ti_3C_2OH) not blocked by F atoms.

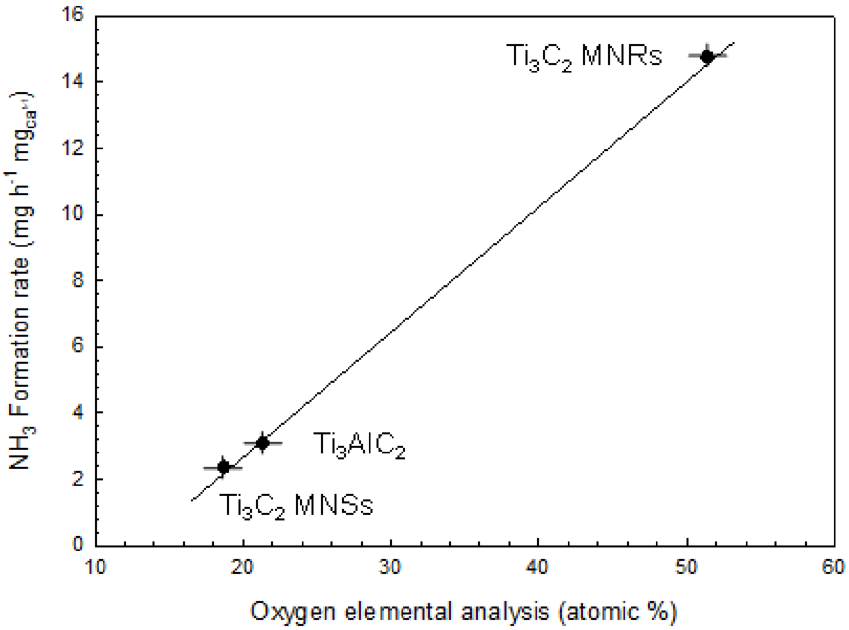

Figure 5.12 Relationship between ammonia formation rate at −0.5 V vs. RHE and atomic % of oxygen in the surface as measured by XPS.

To compare these data with literature, Table 5.2 reports a comparison of reaction conditions, ammonia formation rate and Faradaic selectivity of selected state-of-the-art literature results on NRR, organized in four classes of electrocatalytic materials: (a) MXenes, (b) modified and composite electrocatalysts based on MXenes, and electrocatalysts based on (c) noble metals or (d) transition metal oxides/sulphides. The comparison shows that particularly with respect to MXenes electrocatalysts, the electrocatalysts reported here well compare with other published, taking into account of the differences in the operating conditions, and the use here of an electrocatalytic reactor without liquid electrolyte differently from the other cases.

Table 5.2 Comparison with state-of-the-art representative electrocatalysts in NRR. Type of electrocatalysts: (a) MXenes, (b) modified and composite electrocatalysts based on MXenes, selected electrocatalysts based on (c) noble metals or (d) transition metal oxides.

Composition (*)	FE (%)	NH_3 Formation rate ($\mu g \cdot h^{-1} \cdot mg_{cat}^{-1}$)	Potential applied (V) and electrolyte	Ref.
(a) Pure MXenes				
Ti_3C_2 MNRs	2.0	14.8	-0.5 vs RHE 0.5 M KOH	This work
Ti_3C_2 MNSs	0.7	2.4		
$Ti_3C_2T_x$ nanosheets	2.0	6.5	-0.2 vs RHE 0.05 M H_2SO_4	[12]
Ti_3C_2 nanosheets	1.0	30.3	-0.3 vs RHE 0.1 M HCl	[26]
OH-rich $Ti_3C_2T_x$ QDs	13.3	62.9	-0.5 vs RHE 0.1 M HCl	[25]
OH-surface rich Ti_3C_2	7.0	1.71	-0.2 vs RHE 0.1 M KOH	[11]
$Ti_3C_2T_x$	1.5	22.4	-0.6 vs RHE 0.1 M HCl	[27]
$Ti_3C_2T_x$ nanosheet/CP	9.3	20.4	-0.4 vs RHE 0.1 M HCl	[28]
HF-$Ti_3C_2T_x$ nanosheets/CC	6.0	15.0	-0.3 vs RHE 0.1 M HCl	[29]
F-free $Ti_3C_2T_x$ nanosheets/CC	9.1	36.9		
$Ti_3C_2T_x$/CP	3.0	10.2	-0.6 vs RHE 0.1 M HCl	[30]
$Ti_3C_2T_x$ MXene / SSM	4.6	2.7	-0.1 vs RHE 0.5 M Li_2SO_4	[7]
Mo_2CT_X MXene	7.0	10.0	-0.3 vs RHE 0.5 M K_2SO_4	[31]
(b) Modified and composite MXenes				
MXene/ TiFeOx-700	24.4	21.9	-0.2 vs RHE 0.05 M H_2SO_4	[12]
1T-MoS_2/ Ti_3C_2 MXene	10.9	39.3	-0.3 vs RHE 0.1 M HCl	[26]
$Ti_3C_2T_x$/ TiO_2 (vacancy rich)	3.0	32.0	-0.6 vs RHE 0.1 M HCl	[27]
TiO_2/$Ti_3C_2T_x$ /CP	8.4	26.3	-0.6 vs RHE 0.1 M HCl	[30]
$Ti_3C_2T_x$ MXene / FeOOH	5.8	0.2	-0.1 vs RHE 0.5 M Li_2SO_4	[7]
MnO_2–$Ti_3C_2T_x$	11.9	34.1	-0.5 vs RHE 0.1 M HCl	[32]
Mn_3O_4/ MXene nanosheets	5.5	25.9	-0.5 vs RHE 0.1 M Na_2SO_4	[33]
(c) Noble-metal based electrocatalysts				
Ru-single atom Mo_2CT_X MXene	25.8	40.6	-0.3 vs RHE 0.5 M K_2SO_4	[31]
Ru/C	12.5	20.0		
Au nanoroads	4.0	1.6	-0.2 vs RHE 0.1 M KOH	[34]

Pd/C	8.2	4.5	-0.1 vs RHE 0.1M PBS	[35]
Rh nanosheets	0.3	23.9	-0.2 vs RHE 0.1 M KOH	[36]
α-Au/CeOx-RGO	10.1	8.3	-0.2 vs RHE 0.1 M HCl	[37]
(d) Transition metal oxide/sulphide based electrocatalysts				
Fe_2O_3/CNT 3h activated in situ	17.0	41.6	-0.5 vs RHE 0.5 M KOH	[38]
TiO_2/rGO	3.3	15.1	-0.9 vs RHE 0.1 M Na_2SO_4	[39]
amorphous $Bi_4V_2O_{11}/CeO_2$	10.1	23.2	-0.2 vs RHE 0.1 M HCl	[40]
Nb_2O_5 nanofibers	9.3	43.6	-0.6 vs RHE 0.1 M HCl	[41]
MoO_3 nanosheets	0.8	29.4	-0.5 vs RHE 0.1 M HCl	[42]
MnO_x nanowire	11.4	1.5	-0.5 vs RHE 0.1 M Na_2SO_4	[43]
Mn_3O_4 nanocube	3.0	11.6	-0.5 vs RHE 0.1 M Na_2SO_4	[44]
N-doped C/ Fe_3C	2.7	15.8	-0.4 vs RHE 0.01 M KOH	[45]
Mo- MnO_2 nanoflowers	7.7	36.6	-0.5 vs RHE 0.1 M Na_2SO_4	[46]
MoS_2/C_3N_4	17.8	18.5	-0.3 vs RHE -	[47]
Mo-SnS_2 nanosheets (&)	20.8 (-0.4V)	41.3	-0.5 vs RHE 0.5M $LiClO_4$	[48]
$FeMoO_4$ Nanorods	7.5	45.8	-0.5 vs RHE 0.5 M LiClO4	[49]

5.4.3 Circular reaction and control experiments

A series of control tests were made to assure that ammonia forms from N_2 feed rather than from other N sources and to verify that ammonia derives from an electrocatalytic process, following the protocol described in detail in Chapter 2 to avoid false positive in ammonia detection.

A verification was made that NO_x was not present in the N_2 pure feed used in the present tests, and that contaminations by NH_3 were also not present in the feed section of the electrocatalytic apparatus. These control experiments were further supported by switching tests with Ar feed.

In these switching-feed tests, the procedure for the electrocatalytic tests is made as described before, but only Ar is feed rather than N_2. After the initial phase of pre-treatment to stabilize the electrode, the first two hours of electrocatalytic tests are made by applying the chosen potential (-0.5 V vs RHE), but feeding Ar; then, the feed is switched to N_2, maintaining constant the applied potential and ammonia formation is monitored for at least 3h; after these tests, the potential is decreased to zero, and a feed of N_2 + 5% H_2 is feed to verify the catalytic (rather than electrocatalytic) activity in ammonia formation. The results are reported in Figure 5.13. It is shown clearly that i) ammonia forms only when gaseous N_2 is feed and thus ammonia does not derive from contaminations by other N-compounds present in the reactor or its components, and ii) after switching to N_2 there is a stable ammonia formation for at least 2h of running test.

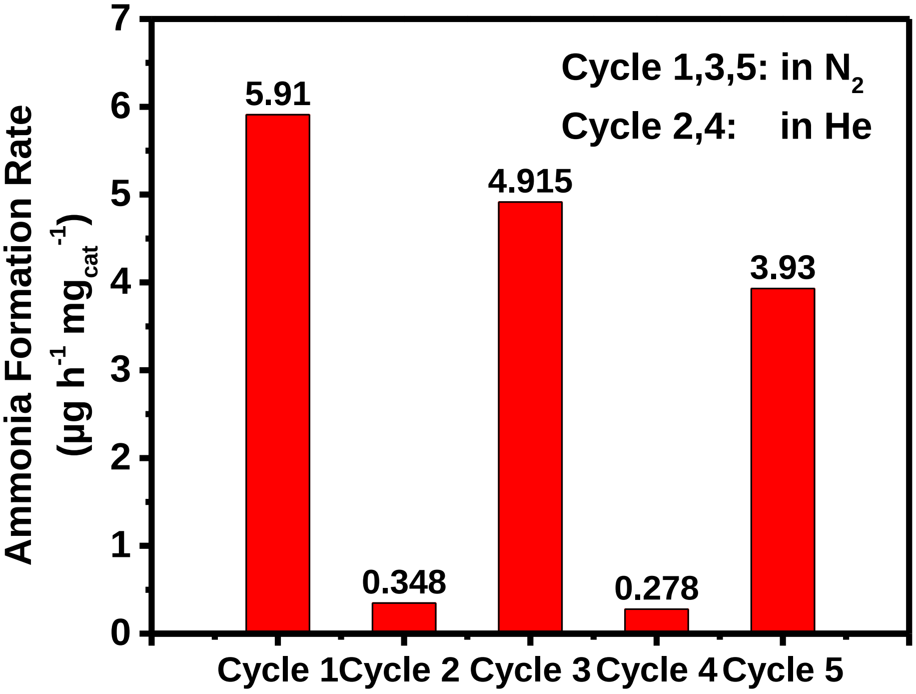

Figure 5.13 Experimental protocol for NRR tests.

Control tests with labelled $^{15}N_2$ were also made to verify formation of ammonia from gas N_2 [50], monitoring $^{15}NH_3$ by NMR, but these tests do not provide different results. We consider preferable the procedure indicated in Figure 5.13, because it can be applied to all tests.

Further control experiments regarded tests feeding N_2 and H_2, but without application of a potential to the electrocatalyst, confirm that i) ammonia does not derive from the catalytic reduction of contaminant N-species and ii) the behaviour observed derives from the electrocatalytic reduction rather than from the catalytic reduction in presence of in-situ generated H_2.

5.5 Conclusions

In summary, the fabrication of a novel 3D porous framework of alkalized Ti_3C_2 MNRs derived from Ti_3C_2 MNSs in KOH solution has been demonstrated. After the preliminary exploration, ammonia synthesis from the electrochemical reduction of N_2 can be achieved on Ti_3C_2 MNRs under ambient conditions in a compact homemade three-phase reactor. Both the ammonia formation rate (14.76 $\mu g\ h^{-1}\ mg_{cat}^{-2}$) and EF (1.93%) improved significantly with Ti_3C_2 MNRs materials. Based on literature, the basal plane of MXene is relatively inert and its activity is related to a greater number of exposed edge sites. In this work, Ti_3C_2 MXene nanoribbons from Mxene nanosheets were prepared to obtain more edge sites and O-terminate, which significantly improved the yield and selectivity of NH_3 electro-synthesis.

The results evidence that a 2D (nanosheet) morphology is not necessary in MXene materials to provide activity in NRR, and a different morphology (nanoribbon), not having the same basal planes and type of edges, shows instead an about five-time higher catalytic activity. Characterization data indicate that in nanoribbon morphology, there is a preferential formation of exposed Ti-O sites, which various studies have indicated as responsible for improved electron transfer, adsorption, and activation of dinitrogen. Present data agree with this interpretation, and evidence for the first time the presence of a linear relationship between ammonia formation rate and amount of oxygen on the surface of Ti_3C_2 MXene.

5.6 Connected Experimental Section

Transmission Electron Microscopy (TEM). In the Transmission Electron Microscopy (TEM), a beam of electrons were accelerated and then were transmitted onto the very thin sample layer [51]. The electrons interact with the atoms in sample thus influencing the direction of electrons and generating the solid angle scattering. Scattering angle is relevant with the density and thickness of the sample, so it can present the image with different intensity. The images can be magnified and focused on the image device.

High-resolution transmission electron microscopy (TEM) was carried out on Titan Themis ETEM G3 (Thermofisher) at 300 kV. The procedure for preparing samples for TEM analysis was as follows: firstly, the sample was grinded into very fine powders. It was dispersed in ethanol under ultrasound for 3 min. Then, one drop of liquid was deposited on copper grid. Once evaporated under room temperature, it was transferred into the chamber of TEM.

Scanning Electron Microscopy (SEM). Scanning Electron Microscopy (SEM) provides detailed high-resolution images of the sample by radiating a focused electron beam across the surface and detecting secondary or backscattered electron signals [52]. Due to the very narrow electron beam, SEM micrographs have a large depth of field yielding a characteristic three-dimensional appearance useful for understanding the surface structure of a sample. Spatially resolved quantitative Energy Dispersive X-Ray (EDX) is also used to provide information about elemental identification and quantitative composition.

Scanning electron microscopy (SEM) was performed on a JSM-7800F instrument at an accelerating voltage of 3 kV. Aberration-corrected STEM in high-angle annular dark field mode and energy dispersive X-ray spectroscopy (EDX) mapping were carried out on JEOL JEM ARM-200F instrument with the probe corrector at 200 kV.

X-ray Photoelectron Spectroscopy (XPS). X-ray Photoelectron Spectroscopy (XPS) is based on the photoelectric effect arising when high energy photons (usually in the ke V range) hit a material with the consequent emission of electrons (photoelectrons) [53]. The energy of an X-ray with particular wavelength is known (for Al K_α X-rays, $E_{photon} = 1486.7$ eV), and because the emitted electrons' kinetic energies are measured, the electron binding energy of each of the emitted electrons can be determined by using the photoelectric effect equation: $E_{binding} = E_{proton} - (E_{kinetic} + \Phi)$.

The XPS technique yields quantitative and qualitative information. Quantitative information arises from the element specificity of the binding energies and the relation between the intensity of the photoelectron peaks and the element concentration. Qualitative information are obtained from the energy position of a photoelectron peak with respect to the energy position of the same level in a reference compound (chemical shift).

XPS was conducted on a Thermofisher ESCALAB 250Xi spectrometer equipped with a monochromatic Al K_α radiation ($h\upsilon$= 1486.6 eV, working voltage = 12.5 kV, filament current = 16 mA), using a pass energy of 40 eV for the narrow scans. The energy calibration was based on the C 1 s at 284.8 eV.

5.7 References

[1] J. Li, C. Guo, C. M. Li, Recent Advances of Two‐Dimensional (2D) MXenes and Phosphorene for High‐Performance Rechargeable Batteries. *ChemSusChem* **2020,** 13(6): 1047-1070.

[2] R. Fang, C. Lu, A. Chen, K. Wang, H. Huang, Y. Gan, C. Liang, J. Zhang, X. Tao, Y. Xia, W. Zhang, 2D MXene‐based Energy Storage Materials: Interfacial Structure Design and Functionalization. *ChemSusChem* **2019**.

[3] T. A. Le, N. Q. Tran, Y. Hong, M. Kim, H. Lee, Porosity‐Engineering of MXene as a Support Material for a Highly Efficient Electrocatalyst toward Overall Water Splitting. *ChemSusChem*, **2020**.

[4] Z. Fu, N. Wang, D. Legut, C. Si, Q. Zhang, S. Du, T. C. Germann, J. S. Francisco, R. Zhang, Rational design of flexible two-dimensional MXenes with multiple functionalities. *Chemical Reviews* **2019**, 119(23): 11980-12031.

[5] A. Liu, Y. Yang, X. Ren, Q. Zhao, M. Gao, W. Guan, F. Meng, L. Gao, Q. Yang, T. Ma, X. Liang, Current Progress of Electrocatalysts for Ammonia Synthesis Through Electrochemical Nitrogen Reduction Under Ambient Conditions. *ChemSusChem* **2020**, 13(15): 3766-3788.

[6] B. Qin, Y.Li, Q. Zhang, G. Yang, H. Liang, F. Peng, Understanding of nitrogen fixation electro catalyzed by molybdenum-iron carbide through the experiment and theory. *Nano Energy* **2020**, 68: 104374.

[7] Luo, G.-F. Chen, L. Ding, X. Chen, L.-X. Ding, H. Wang, Efficient electrocatalytic N_2 fixation with MXene under ambient conditions. *Joule* **2019**, 3(1): 279-289.

[8] J. D. Gouveia, A. Morales-Garcia, F. Vines, F. Illas, J. R. B. Gomes, MXenes as promising catalysts for water dissociation. *Applied Catalysis B: Environmental* **2020**, 260: 118191.

[9] S. Wang, B. Li, L. Li, Z. Tian, Q. Zhang, L. Chen, X. C. Zeng, Highly efficient N_2 fixation catalysts: transition-metal carbides M 2 C (MXenes). *Nanoscale* **2020**, 12(2): 538-547.

[10] L. R. Johnson, S. Sridhar, L. Zhang, K. D. Fredrickson, A. S. Raman, J. Jang, C. Leach, A. Padmanabhan, C. C. Price, N. C. Frey, A. Raizada, V. Rajaraman, S. A. Saiprasad, X. Tang, A. Vojvodic, MXene Materials for the Electrochemical Nitrogen Reduction—Functionalized or Not?. *ACS Catalysis* **2019**, 10(1): 253-264.

[11] J. Xia, S.-Z. Yang, B. Wang, P. Wu, I. Popovs, H. Li, S. Irle, S. Dai, H. Zhu, Boosting electrosynthesis of ammonia on surface-engineered MXene Ti_3C_2. *Nano Energy* **2020**: 104681.

[12] Y. Guo, T. Wang, Q. Yang, X. Li, H. Li, Y. Wang, T. Jiao, Z. Huang, B. Dong, W. Zhang, J. Fan, C. Zhi, Highly Efficient Electrochemical Reduction of Nitrogen to Ammonia on Surface Termination Modified Ti3C2T x MXene Nanosheets. *ACS nano* **2020**, 14(7): 9089-9097.

[13] C. J. Heard, J. Čejka, M. Opanasenko, P. Nachtigall, G. Centi, S. Perathoner, 2D oxide nanomaterials to address the energy transition and catalysis. *Advanced Materials* **2019**, 31(3): 1801712.

[14] G. Centi, S. Perathoner, Coord. Creating and mastering nano-objects to design advanced catalytic materials. *Coordination Chemistry Reviews* **2011**, 255(13-14): 1480-1498.

[15] Z. Wu, T. Shang, Y. Deng, Y. Tao, Q.-H. Yang, The Assembly of MXenes from 2D to 3D. *Advanced Science* **2020**, 7(7): 1903077. 1.

[16] Wei, H.; Jiang, Q.; Ampelli, C.; Chen, S.; Perathoner, S.; Liu, Y.; Centi, G., Enhancing N_2 Fixation Activity by Converting Ti 3 C 2 MXenes Nanosheets to Nanoribbons. *ChemSusChem* **2020,** *13* (21), 5614-5619.

[17] P. Lian, Y. Dong, Z.-S. Wu, S. Zheng, X. Wang, S. Wang, C. Sun, J. Qin, X. Shi, X. Bao, Alkalized Ti_3C_2 MXene nanoribbons with expanded interlayer spacing for high-capacity sodium and potassium ion batteries. *Nano Energy* **2017**, 40: 1-8.

[18] M. Alhabeb, K. Maleski, T. S. Mathis, A. Sarycheva, C. B. Hatter, S. Uzun, A. Levitt, Y. Gogotsi, Angew. Chem. 2018, 130, 5542. Selective etching of silicon from Ti_3SiC_2 (MAX) to obtain 2D titanium carbide (MXene). *Angewandte Chemie* **2018**, 130(19): 5542-5546.

[19] Li, J.; Yan, D.; Hou, S.; Li, Y.; Lu, T.; Yao, Y.; Pan, L., Improved sodium-ion storage performance of $Ti_3C_2T_x$ MXenes by sulfur doping. *Journal of Materials Chemistry A* **2018,** *6* (3), 1234-1243.

[20] Ghidiu, M.; Lukatskaya, M. R.; Zhao, M.-Q.; Gogotsi, Y.; Barsoum, M., Conductive two-dimensional titanium carbide ‘clay’ with high volumetric capacitance. *Nature* **2014,** *516* (7529), 78-81.

[21] Mashtalir, O.; Naguib, M.; Mochalin, V. N.; Dall'Agnese, Y.; Heon, M.; Barsoum, M. W.; Gogotsi, Y., Intercalation and delamination of layered carbides and carbonitrides. *Nature communications* **2013**, 4 (1), 1-7.

[22] Li, J.; Yuan, X.; Lin, C.; Yang, Y.; Xu, L.; Du, X.; Xie, J.; Lin, J.; Sun, J., Achieving high pseudocapacitance of 2D titanium carbide (MXene) by cation intercalation and surface modification. *Advanced Energy Materials* **2017,** *7* (15), 1602725.

[23] Halim, J.; Cook, K. M.; Naguib, M.; Eklund, P.; Gogotsi, Y.; Rosen, J.; Barsoum, M. W., X-ray photoelectron spectroscopy of select multi-layered transition metal carbides (MXenes). *Applied Surface Science* **2016,** *362*, 406-417.

[24] Tang, S.; Liu, T.; Dang, Q.; Zhou, X.; Li, X.; Yang, T.; Luo, Y.; Sharman, E.; Jiang, J., Synergistic Effect of Surface-Terminated Oxygen Vacancy and Single-Atom Catalysts on Defective MXenes for Efficient Nitrogen Fixation. *The Journal of Physical Chemistry Letters* **2020,** *11* (13), 5051-5058.

[25] Jin, Z.; Liu, C.; Liu, Z.; Han, J.; Fang, Y.; Han, Y.; Niu, Y.; Wu, Y.; Sun, C.; Xu, Y. J. A. E. M., Rational Design of Hydroxyl-Rich $Ti_3C_2T_x$ MXene Quantum Dots for High‐Performance Electrochemical N_2 Reduction. *Advanced Energy Materials* **2020**, 2000797.

[26] Sun, D.; Bai, H.; Zhao, Y.; Zhang, Q.; Bai, Y.; Liu, Y.; Pang, X.; Wang, F.; Ding, J.; Xu, D. J. A. A. M.; Interfaces, Amorphous $MnCO_3$/C Double Layers Decorated on $BiVO_4$ Photoelectrodes to Boost Nitrogen Reduction. *ACS Applied Materials* **2020**.

[27] Fang, Y.; Liu, Z.; Han, J.; Jin, Z.; Han, Y.; Wang, F.; Niu, Y.; Wu, Y.; Xu, Y., High‐Performance Electrocatalytic Conversion of N_2 to NH_3 Using Oxygen‐Vacancy‐Rich TiO_2 In Situ Grown on $Ti_3C_2T_x$ MXene. *Advanced Energy Materials* **2019,** *9* (16), 1803406.

[28] Zhao, J.; Zhang, L.; Xie, X.-Y.; Li, X.; Ma, Y.; Liu, Q.; Fang, W.-H.; Shi, X.; Cui, G.; Sun, X., Ti 3 C 2 T x (T= F, OH) MXene nanosheets: conductive 2D catalysts for ambient electrohydrogenation of N_2 to NH_3. *Journal of Materials Chemistry A* **2018,** *6* (47), 24031-24035.

[29] Li, T.; Yan, X.; Huang, L.; Li, J.; Yao, L.; Zhu, Q.; Wang, W.; Abbas, W.; Naz, R.; Gu, J., Fluorine-free $Ti_3C_2T_x$ (T= O, OH) nanosheets (∼ 50–100 nm) for nitrogen fixation under ambient conditions. *Journal of Materials Chemistry A* **2019,** *7* (24), 14462-14465.

[30] Zhang, J.; Yang, L.; Wang, H.; Zhu, G.; Wen, H.; Feng, H.; Sun, X.; Guan, X.; Wen, J.; Yao, Y., In Situ Hydrothermal Growth of TiO2 Nanoparticles on a Conductive $Ti_3C_2T_x$ MXene Nanosheet: A Synergistically Active Ti-Based Nanohybrid Electrocatalyst for Enhanced N_2 Reduction to NH_3 at Ambient Conditions. *Inorganic chemistry* **2019,** *58* (9), 5414-5418.

[31] Peng, W.; Luo, M.; Xu, X.; Jiang, K.; Peng, M.; Chen, D.; Chan, T. S.; Tan, Y., Spontaneous Atomic Ruthenium Doping in Mo_2CT_X MXene Defects Enhances Electrocatalytic Activity for the Nitrogen Reduction Reaction. *Advanced Energy Materials* **2020**, 2001364.

[32] Kong, W.; Gong, F. F.; Zhou, Q.; Yu, G.; Ji, L.; Sun, X.; Asiri, A. M.; Wang, T.; Luo, Y.; Xu, Y., An MnO_2-$Ti_3C_2T_x$ MXene nanohybrid: an

efficient and durable electrocatalyst toward artificial N 2 fixation to NH 3 under ambient conditions. *Journal of Materials Chemistry A* **2019,** *7* (32), 18823-18827.

[33] Wang, C.; Zhu, X.-D.; Zuo, P.-J., Novel Confinement of Mn3O4 Nanoparticles on Two-dimensional Carbide Enabling High-performance Electrochemical Synthesis of Ammonia under Ambient Conditions. *Chemical Engineering Journal* **2020**, 125163.

[34] Bao, D.; Zhang, Q.; Meng, F. L.; Zhong, H. X.; Shi, M. M.; Zhang, Y.; Yan, J. M.; Jiang, Q.; Zhang, X. B., Electrochemical reduction of N_2 under ambient conditions for artificial N_2 fixation and renewable energy storage using N_2/NH_3 cycle. *Advanced materials* **2017,** *29* (3), 1604799.

[35] Wang, J.; Yu, L.; Hu, L.; Chen, G.; Xin, H.; Feng, X., Ambient ammonia synthesis via palladium-catalyzed electrohydrogenation of dinitrogen at low overpotential. *Nature communications* **2018,** *9* (1), 1-7.

[36] Liu, H.-M.; Han, S.-H.; Zhao, Y.; Zhu, Y.-Y.; Tian, X.-L.; Zeng, J.-H.; Jiang, J.-X.; Xia, B. Y.; Chen, Y., Surfactant-free atomically ultrathin rhodium nanosheet nanoassemblies for efficient nitrogen electroreduction. *Journal of Materials Chemistry A* **2018,** *6* (7), 3211-3217.

[37] Li, S. J.; Bao, D.; Shi, M. M.; Wulan, B. R.; Yan, J. M.; Jiang, Q., Amorphizing of Au nanoparticles by CeO_x–RGO hybrid support towards highly efficient electrocatalyst for N2 reduction under ambient conditions. *Advanced materials* **2017,** *29* (33), 1700001.

[38] Chen, S.; Perathoner, S.; Ampelli, C.; Wei, H.; Abate, S.; Zhang, B.; Centi, G., Enhanced performance in the direct electrocatalytic synthesis

of ammonia from N_2 and H_2O by an in-situ electrochemical activation of CNT-supported iron oxide nanoparticles. *Journal of Energy Chemistry* **2020,** *49*, 22-32.

[39] Zhang, X.; Liu, Q.; Shi, X.; Asiri, A. M.; Luo, Y.; Sun, X.; Li, T., TiO_2 nanoparticles–reduced graphene oxide hybrid: an efficient and durable electrocatalyst toward artificial N_2 fixation to NH_3 under ambient conditions. *Journal of Materials Chemistry A* **2018,** *6* (36), 17303-17306.

[40] Lv, C.; Yan, C.; Chen, G.; Ding, Y.; Sun, J.; Zhou, Y.; Yu, G., An Amorphous Noble‐Metal‐Free Electrocatalyst that Enables Nitrogen Fixation under Ambient Conditions. *Angewandte Chemie* **2018,** *130* (21), 6181-6184.

[41] Han, J.; Liu, Z.; Ma, Y.; Cui, G.; Xie, F.; Wang, F.; Wu, Y.; Gao, S.; Xu, Y.; Sun, X., Ambient N_2 fixation to NH_3 at ambient conditions: Using Nb_2O_5 nanofiber as a high-performance electrocatalyst. *Nano Energy* **2018,** *52*, 264-270.

[42] Han, J.; Ji, X.; Ren, X.; Cui, G.; Li, L.; Xie, F.; Wang, H.; Li, B.; Sun, X., MoO_3 nanosheets for efficient electrocatalytic N_2 fixation to NH_3. *Journal of Materials Chemistry A* **2018,** *6* (27), 12974-12977.

[43] Zhang, L.; Xie, X.-Y.; Wang, H.; Ji, L.; Zhang, Y.; Chen, H.; Li, T.; Luo, Y.; Cui, G.; Sun, X., Boosting electrocatalytic N_2 reduction by MnO_2 with oxygen vacancies. *Chemical Communications* **2019,** *55* (32), 4627-4630.

[44] Wu, X.; Xia, L.; Wang, Y.; Lu, W.; Liu, Q.; Shi, X.; Sun, X., Mn_3O_4 nanocube: An efficient electrocatalyst toward artificial N_2 fixation to NH_3. *Small* **2018,** *14* (48), 1803111.

[45] Cong, L.; Yu, Z.; Liu, F.; Huang, W.; Technology, Electrochemical synthesis of ammonia from N_2 and H_2O using a typical non-noble metal carbon-based catalyst under ambient conditions. *Catalysis Science* **2019,** *9* (5), 1208-1214.

[46] Chu, K.; Liu, Y.-p.; Li, Y.-b.; Guo, Y.-l.; Tian, Y.; Zhang, H., Multi-functional Mo-doping in MnO_2 nanoflowers toward efficient and robust electrocatalytic nitrogen fixation. *Applied Catalysis B: Environmental* **2020,** *264*, 118525.

[47] Li, Q.; Guo, Y.; Tian, Y.; Liu, W.; Chu, K., Activating VS_2 basal planes for enhanced NRR electrocatalysis: the synergistic role of S-vacancies and B dopants. *Journal of Materials Chemistry A* **2020,** *8* (32), 16195-16202.

[48] Chu, K.; Wang, J.; Liu, Y.-p.; Li, Q.-q.; Guo, Y.-l., Mo-doped SnS_2 with enriched S-vacancies for highly efficient electrocatalytic N_2 reduction: the critical role of the Mo-Sn-Sn trimer. *Journal of Materials Chemistry A* **2020,** *8* (15), 7117-7124.

[49] Chu, K.; Li, Q.-q.; Cheng, Y.-h.; Liu, Y.-p.; Interfaces, Efficient Electrocatalytic Nitrogen Fixation on $FeMoO_4$ Nanorods. *ACS Applied Materials Interfaces* **2020,** *12* (10), 11789-11796.

[50] Kibsgaard, J.; Nørskov, J. K.; Chorkendorff, I., The difficulty of proving electrochemical ammonia synthesis. *ACS Energy Letters* **2019,** *4* (12), 2986-2988.

[51] Reimer, L., *Transmission electron microscopy: physics of image formation and microanalysis*. Springer: 2013; Vol. 36.

[52] Goldstein, J. I.; Newbury, D. E.; Michael, J. R.; Ritchie, N. W.; Scott, J. H. J.; Joy, D. C., *Scanning electron microscopy and X-ray microanalysis*. Springer: 2017.

[53] Venezia, A. M. J. C. T., X-ray photoelectron spectroscopy (XPS) for catalysts characterization. **2003,** *77* (4), 359-370.

6 General conclusions

The present PhD thesis has been focused on development of innovative electrodes for the electrocatalytic nitrogen reduction reaction (NRR) to ammonia in unconventional electrochemical devices.

This process is an example of activation of small molecules (i.e., N_2) and how they play an important role as building blocks for the production of fuels, chemicals, and fertilizers. Ammonia synthesis, is in fact, the largest-scale chemical process with the highest impact on greenhouse gas emissions (about 350 Mt CO_2 emissions worldwide). This value could be decreased by over 90% in a direct electrocatalytic process using N_2, H_2O and renewable energy as input sources. Thus, electrocatalytic nitrogen fixation and transformation is a promising solution to meet the ever-growing demand of ammonia, as well as to restore the global nitrogen balance. Implementing this technology will result in a breakthrough change towards a sustainable, low-carbon chemical production based on the use of renewable energy sources.

In order to develop a system able to convert efficiently nitrogen into ammonia, three aspects have been taken into account in this PhD work: i) the synthesis and advanced characterization of active electrocatalysts/electrodes, suitable to perform the reduction reactions, ii) the electrochemical characterization of these materials and their testing in NRR, iii) the engineering design of the cell and related electrodes, optimized to attain the maximum benefit and to minimize the resistances that lead to overpotentials.

Initially, Fe-MOF-based (Fe@Zn/SIM-1) electrodes were prepared and assembled to be tested in NRR by using an advanced engineered three-phase reactor, working in gas-phase. This electrochemical device was homemade and realized in a very compact configuration and without using liquid electrolyte in the cathode (electrolyte-less configuration). The tests were carried out adopting a rigid protocol to avoid false positive due to ammonia contaminations, on two catalyst forms (as MOFs and in the pyrolyzed form). A part of the work, in fact, was dedicated to the development of new experimental strategies for avoiding false positive in the detection of ammonia, which is one of the topics recently studied from scientists working in NRR. An easier methodology based on UV-visible spectrophotometric analysis (coupled with blank tests with inert gases) was successfully suggested, although more sophisticated analytical techniques may definitely confirm the real source of ammonia, (i.e., using ^{15}N labelled nitrogen) as recently indicated in literature.

Results showed some activity of these Fe@Zn/SIM-1 materials in NRR; however, the performances strongly decreased after pyrolysis of the electrocatalysts, and in general this class of MOFs were not much stable in the reaction environment. A possible explanation is that ammonia produced in these tests majorly came from the Fe@Zn/SIM-1 itself, which contained nitrogen atoms in the molecular structure. This hypothesis was also confirmed by check analysis with inert gas (He, or Ar), as required by the analytical protocol adopted. These results also confirmed that Fe@Zn/SIM-1 MOFs were nor stable in aqueous solution, permeated from the Nafion membrane directly assembled with the MOF-based electrode. Therefore, a different MOF electrocatalyst was needed, more stable and suitable to be used as efficient electrode for NRR, and thus not containing nitrogen atoms in its structure.

Thus, a series of improved Fe-based and Fe-alkali metal-based MOF UiO-66-$(COOH)_2$ were synthesized by cation exchange reaction technique for the preparation of more efficient and stable electrodes for NRR. Results evidenced that 80% cation exchange Fe@UiO-66-$(COOH)_2$ (with an actual Fe content of around 8 wt.%) was the best electrocatalyst among the tested Fe-based MOF catalysts. The performances in NRR highly depended on cell and electrode design. Specifically, an ammonia yield of 1.19 $\mu g\ h^{-1}\ mg_{cat}^{-2}$ was obtained with an assembling configuration of layers ordered as i) Nafion (the membrane), ii) Fe-based MOF (the electrocatalyst), iii) GDL (the carbon gas diffusion layer) and iv) a further layer of Fe-MOF. The effect of applied voltage was also studied, evidencing an optimal voltage of -0.5 V vs. RHE to maximize activity in NRR and limiting the side hydrogen evolution reaction. As currently used in the industrial catalysts for Haber-Bosh process, the introduction of potassium in the electrocatalysts was also explored, in order to facilitate charge transfer from K^- ions to the Fe-based catalyst surface, balancing the dissociative chemisorption between H_2 and N_2, and suppressing side reactions, thus improving both activity and stability. These results were very promising, although a further experimentation is needed to improve their performances in NRR, to overcome limitations related to MOF materials themselves, majorly due to their low conductivity and stability.

Finally, the fabrication of a novel 3D porous framework of alkalized Ti_3C_2 MXenes was performed to enhance definitely the performances in NRR. Particularly, it was demonstrated that the transformation from a 2D-(nanosheets) to a 3D-type nanostructure (nanoribbons) led to a significant enhancement of the N_2 fixation activity due to the formation of exposed Ti-OH sites. The results evidenced that a 2D (nanosheet) morphology was not necessary in MXene materials to provide activity in NRR, and a different morphology (nanoribbon), not having the same basal planes and type of edges, provided instead an about five-time higher catalytic activity. Characterization data have shown that in nanoribbon morphology, there was a preferential formation of exposed Ti-O sites, which various studies have indicated as responsible for improved electron transfer, adsorption, and activation of dinitrogen. A linear relationship was observed between ammonia formation rate and amount of oxygen on the surface of Ti_3C_2 MXene.